DEPARTMENT OF AEROSPACE ENGINEERING
COLLEGE OF ENGINEERING & TECHNOLOGY
OLD DOMINION UNIVERSITY
NORFOLK, VIRGINIA 23529

NAVIER-STOKES, DYNAMICS AND AEROELASTIC COMPUTATIONS FOR VORTICAL FLOWS, BUFFET AND FLUTTER APPLICATIONS

By

Osama A. Kandil, Principal Investigator

Progress Report
For the period October 1, 1992 to September 30, 1993

Prepared for
National Aeronautics and Space Administration
Langley Research Center
Hampton, VA 23681-0001

Under
Research Grant NAG-1-648
Dr. Samuel R. Bland, Technical Monitor
SDYD-Unsteady Aerodynamics Branch

Submitted by the
Old Dominion University Research Foundation
P.O. Box 6369
Norfolk, Virginia 23508-0369

September 1993

NAVIER-STOKES, DYNAMICS AND AEROELASTIC COMPUTATIONS FOR VORTICAL FLOWS, BUFFET AND FLUTTER APPLICATIONS

Osama A. Kandil*
Aerospace Engineering Department
Old Dominion University, Norfolk, VA 23529

ACCOMPLISHMENTS

In the period of October 1, 1992 to September 30, 1993, the Principal Investigator (PI) with the assistance of three graduate students have achieved the following accomplishments under Grant No. NAG-1-648. This grant is jointly supported by the NASA Langley Research Center, Aeroelastic Analysis and Optimization Branch (Monitors: Dr. Samuel R. Bland and Dr. Woodrow Whitlow, Jr.—Branch Head) and the Air Force Office of Scientific Research, Aeronautics Directorate — Unsteady Aerodynamics Program (Monitor: Major Daniel Fant.).

I. Publications:

I.1. Kandil, O. A. and Flanagan, M. W., "Vertical Tail Buffet in Vortex Breakdown Flows," Fifth International Symposium on Computational Fluid Dynamics Sendai, Japan, August 31–September 3, 1993, Vol. I, pp. 432–437, (a copy is enclosed).

I.2. Kandil, O. A., Kandil, H. A. and Massey, S. J., "Simulation of Tail Buffet Using Delta Wing-Vertical Tail Configuration," AIAA 93–3688–CP, AIAA Atmospheric Flight Mechanics Conference, Monterey, CA, August 9–11, 1993, pp. 566–577, (a copy is enclosed).

I.3. Kandil, O. A., Kandil, H. A. and Liu, C. H., "Shock-Vortex Interaction Over a 65–Degree Delta Wing in Transonic Flow," AIAA 93–2973, AIAA 24th Fluid Dynamics Conference, Orlando, FL, July 6–9, 1993 (a copy is enclosed).

---

* Professor, Eminent Scholar and Chairman of Aerospace Engineering Department.

I.4. Kandil, H. A., Kandil, O. A. and Liu, C. H., "Supersonic Vortex Breakdown Over a Delta Wing in Transonic Flow," AIAA 93–3472, CP, AIAA 11th Applied Aerodynamics Conference, Monterey, CA, August 11–13, 1993, Vol. I, pp. 582–596, (a copy is enclosed).

I.5. Kandil, O. A., "Simulation of Vertical Tail Buffet," NAS Technical Summaries Report, to be published in December 1993.

I.6. Kandil, O. A. and Salman, A. A., "Prediction and Control of Slender Wing Rock," ICAS Paper No. 92–4.7.2–CP, 18th ICAS Congress, Beijing, People's Republic of China, September 21–25, 1992, Vol. 2, pp. 1430–1441.

II. Abstracts Submitted to Technical Conferences:

II.1. Kandil, O. A. and Massey, S. J., "Computation of Vortex-Breakdown Induced Tail Buffet Undergoing Bending and Torsional Vibrations," Submitted to AIAA/ASME/ASCE 35th SDM Conference, Hilton Head, SC, April 18–21, 1994.

II.2. Kandil, O. A., Kandil, H. A. and Kalisch, M., "Pitching Oscillation of a 65–degree Delta Wing in Transonic Flow," Submitted to AIAA/ASME/ASCE 35th SDM Conference, Hilton Head, SC, April 18–21, 1994.

III. Conference Presentations and Activities:

III.1. "Simulation of Tail Buffet Using Delta Wing-Vertical Tail Configuration," AIAA Atmospheric Flight Mechanics Conference, Monterey, CA, August 9–11, 1993. Prof. O. A. Kandil gave the presentation.

III.2. "Vertical Tail Buffet in Vortex Breakdown Flows," Fifth International Symposium on Computational Fluid Dynamics, Sendai, Japan, August 31–September 3, 1993. Mr. Mark W. Flanagan gave the presentation.

III.3. "Shock-Vortex Interaction Over a 65–Degree Delta Wing in Transonic Flow," AIAA 24th Fluid Dynamics Conference, Orlando, FL, July 6–9, 1993. Prof. O. A. Kandil gave the presentation.

III.4. "Supersonic Vortex Breakdown Over a Delta Wing in Transonic Flow," AIAA 11th Applied Aerodynamics Conference, Monterey, CA, August 9–11, 1993. Prof. O. A. Kandil gave the presentation.

III.5. Chairing a session titled, "Vortex Dominated Flows I," AIAA 24th Fluid Dynamics Conference, Orlando, FL, July 6–9, 1993. Prof. O. A. Kandil chaired the session.

III.6. "Prediction and Control of Slender Wing Rock," 18th ICAS Congress, Beijing, People's Republic of China, September 21–25, 1992. Prof. O. A. Kandil gave the presentation.

III.7. "Simulation of Vertical Tail Buffet," Seminar Series, School of Mechanical and Aerospace Engineering, Old Dominion University, Norfolk, VA, September 24, 1993. Prof. O. A. Kandil gave the presentation.

III.8. Chairing a session titled, "Flow Control," IUTAM Symposium on Fluid Dynamics of High Angle of Attack, University of Tokyo, Japan, September 13–17, 1992. Prof. O. A. Kandil chaired the session.

III.9. Invited by the Japanese Institute of Space and Astronautical Sciences to give a seminar on "CFD/Dynamics/Control Interaction," Tokyo, Japan, September 18, 1992. Prof. O. A. Kandil gave a presentation.

IV. Interaction with Other Federal Agencies:

1. **AFOSR:** A report has been submitted to Major Daniel Fant, manager of the unsteady program at the AFOSR on September 7, 1993. The report summarizes the important research results in supersonic vortex breakdown on delta wings and vertical-tail buffet problem. It also covers the concepts and ideas that benefit air force applications. It covers the period of October 1–September 30, 1993. Major Fant is supporting part of the present work for the FY 1994 at $35 K.

2. **Numerical Aerodynamics Simulation:**

   A proposal for computing resources has been submitted to the NAS facilities at NASA Ames in November 1992. The proposal has been approved for 1,100 hrs of computational time. Additional 500 hrs have been added to our account in July 1993. A summary has been submitted in July 1993 for publication in the NAS Annual Summaries.

3. The Principal Investigator helped researchers at two branches at NASA Langley and a researcher at the Air Force Academy in Colorado to correct boundary conditions for unsteady flow calculation in the computer code "CFL3D".

V. Graduate Students:

The Principal Investigator has three graduate students who are working on their M.S. thesis and Ph.D. dissertation. They are supported under this grant with the funds from NASA Langley Research Center and AFOSR. These students are:

V.1. **Mr. Mark W. Flanagan (US Citizen):** He is supported under the present grant and a supplement from the Aerospace department. He is expected to defend his M.S. thesis in October 1993. He thesis is titled "Computational Simulation of Vertical Tail Buffet in a Configured Duct." He is staying for his Ph.D. degree in the Aerospace Engineering

Department. His Ph.D. dissertation will focus on simulation and optimization control of three-dimensional tail buffet phenomenon.

V.2. **Mr. Steven J. Massey (US Citizen):** He is supported under the present grant and a supplement from the Aerospace department. He is expected to defend his M.S. thesis in March, 1994. His thesis is titled "Computational Simulation of Tail Buffet Using a Delta Wing-Vertical Tail Configuration." He is staying for his Ph.D. dissertation which will focus on simulation and optimizational control of tail buffet for bending and torsional responses.

V.3. **Ms. Margaret Kalisch (US Citizen):** She joined our research group in May 1993. She has a M.S. degree from the Naval Postgraduate School in Monterey, CA. She is working on her Ph.D. degree in Aerospace Engineering. She is currently supported under the present grant. Her Ph.D. dissertation will focus on multi-mode coupling (roll/pitch and/or yaw) of a delta wing during vortex breakdown in transonic regime.

VERTICAL TAIL BUFFET IN VORTEX BREAKDOWN FLOWS

Osama A. Kandil and Mark W. Flanagan
Aerospace Engineering Department
Old Dominion University
Norfolk, Virginia 23529, USA

5th International Symposium on
Computational Fluid Dynamics
Sendai, Japan-August 31–September 3, 1993

VERTICAL TAIL BUFFET IN VORTEX BREAKDOWN FLOWS

Osama A. Kandil* and Mark W. Flanagan*

***Aerospace Engineering Department, Old Dominion University, Norfolk, Virginia 23529, USA**

Computational simulation of vertical tail buffet has been accomplished using a simple generic model. The model consists of a vortex-breakdown flow in a configured circular duct and a vertical flat plate which is placed as a cantilever downstream of the vortex-breakdown flow. Vortex-breakdown flow is generated through a shock wave at the duct inlet. The unsteady, compressible, full Navier-Stokes (NS) equations and the aeroelastic equation for bending vibrations are solved sequentially to obtain the unsteady vortex-breakdown loads on the plate and its aeroelastic deflections, respectively. The grid displacements are obtained using an interpolating equation.

1. INTRODUCTION

The ability of modern fighter aircraft to fly and maneuver at high angles of attack is of prime importance. This capability is achieved, for example in the F/A-18 Fighter, through the combination of the leading-edge extension (LEX) for a delta wing and the use of a single or twin vertical tail(s). However, at some flight conditions, the vortices emanating from the highly-swept LEX breakdown before reaching the vertical tails which get bathed in a wake of highly unsteady, turbulent swirling flow. The vortex-breakdown flow produces unsteady loads which in turn produce severe buffeting of the vertical tails and have led to their premature fatigue failure. Experimental research work has been conducted on different models of the F/A-18 to understand the flow physics, measure the tails' response [1–4] and alleviate the buffet phenomenon [5]. Cole, Moss and Doggett [6] have found that the buffet response of a 1/6 size model of the F-18 airplane occurs in the first bending mode.

The crucial point in predicting the buffet characteristics is the knowledge of the driving unsteady air loads associated with the vortex breakdown flow. Edwards [7] presented a good assessment of the computational cost of this problem for a full fighter aircraft. The principal author of this paper has proposed two simple models to simulate and study the vertical-tail buffet problem at a substantially reduced computational cost in comparison with the cost of solving for the flow around a full fighter aircraft. The basic concept behind these models is to be able to generate an unsteady, vortex-breakdown flow and to place a vertical tail, which is cantilevered, downstream of the vortex-breakdown flow. In this way, the buffet problem is isolated from the whole configuration and the computational resources are focused on a small region for high resolution. The first proposed model consists of a configured duct in which the inlet swirling flow is forced to breakdown either through a shock wave [8] (for transonic and supersonic inlet flows) or through a gradual adverse pressure gradient that is generated by the duct wall (for subsonic inlet swirling flows). Downstream of the breakdown flow, a vertical cantilevered tail is placed. In the second model, the configuration consists of a delta wing at a critical angle of attack which produces breakdown of the leading-edge vortex cores. Downstream of the breakdown flow, a vertical single or twin-tail configuration, which is fixed as a cantilever, is placed.

Computational simulation using the second model has been presented in Ref. [9] by Kandil, Kandil and Massey. In the present paper, the first model is used for the computational simulation of vertical tail buffet. The model consists of a configured circular duct with supersonic swirling flow which is forced to breakdown through a shock wave at the inlet. Downstream of the vortex-breakdown flow a plate is placed as a cantilever which is fixed at the duct wall. The initial flow conditions are obtained by solving the unsteady, compressible, full NS equations accurately in time while the plate is assumed to be rigid. Next, the NS equations are sequentially solved with the aeroelastic equation of bending vibrations for the plate deflection. The grid is displaced using an interpolation equation.

2. FORMULATION AND COMPUTATIONAL SCHEME

The present multidisciplinary problem is solved using three sets of equations which consist of the unsteady, compressible, full NS equations; the aeroelastic equation for bending vibrations of a cantilever beam, which approximates the plate bending vibrations, and an interpolation equation to move the grid due to the plate deflection. The NS equations are given in Ref. [9] and are solved using an implicit, upwind, flux-difference splitting (Roe scheme), finite-volume scheme. The aeroelastic equation for the bending vibrations is given by

$$EI\frac{\partial^4 w}{\partial r^4} + m\frac{\partial^2 w}{\partial t^2} = N(r,t) \tag{1}$$

where r is the radial distance from the fixed support along the beam length l_t, E the modulus of elasticity, I the area moment of inertia, m the mass per unit length and N is the net surface pressure force per unit length. The dimensionless form of w, r, E, I and m are given by

$$w = \frac{w^*}{r_d^*}, \quad r = \frac{r^*}{r_d^*}, \quad E = \frac{E^*}{\rho_\infty^* a_\infty^{*2}},$$
$$I = \frac{1}{12}\frac{d^{*3}b^*}{r_d^{*4}}, \quad m = \frac{m^*}{\rho_\infty^* r_d^{*2}} \tag{2}$$

where r_d^* is the duct inlet radius, ρ_∞^* the freestream air density, a_∞^* the freestream speed of sound, d^* the plate thickness, b^* the plate width and the "*" denotes dimensional quantities. The geometrical and natural boundary conditions are given by

$$w(0,t) = \frac{\partial w}{\partial r}(0,t) = \frac{\partial^2 w}{\partial r^2}(l_t,t) = \frac{\partial^3 w}{\partial r^3}(l_t,t) = 0 \tag{3}$$

The solution to Eq. (1) is given by

$$w(r,t) = \sum_{j=1}^{n} \phi_j(r) q_j(t) \tag{4}$$

substituting Eq. (4) into Eq. (1) and using the Galerkin method, the equation for the generalized coordinates, $q_j(t)$, is obtained. The solution for $q_j(t)$ is obtained either by using a convolution integral or by using a four-stage Runge-Kutta scheme. For the present problem, six natural modes of vibration, ϕ_j, are used. More details of the solution are given in Ref. [9].

For the grid displacements, the following interpolation equation is used for the x-coordinate which is measured from the plate surface

$$x_{i,j}^{n+1} = x_{i,j}^n + w_{i,j}^{n+1} \cos\left(\frac{x_{i,j}^n}{X_r \text{ or } l}\frac{\pi}{2}\right) \tag{5}$$

where X_r or l is the maximum x coordinate (measured from the plate surface) of a grid point at the right (r) or left (l) boundary of the computational domain. With Eq. (5), a point on the plate is displaced by the total plate deflection and a point at either boundary is not displaced.

3. COMPUTATIONAL RESULTS

A configured, circular duct which is similar to the one used by the senior author in Ref. [8] is employed for the present problem. The duct length here is 3.9 dimensionless units. It is configured such that a supersonic inlet flow produces a shock at the inlet section which is strong enough to break down the inlet swirling flow. A half of the duct axial plane is shown in Fig. 1. As a cantilevered plate at the duct wall of length $l_t = 0.4$ is placed at the axial station $x = 2.0$, multi-block grids are used. There are three blocks of grids; the first is to the left of the plate ($0 \le x \le 2.0$, $r \ge 0.6$) which consists of 182×48 grid points in the axial and radial directions, respectively; the second is to the right of the plate ($2.0 \le x \le 3.9$, $r \ge 0.6$) which consists of 120×48 grid points in the axial and radial directions, respectively; the third extends from the center line to the level of plate tip ($0 \le r \le 0.6$, $0 \le x \le 3.9$) which consists of 302×64 grid points in the axial and radial directions, respectively. The minimum radial grid size at the center line is $\Delta r_{\min} = 3.5 \times 10^{-3}$ and the minimum axial grid size at the plate surface is $\Delta x_{\min} = 3 \times 10^{-4}$. Figure 1 shows the grid used.

The problem is solved for a quasi-axisymmetric flow by forcing the components of the flowfield vector to be equal on two meridian planes in close proximity of each other. The inlet flow Mach number is 1.75 and the Reynolds number is 10^5 (based on the duct inlet radius). The inlet profile for the tangential velocity is given by

$$\frac{w}{U_\infty} = \frac{k_\epsilon}{r}\left[1 - \exp\left(-\frac{r^2}{r_m^2}\right)\right] \tag{6}$$

where $U_\infty = 1.74$, $r_m = 0.2$ and $k_\epsilon = 0.1$. The maximum $\frac{w}{U_\infty}$, swirling ratio β, is at $r = 0.224$ and its value is kept at 0.32. The radial velocity, v, at the inlet is set equal to zero and the radial momentum equation is integrated to obtain the inlet pressure profile. Finally, the density ρ is obtained from the definition of the speed of sound for the inlet flow. With this compatible set of profiles, the computations are carried out accurately in time with $\Delta t = 0.001$ and without inserting the plate until $t = 9$ dimensionless time units.

The boundary conditions for this step consists of the inflow Riemann-invariant conditions, solid boundary conditions at the duct wall, symmetry conditions at the centerline and extrapolating the flow variables at the duct exit boundary. Figure 2 shows two snapshots of the streamlines and Mach contours at $t = 3$ and $t = 8$. It is noticed that an oscillating shock developed at the duct inlet (see Mach contours) and the unsteady vortex-breakdown bubbles developed behind the shock. The present solution is the same as that obtained earlier with one block of grid.

3.1 Initial Conditions

For $t > 9$, a flat plate is impulsively inserted at $x = 2.0$ and is cantilevered at the duct wall. The computations are carried out accurately in time with $\Delta t = 0.001$ and with the plate being considered as a rigid boundary. Solid boundary conditions are enforced on the plate surfaces. Figure 3 shows snapshots of the streamlines and the Mach contours at $t = 10$, 11, 17, 23, 29 and 32. The streamlines show the continuous evolution, convection, merging and shedding of vortex-breakdown bubbles behind the oscillating inlet shock. They also show an unsteady, separated vortical region behind the plate. The Mach-contours figures show the oscillating shock at the inlet and unsteady shocks between the plate tip and the duct wall. Having produced a strong vortex-breakdown flow ahead and behind the plate, this solution serves as initial conditions for the next step. The next step is to couple the computational fluid dynamics with the aeroelastic equation for bending vibrations of the plate along with Eq. (5) for the grid displacements.

3.2 Vortex-Breakdown Flow and Plate Deflection

For $t > 34$, the plate is allowed to deflect in bending by solving Eq. (1) with the force per unit length, $N(r,t)$, obtained from the net surface pressure on the plate. Since the plate is oscillating, the kinematical boundary conditions are based on the relative velocity of the fluid with respect to the plate. The dynamical boundary condition $\frac{\partial p}{\partial n}$ on the plate is no longer equal to zero. The pressure gradient is modified to $\frac{\partial p}{\partial n} = -\rho \bar{a}_p \cdot \hat{n}$, where $\bar{a}_p$ is the plate acceleration which is equal to $\frac{\partial^2 w}{\partial t^2}\Big|_{plate}$ and $\hat{n}$ is the unit normal to the plate. The computations are carried out accurately in time with $\Delta t = 0.0001$. The plate dimensions are $l_t = 0.4$, $d = 0.02$ and $b = 0.157$. Its modulus of elasticity and its mass per unit length are $E = 0.499 \times 10^3$ and $m = 7.177$, respectively. Figure 4 shows snapshots of the streamlines and Mach contours during one cycle of periodic response of the plate. The snapshots are marked by the numbers 1, 2, 3 and 4 which correspond to the instants 1, 2, 3 and 4 shown on Fig. 5. Figure 5 shows the force distribution on the plate, N, at different time levels (from $t = 35$ to $t = 35.5$). It also shows the plate deflections at its midpoint and its tip. It is noticed that the period of oscillation is 0.3 time units which corresponds to a frequency of 20.94. The maximum tip deflection of the plate is 2.5×10^{-4}, which is of the same order as that of the axial minimum spacing of the grid at the plate surface.

4. CONCLUDING REMARKS

A simple generic model is introduced to simulate the vertical tail buffet problem due to vortex-breakdown flows. The model consists of a configured circular duct which produces unsteady vortex-breakdown flow for the inlet supersonic swirling flow due to an oscillating shock. Downstream of the vortex-breakdown flow, a plate is placed as a cantilever at the duct wall. The problem is solved using three sets of equations which include the NS equations, the aeroelastic equation for bending vibrations and an equation for the grid displacements. The equations are solved sequentially using time accurate stepping to obtain the force distribution on the plate, the plate deflections and the grid displacements, respectively. It has been shown that the plate reaches periodic response in bending in a short time. The present work represents a proof of concept for a generic model to simulate vertical tail buffet. The next step is to consider the three-dimensional flow

problem with the plate surface placed along the axial flow direction where both bending and torsional modes can be considered.

5. ACKNOWLEDGEMENT

This research work has been supported by the NASA Langley Research Center and the Air Force Office for Scientific Research under Grant No. NAG-1-648. The authors acknowledge and appreciate the computational resources provided by the NASA Langley Research Center and the NAS computational facilities at NASA Ames Research Center.

REFERENCES

1. Sellers, W. L. III, Meyers, J. F. and Hepner, T. E., SAE Paper 88–1448, 1988.
2. Erickson, G. E., Hall, R. M., Banks, D. W., Del Frate, J. H., Shreiner, J. A., Hanley, R. J., and Pulley, C. T., AIAA Paper 89–2222, 1989.
3. Wentz, W. H., AIAA Paper 87–2474, 1987.
4. Lee, B. and Brown, D., AIAA Paper 90–1432, 1990.
5. Rao, D. M., Puram, C. K. and Shah, G. H., SAE Paper 89–2221, 1989.
6. Cole, S. R., Moss, S. W. and Doggett, R. V., Jr., NASA TM-102749, October 1990.
7. Edwards, J. W., NASA TM 101613, January 1990.
8. Kandil, O. A., Kandil, H. A. and Liu, C. H., AIAA Paper 93–0526, January 1993.
9. Kandil, O. A., Kandil, H. A. and Massey, S. J., AIAA Paper 93–3688–CP, August 1993.

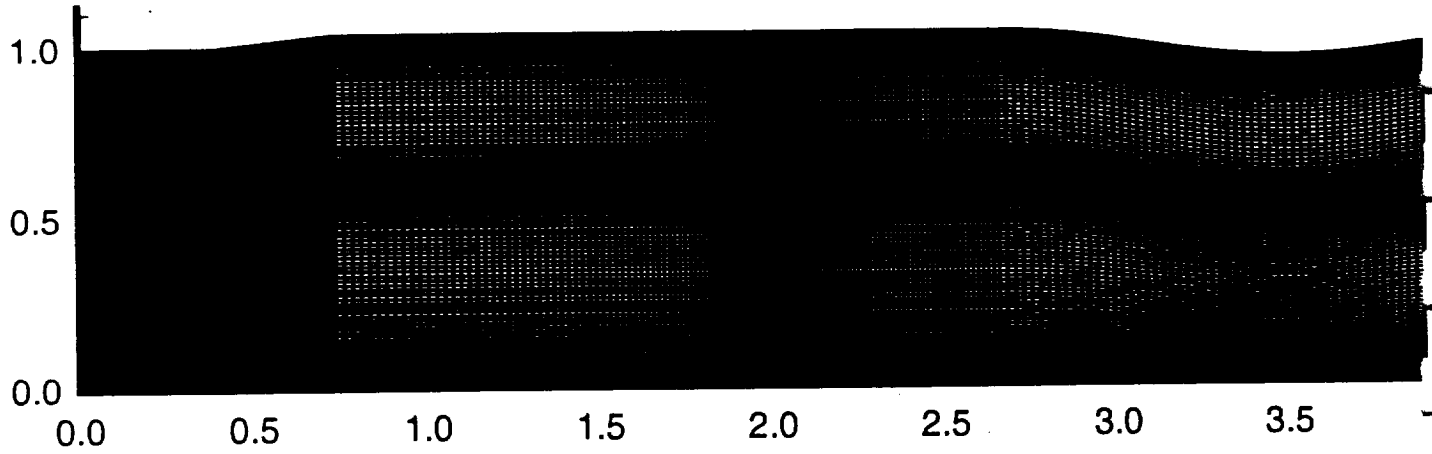

Fig. 1 Geometry and grid of the duct and plate.

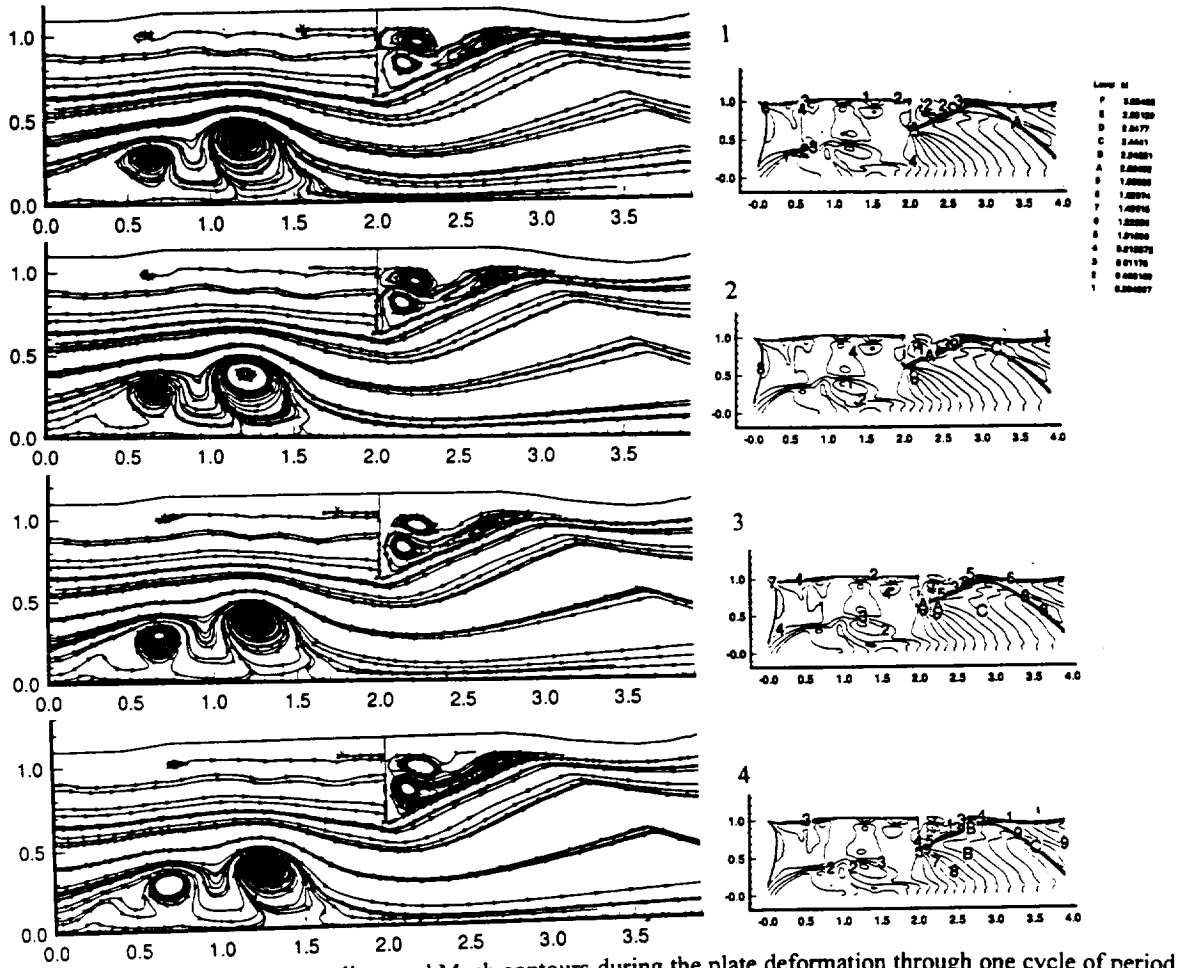

Fig. 4 Snapshots of streamlines and Mach contours during the plate deformation through one cycle of periodic response, $R_e = 10^5$, $M_\infty = 1.75$, $\beta = 0.32$, $l_t = 0.4$, $E = 0.499 \times 10^3$, $d = 0.02$, $b = 0.157$, $m = 7.177$, $\Delta t = 0.0001$

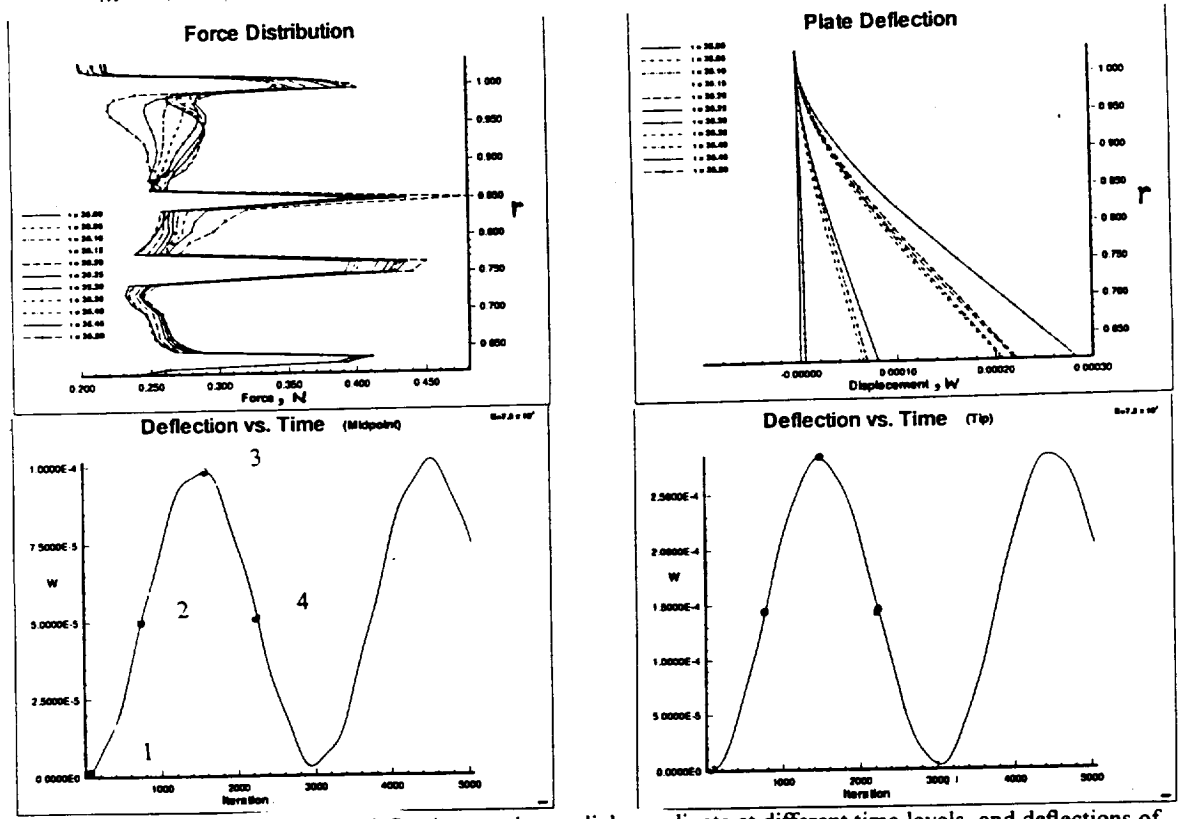

Fig. 5 Force per unit length and deflection vz plate radial coordinate at different time levels, and deflections of the midpoint and tip of plate vz time, $R_e = 10^5$, $M_\infty = 1.75$, $\beta = 0.32$, $l_t = 0.4$, $E = 0.499 \times 10^3$, $d = 0.02$, $b = 0.157$, $m = 7.177$, $\Delta t = 0.0001$

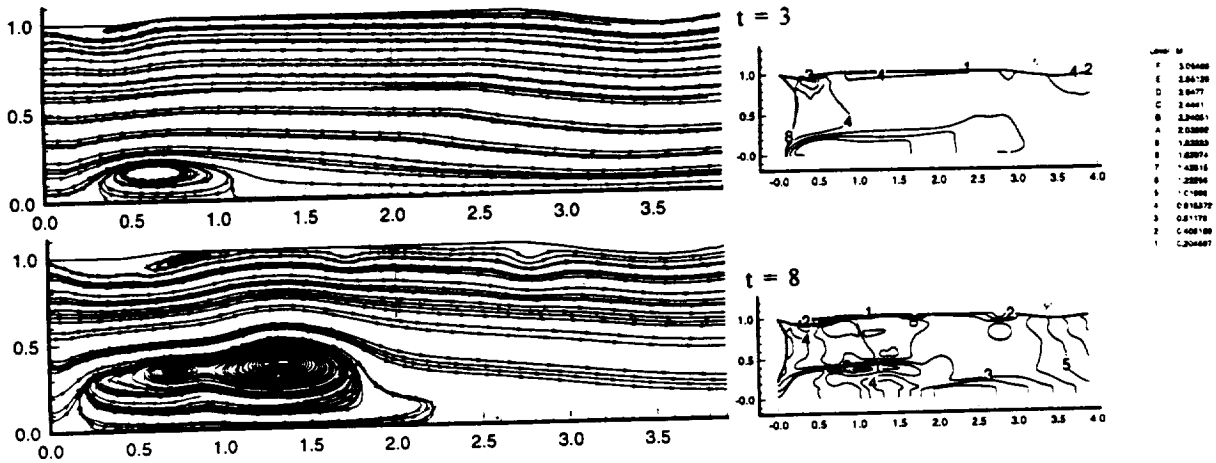

Fig. 2 Snapshots of streamlines and Mach contours before the plate is placed, $R_e = 10^5$, $M_\infty = 1.75$, $\beta = 0.32$, $\Delta t = 0.001$

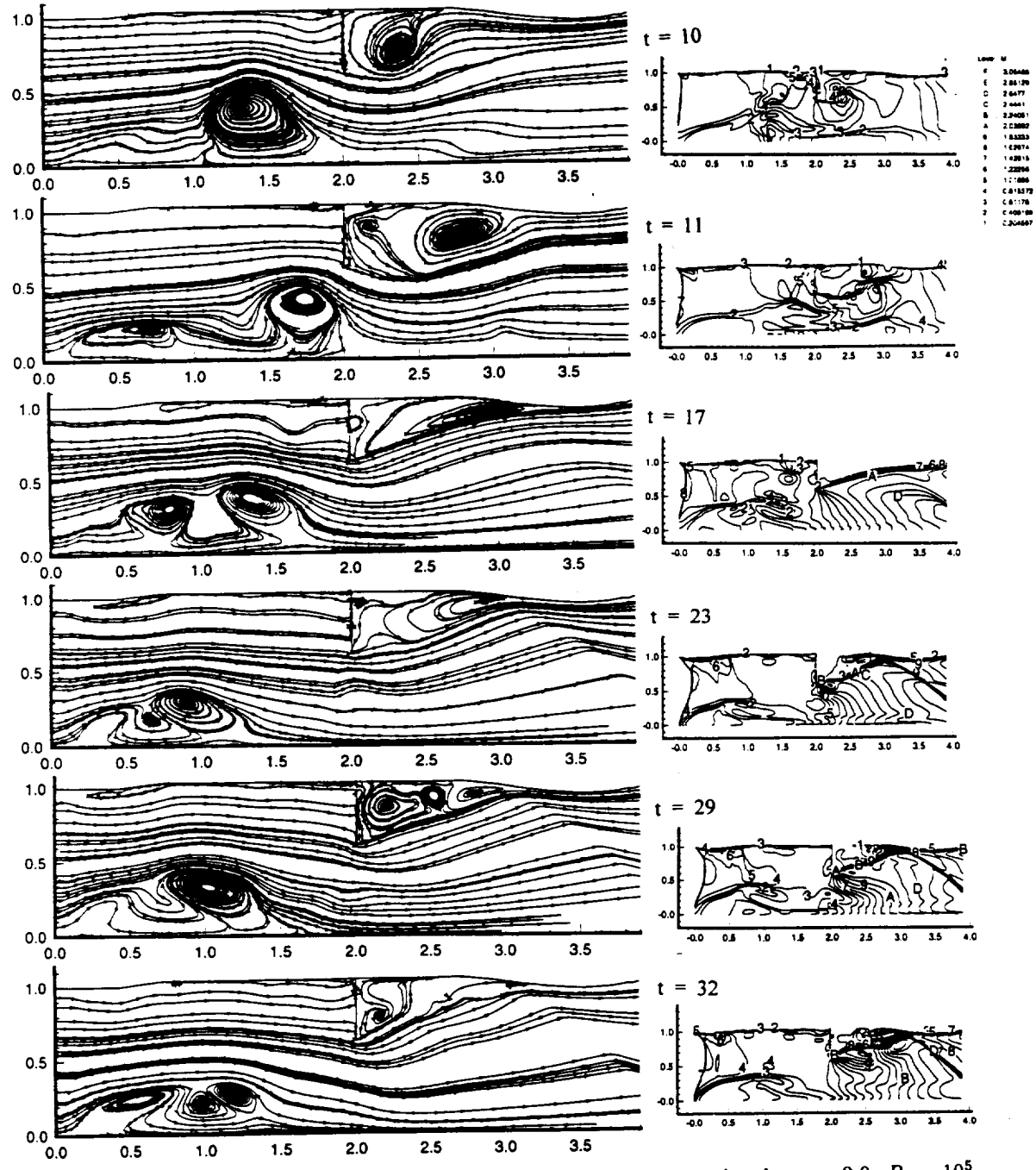

Fig. 3 Snapshots of streamlines and Mach contours with the rigid plate placed at $x = 2.0$, $R_e = 10^5$, $M_\infty = 1.75$, $\beta = 0.32$, $l_t = 0.4$, $\Delta t = 0.001$

AIAA-93-3688-CP

SIMULATION OF TAIL BUFFET USING DELTA WING-VERTICAL TAIL CONFIGURATION

Osama A. Kandil, Hamdy A. Kandil and Steven J. Massey
Old Dominion University, Norfolk, VA 23529

AIAA Atmospheric Flight Mechanics Conference
August 9–11, 1993/Monterey, CA

SIMULATION OF TAIL BUFFET USING DELTA WING-VERTICAL TAIL CONFIGURATION

Osama A. Kandil*, Hamdy A. Kandil, and Steven J. Massey*****
Old Dominion University, Norfolk, VA 23529

ABSTRACT

Computational simulation of the vertical tail buffet problem is accomplished using a delta wing-vertical tail configuration. Flow conditions are selected such that the wing primary-vortex cores experience vortex breakdown and the resulting flow interacts with the vertical tail. This multidisciplinary problem is solved successively using three sets of equations for the fluid flow, aeroelastic deflections and grid displacements. For the fluid dynamics part, the unsteady, compressible, full Navier-Stokes equations are solved accurately in time using an implicit, upwind, flux-difference splitting, finite-volume scheme. For the aeroelastic part, the aeroelastic equation for bending vibrations is solved accurately in time using the Galerkin method and a convolution integral solution. The grid for the fluid dynamics computations is updated every few time steps using an interpolation equation. The computational applications include a delta wing of aspect ratio 1 and two cases for the vertical tail. The first case is for a tail of aspect ratio of 2 located 0.5 chord length from the wing trailing edge. The second case is for a tail of aspect ratio of 1 located at the wing trailing edge.

INTRODUCTION

Recently, the design of modern fighter aircraft has been focused on high angle of attack maneuverability at high loading conditions, renewing the interest in the tail buffet problem. For these fighters, the ability to fly and maneuver at high angles of attack is of prime importance. This capability is achieved, for example in the F/A-18 fighter, through the combination of a leading-edge extension (LEX) and a delta wing and the use of vertical tails. The LEX maintains lift at high angles of attack by generating a pair of vortices that trail aft over the top of the aircraft. The vortex entrains air over the vertical tails to maintain stability of the aircraft. This combination of LEX and vertical tails leads to the aircraft excellent high angle of attack performance. However, at some flight conditions, the vortices emananting from the highly-swept LEX of the delta wing breakdown before reaching the vertical tails which get bathed in a wake of highly-turbulent, swirling flow. The vortex-breakdown flow produces severe buffet on the vertical tails and has led to their premature fatigue failure. Buffeting of the vertical tails of the F/A-18 fits into this category. During flight operations of this airplane large vibrations of the vertical tails have been observed.

Sellers et al.[1] conducted some three-component velocity surveys for a YF-17 model (a configuration similar to the F-18) at low speeds. Their results clearly show that at 25° angle of attack the vortex produced by the LEX experiences breakdown and that there are large fluctuations in the velocity in the vicinity of the vertical tails. They measured rms fluctuations as high as 40% of the freestream stream velocity. Erickson, et al.[2] presented a wind tunnel investigation of the F/A-18 aircraft. The investigation focused mainly on the measurements of steady forces and pressures on the LEX and laser light sheet measurements of the vortex structure. Some water tunnel studies conducted by Wentz[3] using an F-18 model also showed that the vortex produced by the LEX of the wing breaks down ahead of the vertical tails at angles of attack of 25° and higher. If these flows contain substantial energy at frequencies corresponding to the lower modes of vibration of the tail structure, significant structural response can result.

Another wind tunnel investigation of buffeting is published by Lee and Brown[4]. The buffeting of the vertical fin of a rigid 6% model of the F/A-18 has been investigated. Unsteady pressure measurements on the vertical fin were conducted and the vortex flow structure behind the fin was studied. The study was carried out with LEX fences on and off to conclude that the LEX fence has a small influence on the steady balance measurements such as lift and pitching moment.

---

* Professor, Eminent Scholar and Chairman of Aerospace Engineering Dept., Associate Fellow AIAA.
** Research Associate, Aerospace Engineering Dept., Member AIAA
*** Graduate Research Assistant, Aerospace Engineering Dept., Member AIAA.

Rao, Puram and Shah[5] proposed two aerodynamic concepts for alleviating high-alpha tail buffet characteristics of LEX vortex dominated twin tail fighter configurations. These concepts were explored in low speed tunnel tests on generic models via flow visualizations, 6–component balance measurements and monitoring of tail dynamics. Passive dorsal-fin extensions of the vertical tails, and an active LEX arrangement with up-deflected edge sections were evaluated as independent means of re-structuring the adverse vortical flow environment in the tail region. Each of these techniques successfully reduced the buffet. Used in combination, the two concepts indicated significant tail buffet relief with relatively minor impact on the high α configuration aerodynamics.

Cole, Moss and Doggett[6] tested a rigid, 1/6 size, full-span model of an F-18 airplane that was fitted with flexible vertical tails of two different stiffness. Vertical-tail buffet response results were obtained over the range of angles of attack from $-10°$ to $+40°$, and over the range of Mach numbers from 0.3 to 0.95. Their results indicated that the buffet response occurs in the first bending mode, increases with increasing dynamic pressure and is larger at M = 0.3 than that at a higher Mach number.

So far, there are no available theoretical or computational methods to predict and control the aeroelastic buffet characteristics of vertical tails. The crucial point in predicting the buffet characteristics is the knowledge of the driving unsteady airloads associated with flow separations and vortex breakdown. Edwards[7] presented a good assessment of the computational cost of this problem for a full fighter aircraft. The principal author of this paper has proposed two simple models to simulate and study the vertical-tail buffet problem at a substantially reduced computational cost in comparison with the cost of solving for the flow around a full fighter aircraft. The basic concept behind these models is to be able to generate an unsteady, vortex-breakdown flow and to place a cantilevered vertical tail, downstream of the vortex-breakdown flow. In this way, the buffet problem is isolated from the whole configuration and the computational resources are focused on a small region for high resolution. The first proposed model consists of a configured duct in which the inlet swirling flow is forced to breakdown either through a shock wave[8] (for transonic and supersonic inlet flows) or through a gradual adverse pressure gradient that is generated by the duct wall (for subsonic inlet swirling flows). Downstream of the breakdown flow, a vertical cantilevered tail is placed. In the second model, the configuration consists of a delta wing at a critical angle of attack which produces breakdown of the leading-edge vortex cores[9]. Downstream of the breakdown flow, a vertical single or twin-tail configuration which is fixed as a cantilever is placed.

In the present paper, the second model is considered for the computational simulation. The model consists of a delta wing of aspect ratio 1 and two cases of a single vertical tail. In the first case, the tail is of aspect ratio 2 and is placed at 0.5 root-chord length from the wing trailing edge. In the second case, the tail is of aspect ratio 1 and is placed at the wing trailing edge. The tail is cantilevered at the lower side and the configuration is pitched at a 35° angle of attack. The flow Mach number and Reynolds number are 0.4 and 10,000, respectively. The problem is solved sequentially using the time-accurate integration of the laminar, unsteady, compressible Navier-Stokes equations, the aeroelastic equation for a beam in a bending mode and an equation to update the locations of grid points.

FORMULATION

The formulation of the problem consists of three sets of governing equations along with certain initial and boundary conditions. The first set is the laminar, unsteady, compressible, full Navier-Stokes equations. The second set consists of the aeroelastic equations for the vibration modes which could be coupled bending and torsion modes. In the present paper, only the bending vibration is considered without structural damping or nonlinearities, which could be added in the future without any difficulty. The third set consists of an equation for calculating the grid displacements due to the tail deflections. The literature shows various methods for computing the grid displacements. The simplest methods use simple interpolation functions such that the grid points adjacent to the aeroelastic surface move with the surface while the grid points at the computational-region boundary do not move[10,11]. In the more advanced methods for moving the grid, the grid is simulated as a static[12–14] or dynamic truss. The unsteady, linearized, Navier-displacement equations have also been used successfully by Kandil et al. to move the grid dynamically[15,16]. In the present paper, we use simple grid interpolation to move the grid. Next, the governing equations for each set are given:

Fluid Flow:

The conservative form of the dimensionless, unsteady, compressible, full NS equations in terms of time-dependent, body-conformed coordinates ξ^1, ξ^2 and ξ^3 is given by

$$\frac{\partial \bar{Q}}{\partial t} + \frac{\partial \bar{E}_m}{\partial \xi^m} - \frac{\partial (\bar{E}_v)_s}{\partial \xi^s} = 0; m = 1-3, s = 1-3 \quad (1)$$

where

$$\xi^m = \xi^m(x_1, x_2, x_3, t) \quad (2)$$

$$\bar{Q} = \frac{\hat{q}}{J} = \frac{1}{J}[\rho, \rho u_1, \rho u_2, \rho u_3, \rho e]^t \quad (3)$$

$$\begin{aligned} \bar{E}_m &\equiv inviscid\ flux \\ &= \frac{1}{J}\left[\partial_k \xi^m \hat{E}_k + \frac{\partial \xi^m}{\partial t}\hat{q}\right]^t \\ &= \frac{1}{J}[\rho U_m, \rho u_1 U_m + \partial_1 \xi^m p, \rho u_2 U_m \\ &+ \partial_2 \xi^m p, \rho u_3 U_m + \partial_3 \xi^m p, (\rho e + p) U_m \\ &- \frac{\partial \xi^m}{\partial t} p]^t \end{aligned} \quad (4)$$

$$\begin{aligned} (\bar{E}_v)_s &\equiv viscous\ and\ heat\text{–}conduction\ flux\ in\ \xi^s \\ &\quad direction \\ &= \frac{1}{J}[0, \partial_k \xi^s \tau_{k1}, \partial_k \xi^s \tau_{k2}, \partial_k \xi^s \tau_{k3}, \\ &\partial_k \xi^s (u_n \tau_{kn} - q_k)]^t; \quad k = 1-3,\ n = 1-3 \end{aligned} \quad (5)$$

$$U_m = \partial_k \xi^m u_k + \frac{\partial \xi^m}{\partial t} \quad (6)$$

The first element of the three momentum elements of Eq. (5) is given by

$$\partial_k \xi^s \tau_{k1} \equiv \frac{M_\infty \mu}{Re}\left[\left(\partial_k \xi^s \partial_1 \xi^n - \frac{2}{3}\partial_1 \xi^s \partial_k \xi^n\right)\frac{\partial u_k}{\partial \xi^n} + \partial_k \xi^s \partial_k \xi^n \frac{\partial u_1}{\partial \xi^s}\right] \quad (7)$$

The second and third elements of the momentum elements are obtained by replacing the subscript 1, everywhere in Eq. (7), with 2 and 3, respectively. The last element of Eq. (5) is given by

$$\begin{aligned} \partial_k \xi^s (u_p \tau_{kp} - q_k) &\equiv \frac{M_\infty \mu}{Re}\left[\left(\partial_k \xi^s \partial_p \xi^n\right.\right. \\ &- \left.\frac{2}{3}\partial_p \xi^s \partial_k \xi^n\right) u_p \frac{\partial u_k}{\partial \xi^n} \\ &+ \partial_k \xi^s \partial_k \xi^n u_p \frac{\partial u_p}{\partial \xi^n} \\ &+ \left.\frac{1}{(\gamma - 1)Pr}\partial_k \xi^s \frac{\partial (a^2)}{\partial \xi^n}\right]; p = 1-3 \end{aligned} \quad (8)$$

The reference parameters for the dimensionless form of the equations are c^*, a_∞, c^*/a_∞, ρ_∞ and μ_∞ for the length, velocity, time, density and molecular viscosity, respectively. The Reynolds number is defined as $Re = \rho_\infty V_\infty c^*/\mu_\infty$, where c^* is root-chord length of the wing. The pressure, p, is related to the total energy per unit mass and density by the gas equation

$$p = (\gamma - 1)\rho\left[e - \frac{1}{2}\left(u_1^2 + u_2^2 + u_3^2\right)\right] \quad (9)$$

The viscosity is calculated from the Sutherland law

$$\mu = T^{3/2}\left(\frac{1 + C}{T + C}\right), C = 0.4317 \quad (10)$$

and the Prandtl number $P_r = 0.72$. In Eqs. (1)-(8), the indicial notation is used for convenience.

Aeroelastic Deflections:

In the present paper, the vertical rectangular tail is treated as a homogeneous, uniform, cantilevered beam with rectangular section. For bending vibration, the dimensionless equation for the deflection $w(z,t)$ is given by

$$EI\frac{\partial^4 w}{\partial z^4} + m\frac{\partial^2 w}{\partial t^2} = N(z,t) \quad (11)$$

where z is the vertical distance from the fixed support along the beam length, l_t, E the modulus of elasticity, I the area moment of inertia, m the mass per unit length and N is the net surface pressure force per unit length. The dimensionless form of w, z, E, I, m and N are given by

$$\begin{aligned} w = \frac{w^*}{c^*}, z = \frac{z^*}{c^*}, E = \frac{E^*}{\rho_\infty^* a_\infty^{*2}}, \\ I = \frac{1}{12}\frac{d^{*3} b^*}{c^{*4}}, m = \frac{m^*}{\rho_\infty^* c^{*2}}, N = \frac{N^*}{\rho_\infty^* a_\infty^{*2} c^*} \end{aligned} \quad (12)$$

where c^* is the wing root-chord length, ρ_∞^* the freestream air density, a_∞^* the freestream speed of sound, d^* the tail thickness, b^* the tail chord length, N^* the net surface pressure force per unit length and the "*" denotes dimensional quantities. The geometrical and natural boundary conditions are given by

$$w(o,t) = \frac{\partial w}{\partial z}(o,t) = \frac{\partial^2 w}{\partial z^2}(l_t,t) = \frac{\partial^3 w}{\partial z^3}(l_t,t) = 0 \quad (13)$$

The solution to Eq. (11) is given by

$$w(z,t) = \sum_{j=1}^{n} \phi_j(z) q_j(t) \quad (14)$$

where $\phi_j(z)$ are comparison functions which satisfy the boundary conditions, and they are given by the natural modes of vibration

$$\phi_j(z) = \frac{\sin\beta_j z - \sinh\beta_r z}{\sin\beta_j l_t + \sinh\beta_r l_t} + \frac{\cosh\beta_j z - \cos\beta_j z}{\cosh\beta_j l_t + \cos\beta_j l_t} \tag{15}$$

and β_j are the eigenvalues obtained from the solution of $\cos\beta l_t \cosh\beta l_t = -1$. Substituting Eq. (14) into Eq. (11) and using the Galerkin method, the following equation is obtained for the generalized coordinates $q_j(t)$:

$$\sum_{j=1}^{n} m_{rj}\ddot{q}_j + \sum_{j=1}^{n} k_{rj}q_j = \hat{N}_r(t) \quad ;r = 1,2,\ldots,n \tag{16}$$

where

$$m_{rj} \equiv elements\ of\ mass\ matrix = m\int_o^{l_t} \phi_r\phi_j dz \tag{17.a}$$

$$k_{rj} \equiv elements\ of\ stiffness\ matrix = EI\int_o^{l_t} \frac{d^2\phi_r}{dz^2}\frac{d^2\phi_j}{dz^2}dz \tag{17.b}$$

$$\hat{N}_r \equiv generalized\ force = \int_o^{l_t} N\phi_r dz \tag{17.c}$$

Since m, I and E are constants and ϕ_r are orthogonal, the mass and stiffness matrices are diagonal and the set given by Eq. (16) is decoupled. Hence, the solution to the present simple case reduces to the solution of a decoupled set of second-order, ordinary-differential equations, where each equation corresponds to one of the natural modes. The solution is obtained either by using a closed-form convolution integral or by using a four-stage Runge-Kutta scheme. For the jth mode shape, Eq. (16) becomes

$$\ddot{q}_j + \frac{k_{rr}}{m_{rr}}q_j = \frac{\hat{N}_r(t)}{m_{rr}} \quad (no\ summation\ over\ r) \tag{17}$$

The convolution integral solution for this equation is given by

$$q_j(t) = \frac{1}{\omega_r m_{rr}}\int_o^t \hat{N}_r(\zeta)\sin\omega_r(t-\zeta)d\zeta + q_j(0)\cos\omega_r t + \frac{\dot{q}_j(0)}{\omega_r}\sin\omega_r t \tag{18}$$

where $\omega_r^2 = \frac{k_{rr}}{m_{rr}} = \frac{EI\beta_r^4}{m}$, $q_j(0)$ is the initial displacement and $\dot{q}_j(0)$ is the initial velocity.

If m, I and E are functions of z, then Eq. (16) will be a coupled set and one needs to use a normal-mode shape transformation from $q(t)$ to $\eta(t)$ to decouple the resulting set. For a coupled bending and torsion vibration, the present procedure can be generalized to obtain the solution. For the aeroelastic equations in the latter case, the solution is obtained using the four-stage Runge-Kutta scheme.

Grid Displacements:

In the present paper, we use simple interpolation functions to displace the grid due to the tail deflection. For bending vibrations, the tail deflection at any point on its surface, $w_{i,j,k}$, is in the spanwise direction (y coordinate). The spanwise coordinate of a grid point $y_{i,j,k}^{n+1}$ at the time level $n+1$ is computed from the equation

$$y_{i,j,k}^{n+1} = y_{i,j,k}^{n} + w_{i,j,k}^{n+1}\cos\left(\frac{y_{i,j,k}^{n}}{Y_{i,Jdim/4,k}}\frac{\pi}{2}\right) \tag{19}$$

where $Y_{i,Jdim/4,k}$ is the maximum y coordinate of a grid point at the boundary of the computational domain with an index of $Jdim/4$. Thus, the tail displacement $w_{i,j,k}^{n+1}$ is distributed through a cosine function among the y coordinates of the grid. Thus, a point on the tail is displaced by the total deflection and a point at the boundary is not displaced.

Boundary and Initial Conditions:

Boundary conditions consist of conditions for the fluid flow and conditions for the aeroelastic deflection of the tail. For the fluid flow, the Riemann-invariant boundary conditions are enforced at the inflow and outflow boundaries of the computational domain. At the plane of geometric symmetry, a periodic boundary condition is specified with the exception of grid points on the tail. On the wing surfaces, the no-slip and no-penetration conditions are enforced and $\frac{\partial p}{\partial n} = 0$. On the tail surfaces, the no-slip and no-penetration conditions for the relative velocity components are enforced (points on the tail surface are moving). The normal pressure gradient is no longer equal to zero since points on the tail surface are accelerating. This condition becomes $\frac{\partial p}{\partial n} = -\rho_\infty \bar{a}_t \cdot \hat{n}$, where $\bar{a}_t$ is the acceleration of a point on the tail, which is equal to $\frac{\partial^2 w}{\partial t^2}(z,t)$. For the boundary conditions of the aeroelastic deflection of the tail, they are given by Eq. (13).

Initial conditions consist of conditions for the fluid flow and conditions for the aeroelastic deflection of

the tail. For the fluid flow, the initial conditions correspond to the freestream conditions with $u_1 = u_2 = u_3 = 0$ on the wing and tail. For the aeroelastic deflection of the tail, the initial conditions for any point on the tail is that the displacement and velocity are zeros, $w(z,o) = \frac{\partial w}{\partial t}(z,o) = 0$

METHOD OF SOLUTION

The first step is to solve for the fluid-flow problem using the vortex-breakdown conditions and keeping the tail as a rigid beam. Equations (1)-(10) are solved time-accurately using the implicit, upwind, flux-difference splitting finite-volume scheme. The grid speed $\frac{\partial \xi^m}{\partial t}$ is set equal to zero in this step. This step provides the flow field solution along with the pressure difference across the tail. The pressure difference is used to generate the force per unit length of the tail, N. Next, Eqs. (14) and (18) are used to obtain the tail deflections, $w_{i,j,k}$. Equation (19) is used to compute the grid coordinates. The metric coefficients of the coordinate Jacobian matrix are updated as well as the grid speed, $\frac{\partial \xi^m}{\partial t}$. Next, the computational cycle is repeated using Eqs. (1)-(10) for the pressure difference across the tail, Eqs. (14) and (18) for the tail deflections and Eq. (19) for the grid coordinates. It should be noted that the time step for the fluid-flow problem, Δt_f, is an order of magnitude less than the time step for the aeroelastic deflection, Δt_d. Moreover, the maximum tail deflection w for each Δt_d is very small. Hence, one does not need to compute w for each time step, Δt_f. For example, if $\Delta t_d = 10\ \Delta t_f$, the computation of the aeroelastic deflections and grid coordinates can be performed every $10\ \Delta t_f$.

COMPUTATIONAL APPLICATIONS

CASE 1:

The delta wing-vertical tail configuration consists of a sharp-edged, delta wing of aspect ratio 1 and a rectangular, vertical tail of aspect ratio 2, which is placed in the plane of geometric symmetry. The vertical-tail leading edge is located at 0.5 root-chord length from the wing trailing edge. The lower edge of the tail is along the wing axis and the tail is clamped at that edge. The wing angle of attack is 35° and the freestream Mach number and Reynolds number are 0.4 and 10,000, respectively. An O-H grid of 125×85×84 grid points in the wrap-around, normal and axial directions, respectively, is used for the solution of the fluid-flow part of the problem.

The solution and analysis of this problem have progressed through rigorous steps in order to prove the capability of the present model for simulating the present multidisciplinary problem:

Step 1. Fluid Flow Around the Configuration (Initial Conditions):

The laminar, unsteady, compressible, full Navier-Stokes equations have been integrated time accurately using the implicit, upwind, flux-difference splitting, finite-volume scheme with $\Delta t = 0.003$. During this step, the tail is kept rigid. The results of this step are used as initial conditions for the second step. Figure 1 shows the spanwise, surface-pressure coefficient (C_p) on the wing at different chord stations at it = 12,400 (37.2 dimensionless time). At $x = 0.421$, the C_p-curve shows asymmetry with the pressure on the left side having less suction than the pressure on the right side (looking in the upstream direction). This indicates that the left-vortex-core size is enlarging. In Fig. 4, it is noticed that at this location a spiral saddle point is formed and a spiral vortex-breakdown mode is developing downstream of that point. Returning back to Fig. 1, it is noticed that the asymmetry exists in all the cross-flow planes downstream of x = 0.421. At $x = 0.814$, a rapid decrease in the suction pressure on the left side is observed and Fig. 4 shows several spiral saddle points at that location. At x = 0.944, a rapid decrease in the suction pressure on the right side is observed and spiral vortex breakdown develops in the right vortex core (see Fig. 4). Figure 2 shows the total-pressure-loss contours and instantaneous streamlines for the left and right sides at different chord stations. The asymmetry is very clear at $x = 0.65$ and 1.0. At $x = 1.0$ and on the right side, it is noticed that a repelling spiral saddle point exists, which indicates the existence of vortex breakdown.

Figure 3 shows the instantaneous streamlines in cross-flow planes at two chord stations $x = 1.375$ and $x = 2.019$. The vertical-tail leading edge is located at $x = 1.5$ and its trailing edge is at $x = 2.0$. It is clear that the vertical tail is subjected to asymmetric, unsteady, surface-pressure loads due to the vortex-breakdown flow. Figures 4 and 5 show a plan view of the wing and a three-dimensional view of the wing-tail configuration, respectively, along with the spiral saddle points and the asymmetric spiral vortex-breakdown modes of the leading-edge vortex cores.

Figure 6 shows snapshots of the pressure contours on the right (J = 1) and left (J = $Jdim$) surfaces of the vertical tail and the pressure-difference on it at two time levels; it = 12,400 and it = 12,600. A close inspection of these loads reveals that the tail is subjected to both bending and torsional loads. In the present paper, only the bending vibration is taken into consideration (torsional vibrations are also under consideration). Figure 7 shows the corresponding lumped, aerodynamic force per unit length of the tail, $N(z)$, at two time levels, t = 37.2 and t = 37.8. It is noticed that within this short time of change, $N(z)$ changes rapidly in magnitude and direction. The results at it = 12,600 are used for the initial conditions of the buffet problem (i.e. letting the tail deflect and interact dynamically with the flow).

Step 2. Fluid Flow/Tail Deflections Interaction:

With the initial-flow conditions obtained in Step 1 at it = 12,600, the aerodynamic force per unit length $N_r(z,t)$ is provided discretely to the aeroelastic program and the generalized forces $\hat{N}_r$ are computed for six natural mode shapes. The deflections w are computed using Eqs. (14) and (18). Next, Eq. (19) is used to obtain the updated y-coordinates for the grid, the metric coefficients of the Jacobian matrix, the grid speed; and the velocity and acceleration of the points on the tail for the modified boundary conditions for the fluid-flow solution. Next, the fluid flow part is solved and $N_r(z,t)$ is obtained and the computational cycle is repeated. The tail is treated as a homogeneous, uniform, rectangular beam with rectangular cross section of thickness d = 0.01 and width b = 0.5. The dimensionless modulus of elasticity is $E = 0.4903 \times 10^2$ and $EI = 0.0204 \times 10^{-4}$. The dimensionless mass per unit length is m = 11.428. Figure 8 shows the histories of tail deflection, w, and net pressure force per unit length, N, versus the vertical coordinate z every 500 time steps (every 1.5 dimensionless time). The deflection and net pressure force versus time are also shown for the tail midpoint (z = 0.5) and its free-end point z = 1.0. The time-step counter n is for the interaction case only without the time steps for initial conditions (it = 12,600). The early time levels show very large N values with larger values at z = 0.5 than at z = 1.0. The tail deflection w shows a growing oscillatory response reaching a maximum value for the tail free end at n = 3,700 (it = 16,300). Then, the total deflection shows a damped oscillatory response due to the aerodynamic damping of the flow. The aerodynamic damping is automatically included in these results due to the method of solution which considers the fluid flow, the tail aeroelastic deflection and the grid deformation simultaneously. The solutions do not show periodic responses until n = 6,500 (it = 19,100). It is also noticed that all the tail deflections are positive.

Figure 9 shows cross-flow velocities and instantaneous streamlines along the D-ray plane on the right and left sides showing the asymmetric vortex-breakdown flows of the leading-edge vortex cores at n = 6,500 (it = 19,100). In Fig. 10, the instantaneous streamlines are shown in cross-flow planes before and through the vertical tail at chord stations of x = 1.37, 1.51, 1.67, and 1.8. These sections show the asymmetric vortex-breakdown bubbles adjacent to the deflected tail. Figure 11 shows snapshots of the surface pressure contours at two instants, n = 3,150 and 6,500 (it = 15,750 and 19,100) on the two sides of the vertical tail; right side is at J = 1 and left side is at J = $Jdim$. This figure shows the asymmetric unsteady pressure loads which affect the tail.

To show that the tail deflection and its dynamic response affect the flowfield upstream of the tail location, the surface-pressure-coefficient distributions at several chord stations of the wing at it = 19,100 are shown in Fig. 12. Comparing the Cp's of Fig. 1 (it = 12,400) and those of Fig. 12, it is observed that the Cp curves as of x = 0.421 are different. Since the flowfield is subsonic throughout, the disturbances created by the tail deflection and dynamics propagate upstream affecting the flowfield and the vortex-breakdown critical points. Figure 13 shows deformed grids in a cross-flow plane passing through the tail at x = 1.75 at it = 15,750 and 19,100. The grid deformations and the tail deflection are clearly noticed.

In Fig. 14, color graphics of a top view, tilted front view and a three-dimensional view of the wing-tail configuration are shown at it = 19,100. The top view shows the locations of the spiral saddle points on the right and left sides of the wing (their locations are different from those of Fig. 4). The tilted front view shows the trace of the deflected tail and the total-pressure surfaces which show the breakdown of the leading-edge vortex cores. The three-dimensional view shows the whole configuration including the total pressure surfaces, the spiral saddle points and the surface-pressure contours (compare with those of Fig. 5).

CASE 2

With the same delta wing and same flow conditions, the vertical tail aspect ratio is reduced to one (b = 0.5, l_t = 0.5) and its location is changed to the wing trailing edge from x = 1.5 to x = 1.0. The solution for the initial conditions is repeated for this new configuration until it = 12,600. The fluid flow, tail deflection and grid displacement interactions are carried out for n = 4,500 (it = 17,100) with Δt = 0.003. The material properties of the tail are kept fixed.

Figure 15 shows the histories of tail deflection and net pressure force per unit length versus the vertical coordinate z every 500 time steps (every 1.5 dimensionless time). The deflection and net pressure force versus time are also shown for the tail midpoint (z = 0.25) and its free-end point (z = 0.5). The tail deflection shows a growing oscillatory response reaching a maximum value for the midpint at n = 1,200 (it = 13,800). Then, the tail deflection shows a rapidly damped oscillatory response due to the aerodynamic damping of the flow. The tail deflections lead the net pressure forces and the phase lead is more pronounced at the free end of the tail. The solutions do not show a periodic response until n = 4,500 (it = 17,100). However, the tail deflections show positive and negative values. The tail deflections are also noticed to change from the second bending-mode shape to the first bending-mode shape.

Figure 16 shows cross-flow velocities and instantaneous streamlines along the D-ray plane on the right and left sides showing the asymmetric vortex-breakdown flows of the leading-edge vortex cores at n = 4,500 (it = 17,100). In Fig. 17, the instantaneous streamlines are shown in cross-flow planes passing through the tail at x = 1.01, 1.18, 1.38 and 1.5. These sections show the asymmetric vortex-breakdown bubbles adjacent to the tail surface and covering a larger height of the tail than those of Fig. 10 (the tail height here is one-half the tail height of Case 1).

In Fig. 18, color graphics of a top view, a tilted front view and a three-dimensional view of the wing-tail configuration are shown at it = 17,100. Comparing these views with those of Fig. 14, it is observed that the spiral saddle points of vortex breakdown, surface pressure and total-pressure surfaces are different from those of Fig. 14. Again, this shows conclusively that location, shape, deflections, and dynamics of the tail substantially affect the flowfield upstream of the tail, i.e.; on the wing. In Fig. 8, the tail deflection is noticed in the top view and the three-dimensional view as well.

CONCLUDING REMARKS

The buffet problem of a vertical tail due to the interaction of vortex-breakdown flow with the tail has been simulated computationally and efficiently using a delta wing-vertical tail configuration. The wing aspect ratio and flow conditions have been carefully selected in order to produce an unsteady vortex-breakdown flow. The solution has demonstrated the development of the tail buffet due to the unsteady loads produced by the vortex-breakdown flow. The problem is a multidisciplinary problem which requires three sets of equations to obtain its solution. The first set is the unsteady Navier-Stokes equation which is used to obtain the aerodynamics force per unit length on the tail. The second set is the aeroelastic equation for bending vibrations which is used to obtain the tail deflections, velocities and accelerations. The third set is the grid displacement equation which is used to update the grid coordinates due to the tail deflections. The three sets of equations are solved sequentially and accurately in time. The computational applications included two cases of delta wing-vertical tail configurations. Fixing the flow conditions and the geometry of the delta wing, two tail aspect ratios and locations are used. Initially, tail deflections and aerodynamic loads were higher for the first case than the second case. Later on, the deflections were damped due to the aerodynamic damping of the flow. The solutions show that the tail location, shape, deflections and dynamics affect the flowfield upstream of the tail. Work is underway to include torsional modes to the bending modes, upgrade the tail model from beam equations to plate equations, and consider the wing-twin vertical tail configuration.

ACKNOWLEDGEMENT

This research work is supported under Grant No. NAG-1-648 by the NASA Langley Research Center and the Air Force Office for Scientific Research, Bolling AFB. The authors would like to recognize the computational resources provided by the NAS facilities at Ames Research Center and the NASA Langley Research Center.

REFERENCES

1. Sellers, W. L. III, Meyers, J. F. and Hepner, T. E., "LDV Survey Over a Flighter Model at Moderate to High Angle of Attack," SAE Paper 88–1448, 1988.

2. Erickson, G. E., Hall, R. M., Banks, D. W., Del Frate, J. H., Shreiner, J. A., Hanley, R. J., and Pulley, C. T., "Experimental Investigation of the F/A-18 Vortex Flows at Subsonic Through Transonic Speeds," Invited Paper, AIAA 89–2222, 1989.

3. Wentz, W. H., "Vortex-Fin Interactions on a Fighter Aircraft," AIAA 87–2474, AIAA Fifth Applied Aerodynamics Conference, Monterey, CA, August 1976.

4. Lee, B. and Brown, D., "Wind Tunnel Studies of F/A-18 Tail Buffet," AIAA 90–1432, 1990.

5. Rao, D. M., Puram, C. K. and Shah, G. H., "Vortex Control for Tail Buffet Alleviation on a Twin-Tail Fighter Configuration," SAE Paper No. 89–2221, 1989.

6. Cole, S. R., Moss, S. W. and Doggett, R. V., Jr., "Some Buffet Response Characteristics of a Twin-Vertical-Tail Configuration," NASA TM-102749, October 1990.

7. Edwards, J. W., "Assessment of Computational Prediction of Tail Buffeting," NASA TM 101,613, January 1990.

8. Kandil, O. A., Kandil, H. A. and Liu, C. H., "Three-Dimensional Supersonic Vortex Breakdown," AIAA 93–0526, January 11–14, 1993.

9. Kandil, O. A., Kandil, H. A. and Liu, C. H., "Shock-Vortex Interaction Over a 65–Degree Delta Wing in Transonic Flow," AIAA Paper 93–2973, AIAA 24th Fluid Dynamics Conference, Orlando, FL, July 6–9, 1993.

10. Ide, H. and Shankar, V. J., "Unsteady Full Potential Aeroelastic Computations for Flexible Configurations," AIAA 87–1238, June 1987.

11. Schuster, D., Vadyak, J. and Atta, E., "Static Aeroelastic Analysis of Fighter Aircraft Using a Three-Dimensional Navier-Stokes Algorithm," AIAA 90–0435, January 1990.

12. Kennon, S. R., "Supersonic Inlet Calculations Using an Upwind Finite-Volume Method on Adaptive Unstructured Grids," AIAA-89-0113, January 1989.

13. Morgan, K., Peraive, J., Thareja, R. R. and Stewart, J. R., "An Adaptive Finite Element Scheme for the Euler and Navier-Stokes Equations," AIAA-87-1172, June 1987.

14. Batina, J., "Unsteady Euler Airfoil Solutions Using Unstructured Dynamic Meshes," AIAA 89-0115, January 1989.

15. Kandil, O. A., Chuang, H. A. and Salman, A. A., "Unsteady Flow Computation of Oscillating Flexible Wings," AIAA-90-0937-CP, April 1990, pp. 1370–1381.

16. Kandil, O. A. and Salman, A. A., "Unsteady Vortex-Dominated Flow Around Wings with Oscillating Leading-Edge Flaps," AIAA 91-0435, January 1991.

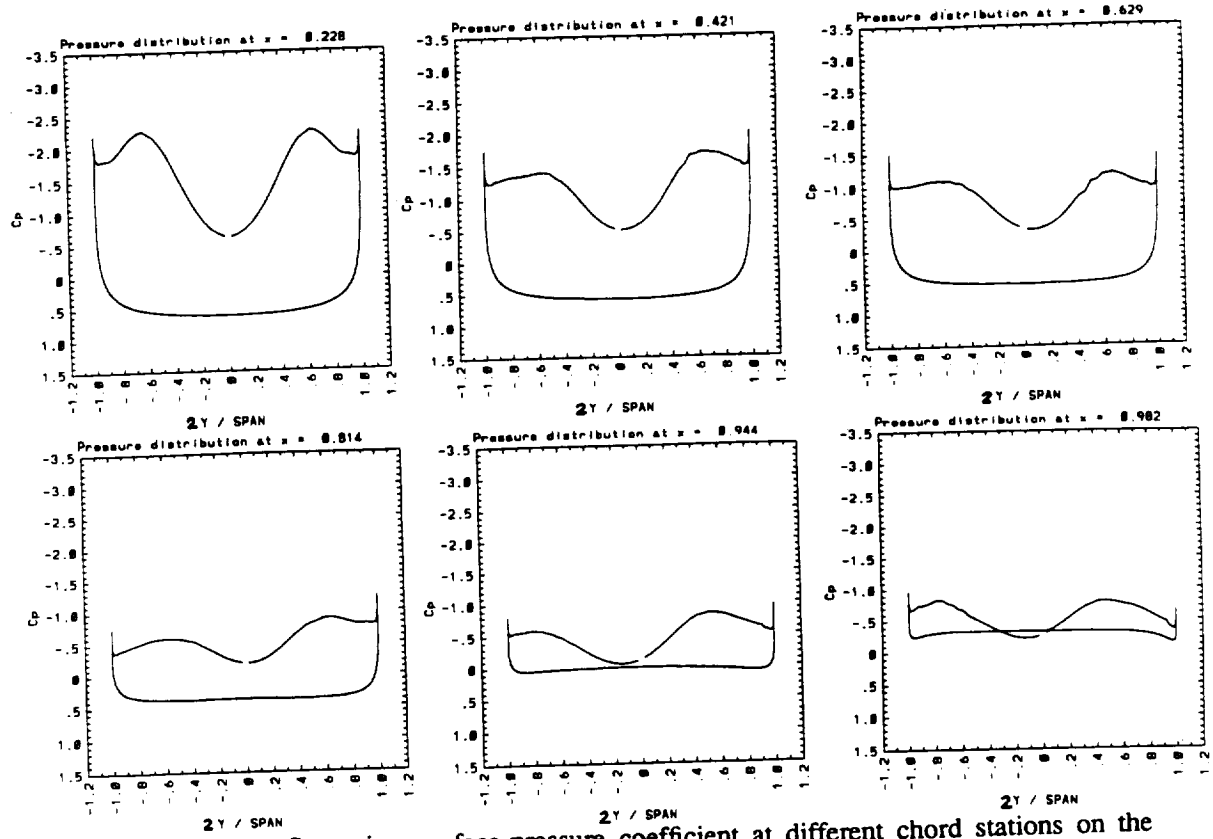

Fig. 1. Spanwise, surface-pressure coefficient at different chord stations on the wing; $AR_w = 1$, $AR_T = 2$, $M_\infty = 0.4$, $\alpha = 35°$, $R_e = 10^4$, $it = 12,400$.

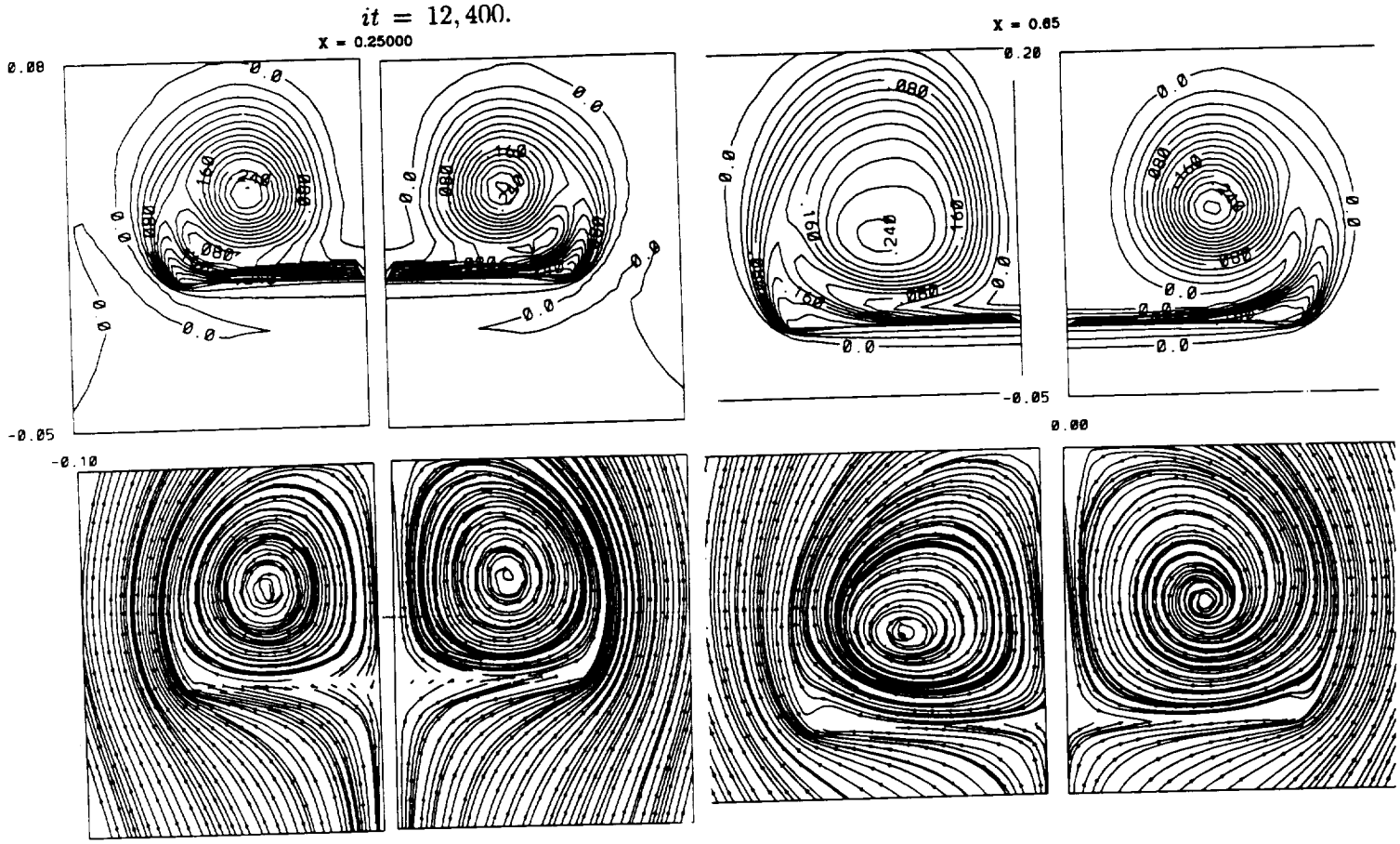

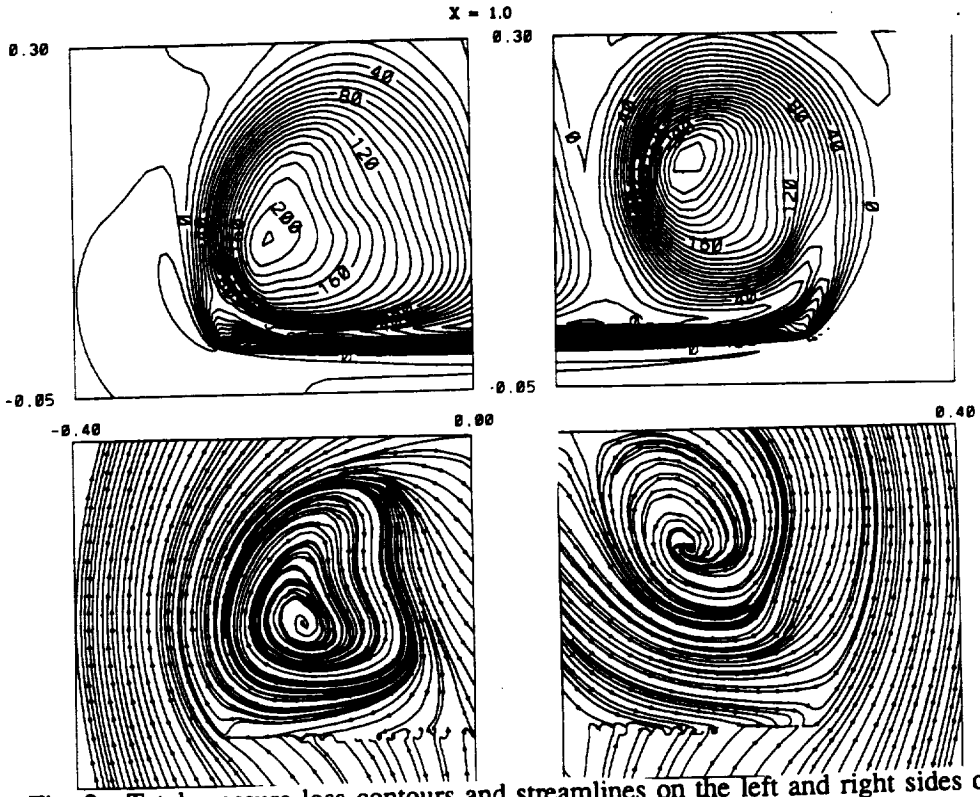

Fig. 2. Total-pressure-loss contours and streamlines on the left and right sides of the wing at different chord stations; $AR_w = 1$, $AR_T = 2$, $M_\infty = 0.4$, $\alpha = 35°$, $R_e = 10^4, it = 12,400$.

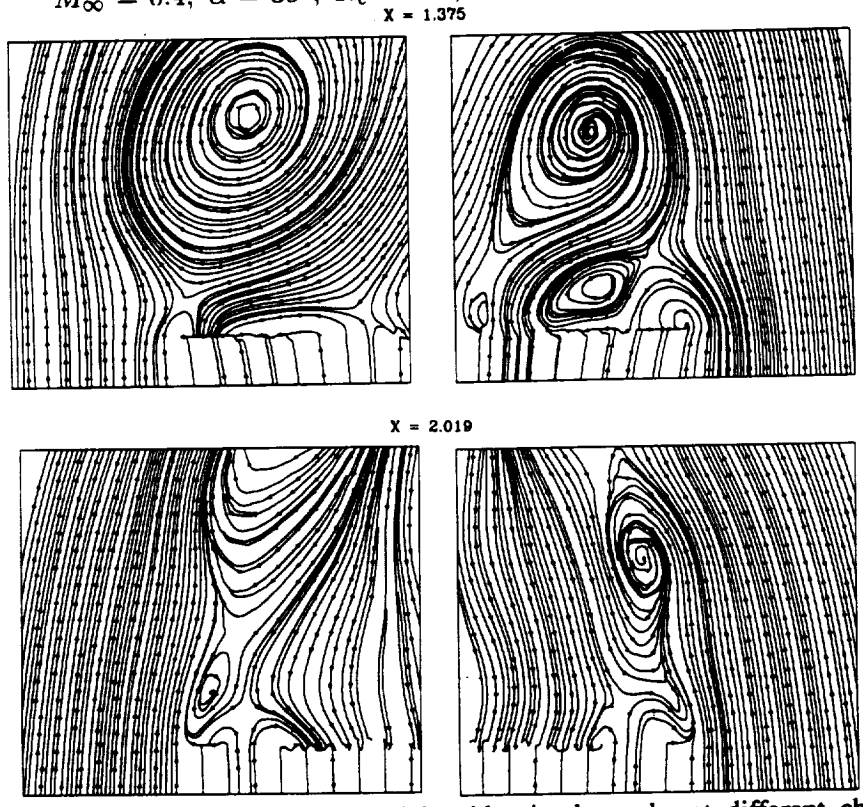

Fig. 3. Streamlines on the left and right sides in the wake at different chord stations; $AR_w = 1$, $AR_T = 2$, $M_\infty = 0.4$, $\alpha = 35°$, $R_e = 10^4$, $it = 12,400$.

Fig. 4. Top view showing surface-pressure contours and streamlines in the vortex cores showing their spiral-vortex breakdown, $AR_w = 1$, $AR_T = 2$.

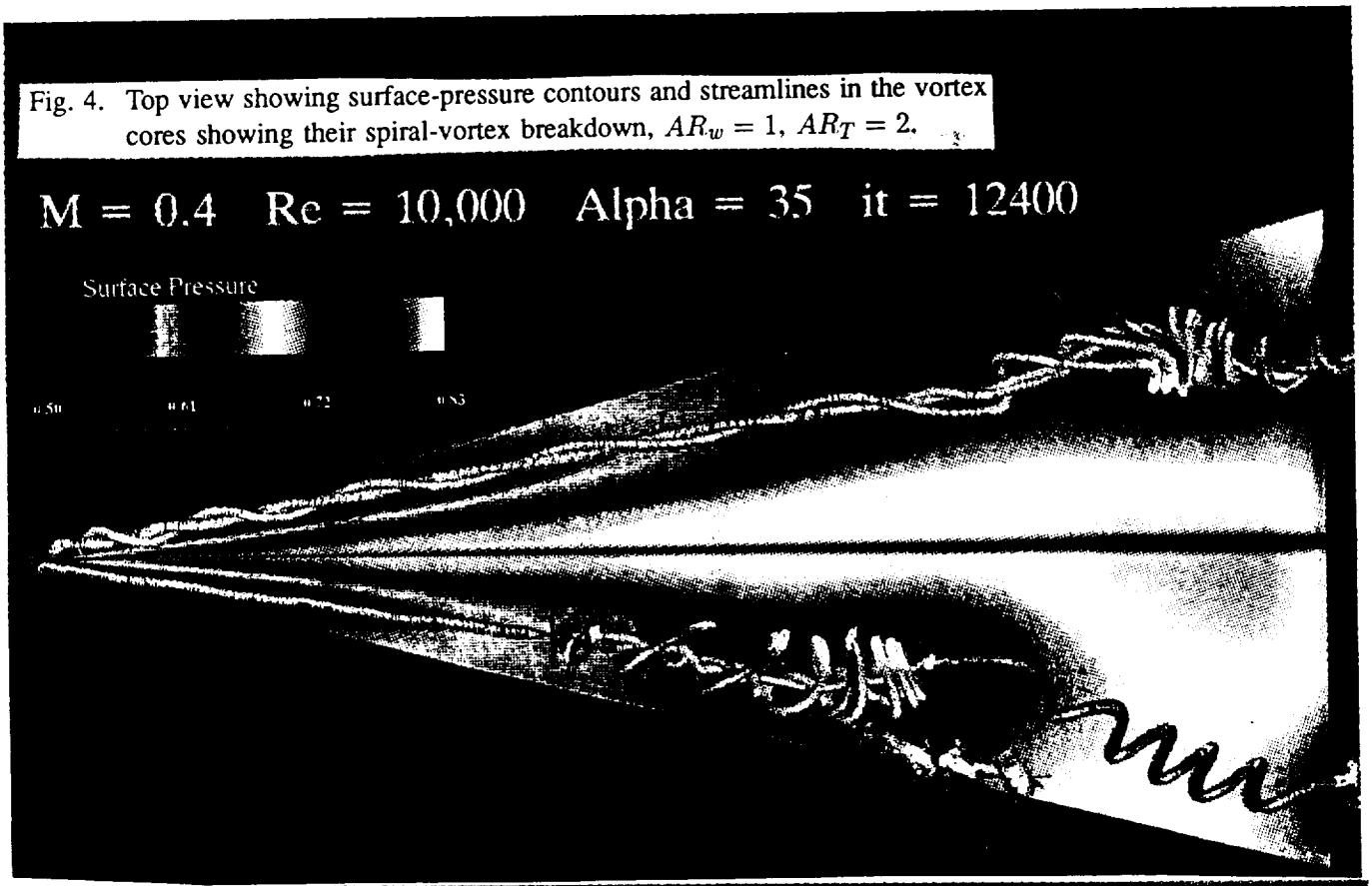

Fig. 5. Three-dimensional view of delta wing-vertical tail configuration showing the spiral vortex breakdown of vortex cores, $AR_w = 1$, $AR_T = 2$.

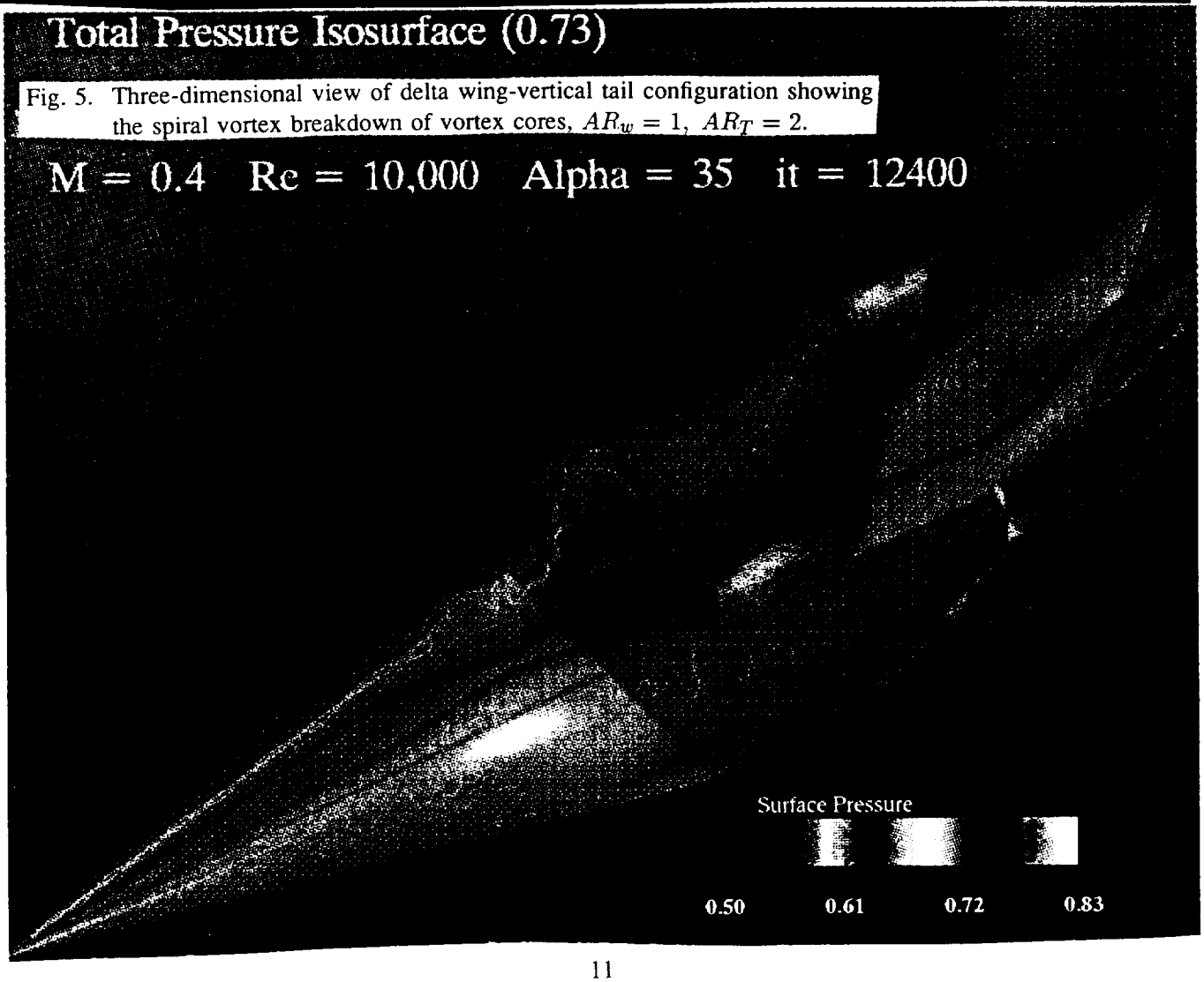

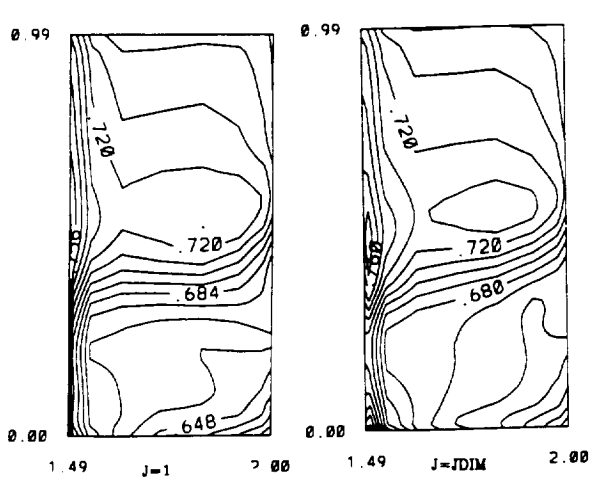

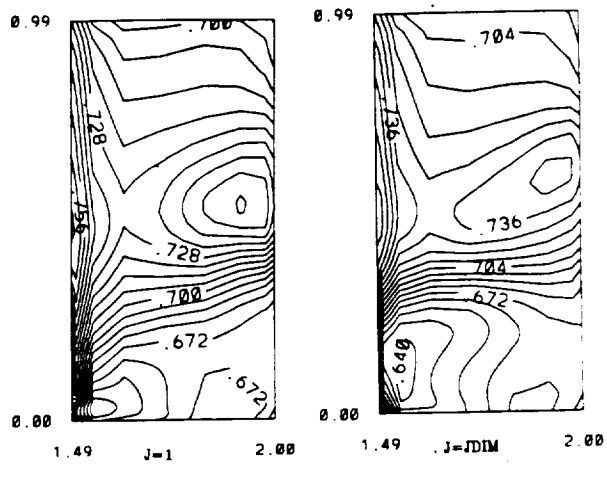

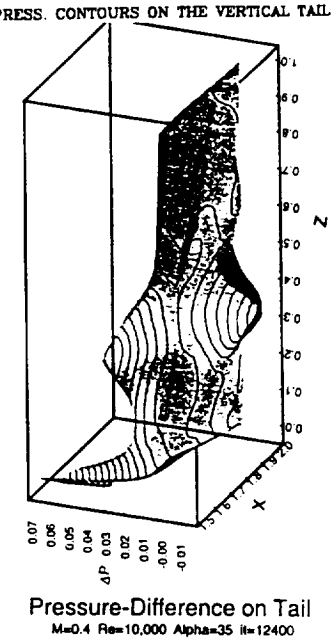

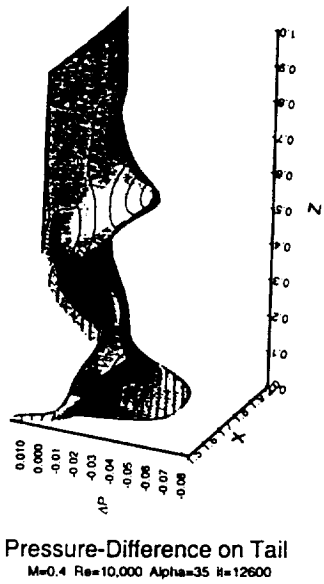

Fig. 6. Pressure contours on the right ($J = 1$) and left ($J = JDIM$) surfaces of the tail and the pressure difference at two time levels, $it = 12,400$; $it = 12,600$.

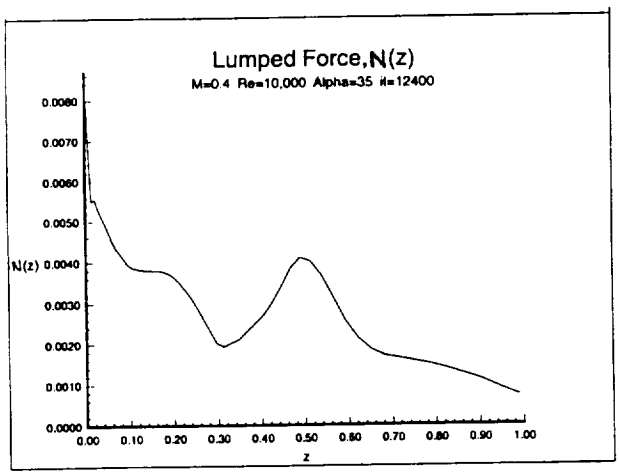

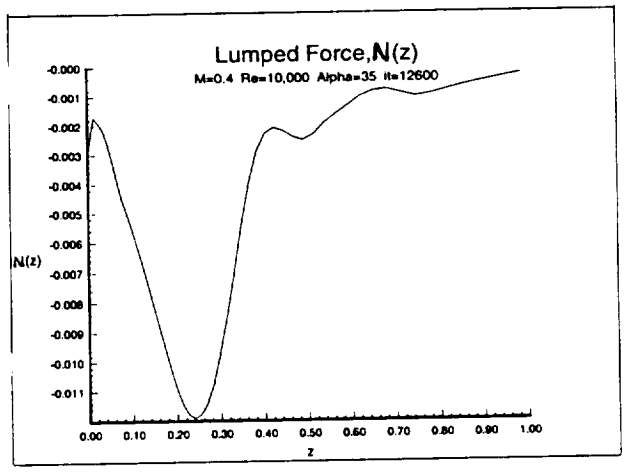

Fig. 7. Lumped force per unit length on the tail at two time levels; $it = 12,400$; $it = 12,600$.

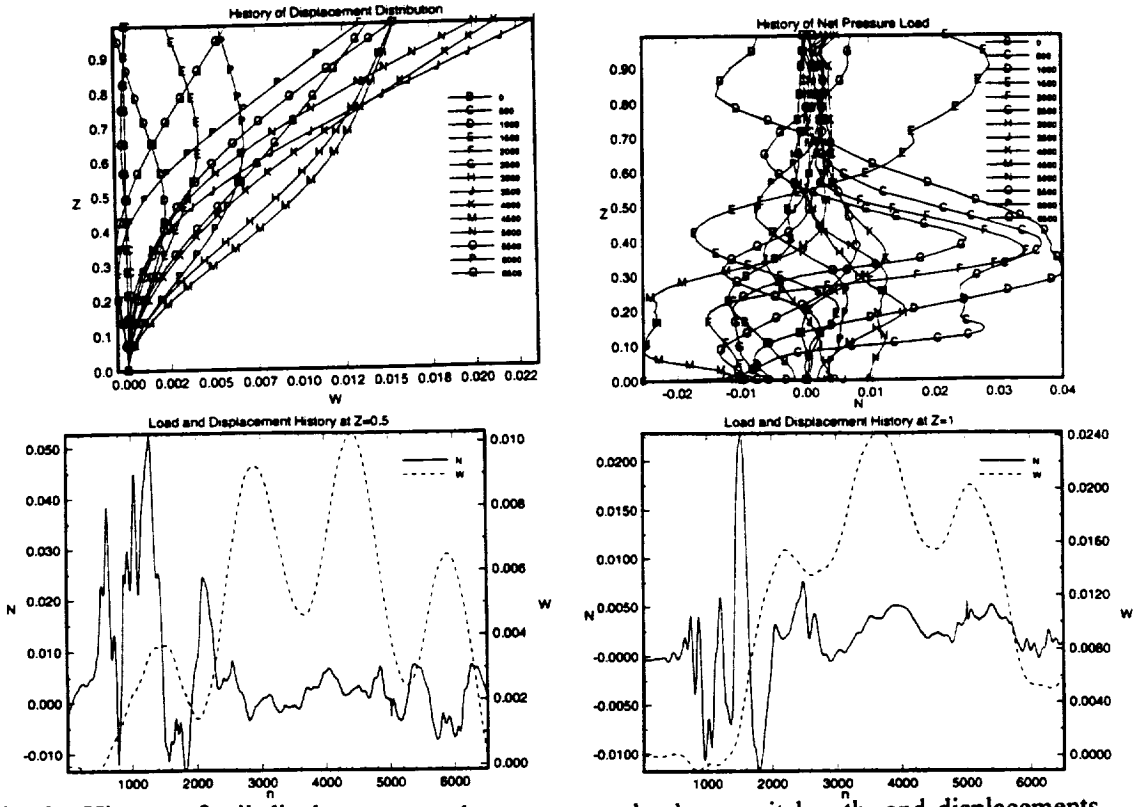

Fig. 8. History of tail displacement and net pressure load per unit length, and displacements of midpoint and free end; $E = 0.4903 \times 10^3$, $m = 11.428$, $l_t = 1$, $AR_T = 2$.

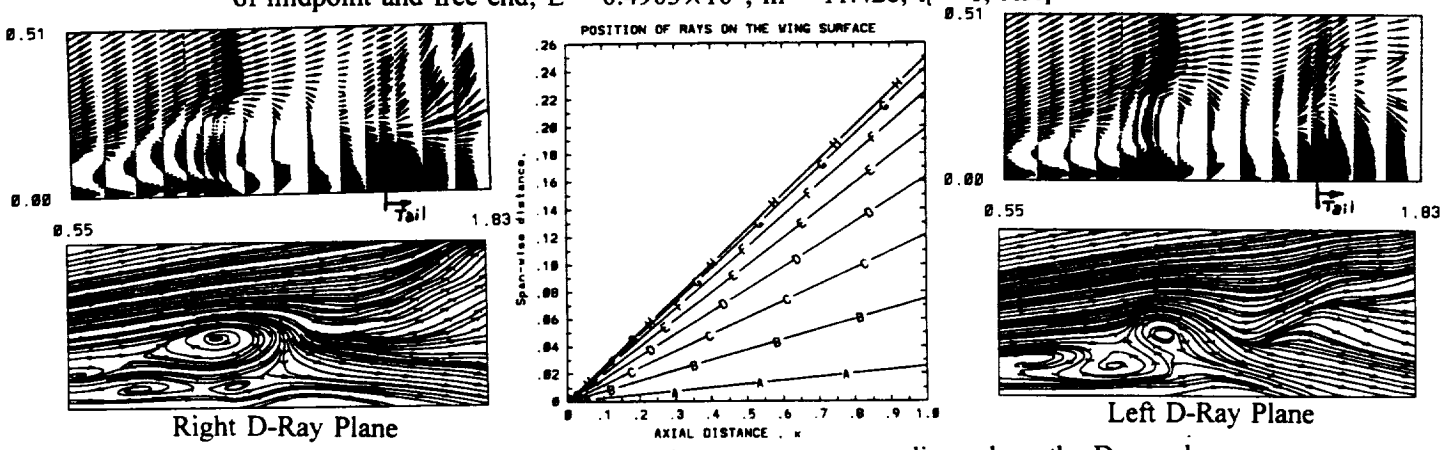

Fig. 9. Cross-flow velocities and instantaneous streamlines along the D-ray plane on the right and left sides of wing, it = 19,100, $\Delta t = 0.003$, $AR_t = 2$.

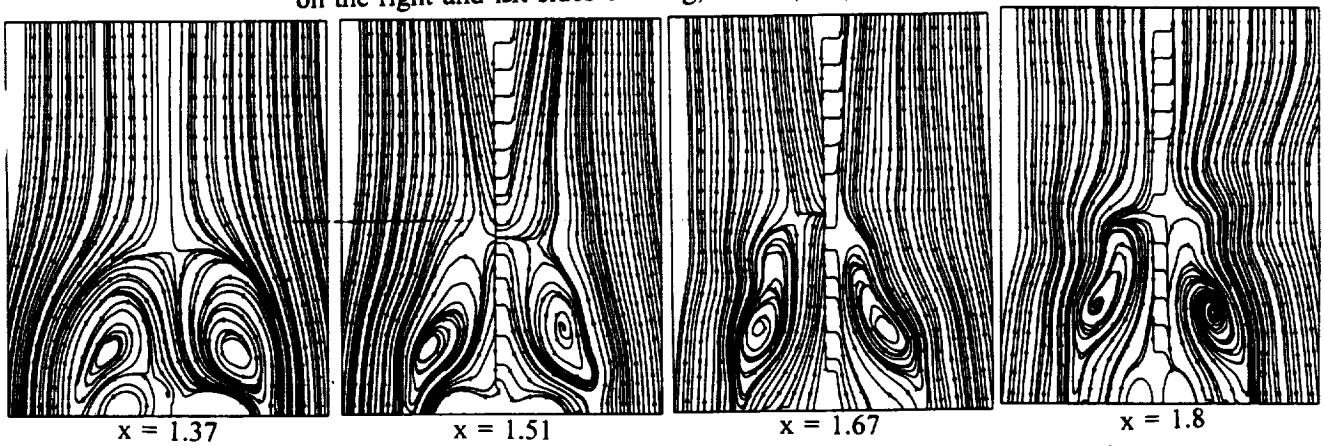

Fig. 10. Cross-flow instantaneous streamlines at different chord stations before and through the tail, it = 19,100, $\Delta t = 0.003$, $AR_T = 2$.

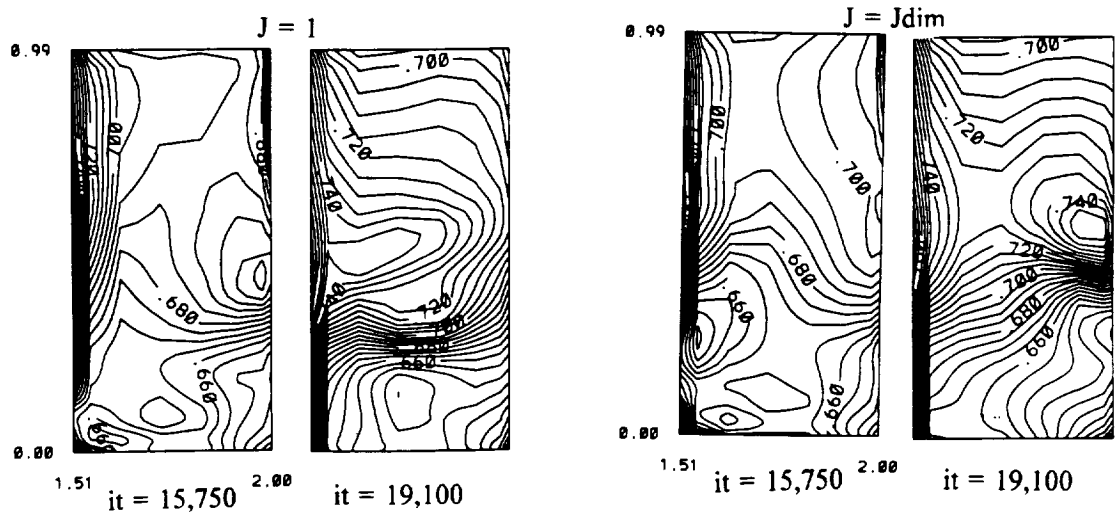

Fig. 11. Pressure contours on the right (J = 1) and left (J = Jdim) surfaces of the tail at two time levels, it=15,750 and it = 19,100, $AR_T = 2$.

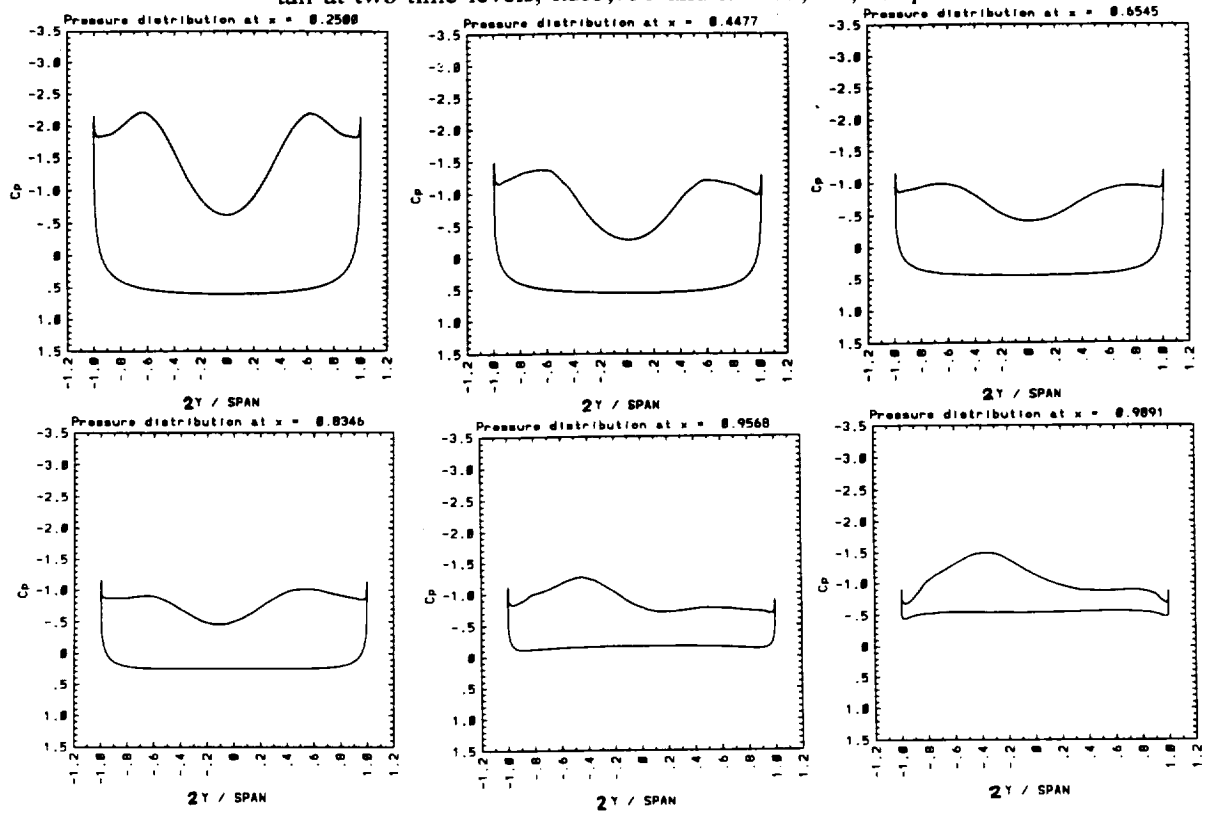

Fig. 12. Spanwise surface-pressure coefficient at different chord stations, it = 19,100, $AR_T = 2$.

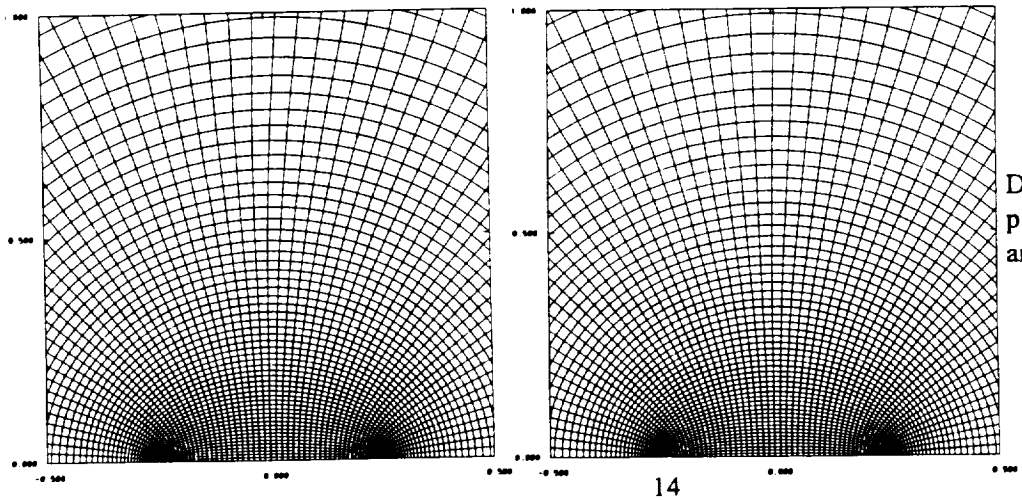

Fig. 13. Deformed grid in cross-flow plane at x = 1.75, at it = 15,750 and it = 19,100, $AR_T = 2$.

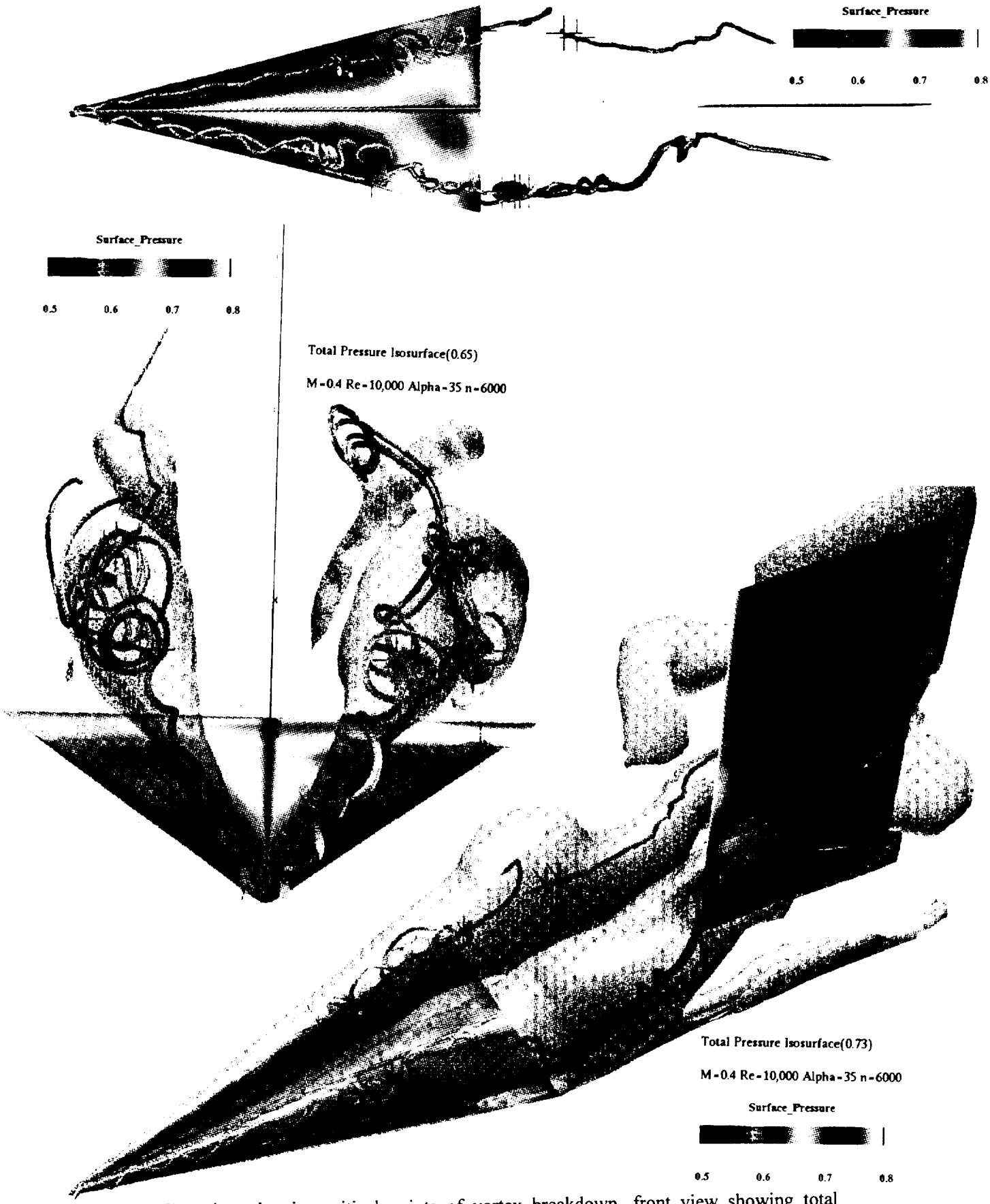

Fig. 14. Top view showing critical points of vortex breakdown, front view showing total pressure surfaces and tail deflection, and three-dimensional view showing the delta wing — vertical tail configuration, it = 19,100, AR_T = 2.

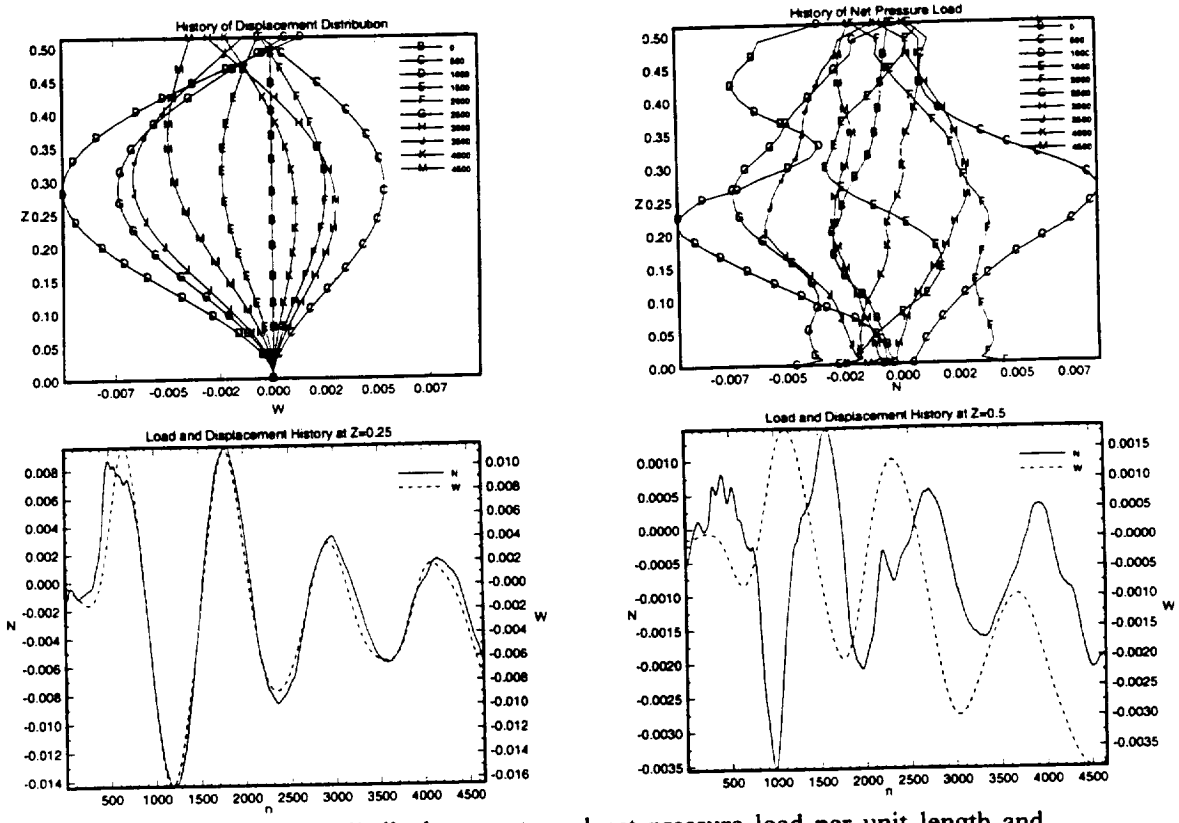

Fig. 15. History of tail displacements and net pressure load per unit length and displacements of midpoint and free end, E = 0.4903×10^3, m = 11.428, l_t = 0.5, AR_T = 1.

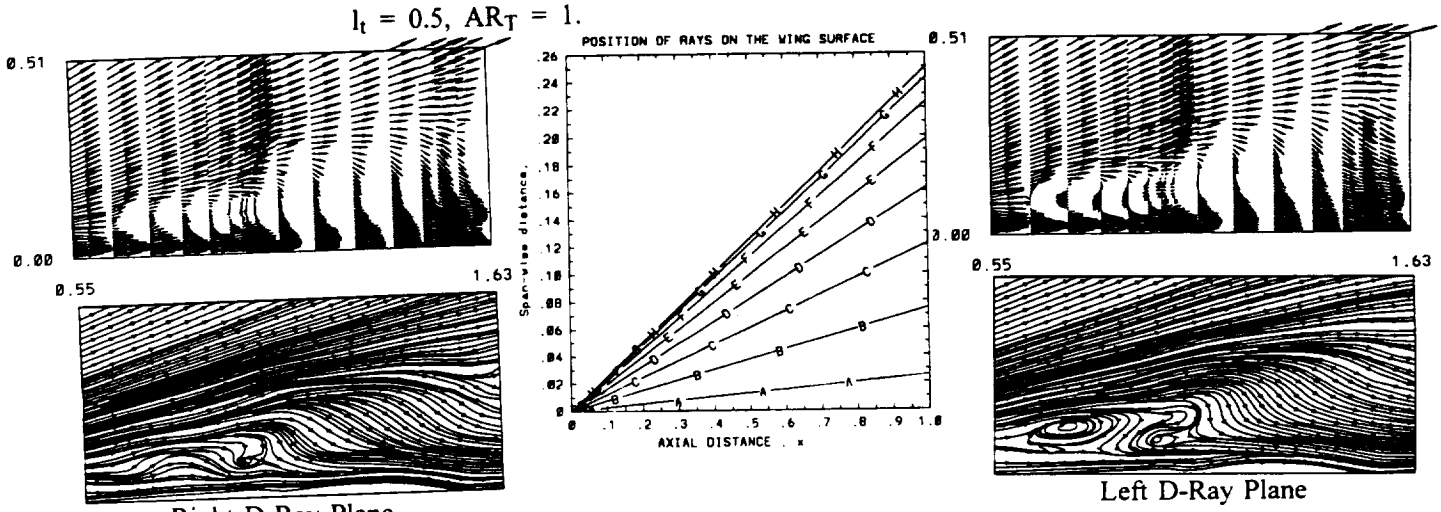

Fig. 16. Cross-flow velocities and instantaneous streamlines along the D-ray plane on thc right and left side of wing, it = 17,100, Δt = 0.003, AR_T= 1.

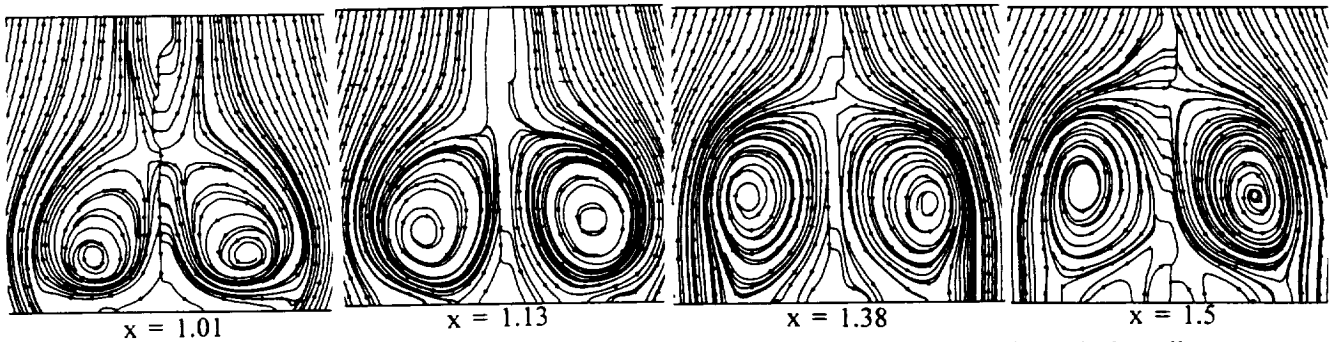

Fig. 17. Cross-flow instantaneous streamlines at different chord stations through the tail, it = 17,100, Δt = 0.003, AR_t = 1.

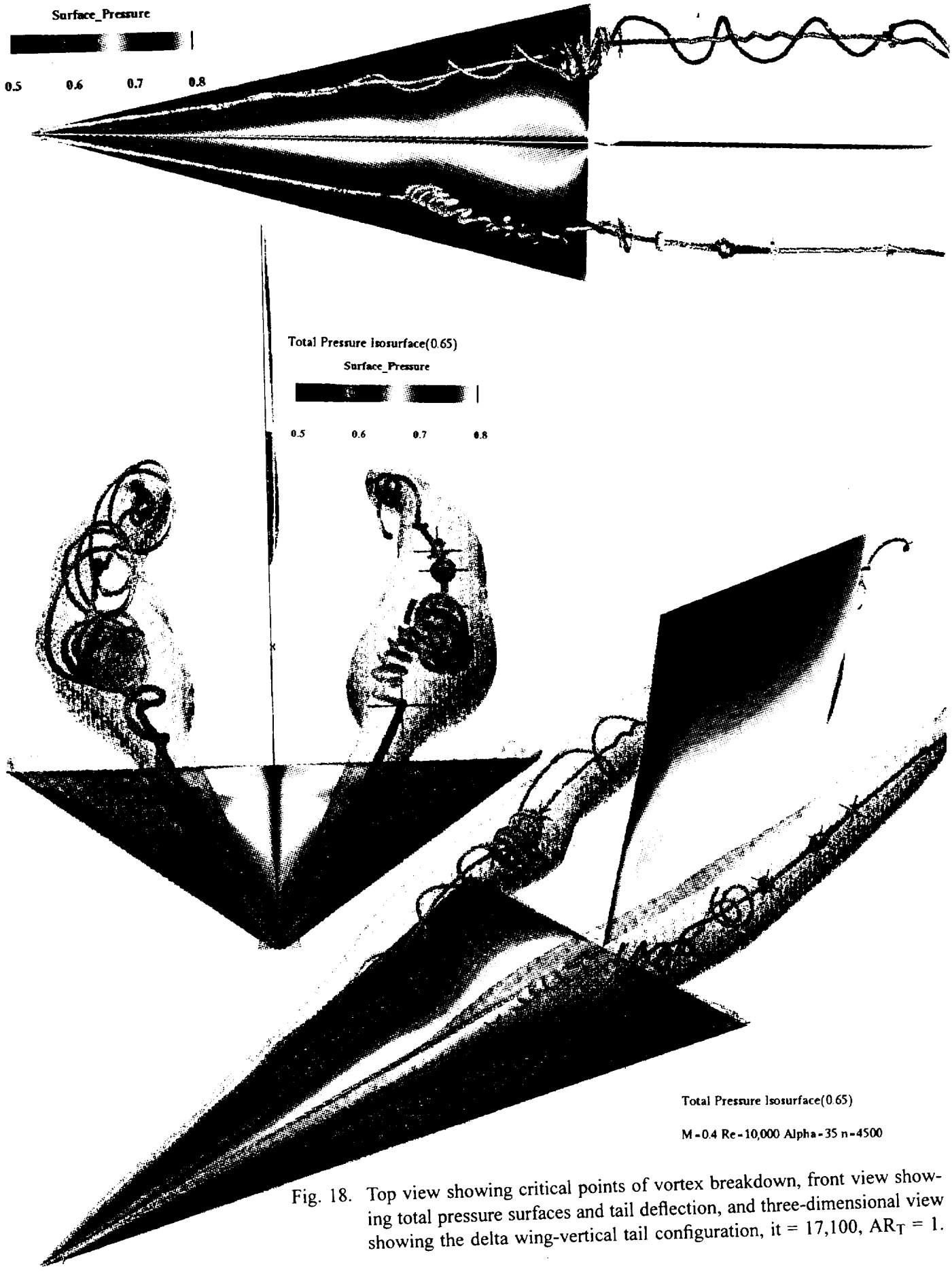

Fig. 18. Top view showing critical points of vortex breakdown, front view showing total pressure surfaces and tail deflection, and three-dimensional view showing the delta wing-vertical tail configuration, it = 17,100, $AR_T = 1$.

AIAA-93-2973

SHOCK-VORTEX INTERACTION OVER A 65-DEGREE DELTA WING IN TRANSONIC FLOW

Osama A. Kandil and Hamdy A. Kandil
Old Dominion University, Norfolk, VA 23529

C. H. Liu
NASA Langley Research Center, Hampton, VA 23681

AIAA 24th
Fluid Dynamics Conference
July 6-9, 1993 / Orlando, FL

SHOCK-VORTEX INTERACTION OVER A 65–DEGREE DELTA WING IN TRANSONIC FLOW

Osama A. Kandil* and Hamdy A. Kandil**
Old Dominion University, Norfolk, Virginia 23529
and
C. H. Liu***
NASA Langley Research Center, Hampton, VA 23681

ABSTRACT

Transonic flow over a 65–degree swept-back, sharp-edged, cropped delta wing is investigated computationally using the time-accurate solution of the unsteady, compressible, full Navier-Stokes equations with an implicit, upwind, flux-difference splitting, finite-volume scheme. Coarse and fine O-H grids are used to obtain the solution. The grid consists of $125\times85\times84$ points in the wrap-around, normal and axial directions, respectively. The results are presented for an angle of attack of 20°, March number of 0.85 and Reynolds number of 3.23×10^6 (based on the wing chord length). With the fine grid, the results show that a system of shocks has been captured over the upper wing surface, and that the leading-edge vortex core experiences an unsteady, supersonic vortex breakdown after passing through a spanwise shock (terminating shock) near the wing trailing edge. The computed results at a certain time are in good agreement with the experimental data. Topological aspects of the vortex-breakdown flowfield are also presented and discussed.

INTRODUCTION

At sufficiently high angles of attack, vortex breakdown for incompressible flows around delta wings has been observed along the leading-edge primary vortex cores. Two distinct forms of vortex breakdown have been documented experimentally[1]. The first form is the bubble type and the second form is the spiral type. The bubble type shows an almost axisymmetric sudden swelling of the vortex core into a bubble, while the spiral type shows an asymmetric, spiral, vortex filament followed by a rapidly spreading turbulent flow. Both types are characterized by an axial stagnation point and a limited region of reversed axial flow. Much of our knowledge of incompressible vortex breakdown has been obtained from experimental studies of pipe flows where both types of breakdown and other types as well were generated and documented[2–4].

The major effort of computational study of vortex breakdown flows has also been focused on isolated swirling flows. For incompressible flows, quasi-axisymmetric, bubble-type, vortex-breakdown flows were computed using the Navier-Stokes equations[5–8]. Three-dimensional bubble and spiral vortex-breakdown flows were also computed for isolated swirling flows using the three-dimensional Navier-Stokes equations in the vorticity-velocity form or the primitive variables form[9–11].

Interaction between a longitudinal vortex and a transverse shock wave occurs in several flow applications which include transonic and supersonic flows over a delta wing or a strake-wing configuration at moderate to high angles of attack, a supersonic inlet ingesting a vortex, and a supersonic combustor where fuel is injected in a swirling jet to enhance fuel-air mixing[13–14]. For delta wings and strake-wing configurations, vortex breakdown is an undesirable phenomenon since it produces wing stall. Therefore, its occurrence needs to be delayed with passive or active control methods in order to increase the wing performance at large angles of attack. For a supersonic combustor, vortex breakdown is desirable since it enhances mixing of air and fuel and stabilizes the flame[15,16]. Therefore its occurrence needs to be enhanced and controlled.

For supersonic flows, quasi-axisymmetric bubble-type vortex-breakdown[17–19] and three-dimensional bubble-type and spiral-type vortex breakdown[20] for isolated swirling flows have been recently computed by the present authors. Using compatible, inlet boundary conditions, the time-accurate solutions of the unsteady, compressible, full Navier-Stokes equations were obtained to study the effects of Reynolds number, Mach number, swirl ratio, type of exit-boundary conditions and grid fineness and distribution on the vortex-breakdown modes for internal and external flows. Several modes of vortex breakdown which include transient single-bubble, transient multi-bubble, periodic multi-frequency multi-bubble, quasi-steady two-bubble cell and spiral-type vortex breakdowns have been obtained[21]. For three-dimensional vortex-breakdown flows in a swirling, supersonic jet flow, topological aspects of the critical points in the vortex-breakdown region have been studied and compared with the available experimental incompressible vortex-breakdown topology.

Recent experimental measurements[22–26] of transonic

* Professor, Eminent Scholar and Chairman of Aerospace Engineering Department, Associate Fellow AIAA.
** Research Associate, Aerospace Engineering Department, Member AIAA.
*** Senior Research Scientist, Computational Aerodynamics Branch, Associate Fellow AIAA.

flows around a 65° swept-back, cropped delta wing show that shock wave formation is likely to occur underneath the leading-edge primary vortex core. In cross-flow planes perpendicular to the wing, the cross-flow beneath the primary vortex reaches supersonic speeds and a cross-flow shock develops beneath the primary vortex similar to the supersonic flow in a convergent-divergent nozzle. These measurements also show that a transverse shock "terminating shock" which might cause primary-vortex-core breakdown could develop in an analogous manner to the shock that terminates the two-dimensional supersonic pocket on an airfoil. A complete reconstruction of the three-dimensional flow field on the delta wing in this region was not possible experimentally[22-26]. Computational simulations for transonic delta-wing flows have been developed by using the Euler equations[27,28] and the thin-layer, Navier-Stokes equations[29]. The Euler-equations solutions were not capable of fully resolving the flow in the terminating shock region and the thin-layer, Navier-Stokes solution did not address that region.

In the present paper, we consider the transonic flow around a 65° sharp-edged, cropped delta wing at an angle of attack of 20°, a Mach number of 0.85 and a Reynolds number of 3.23×10^6. The purpose of the present numerical simulation and study is to construct the flow field over the wing with particular emphasis of the vortex core-terminating shock interaction region. The laminar, unsteady, compressible, full Navier-Stokes equations are solved accurately in time with an implicit, flux-difference splitting, finite-volume scheme. The computations are carried out with time-accurate stepping on two O-H grids; a coarse grid and a fine grid. Both grids consist of $125\times85\times84$ points in the wrap-around, normal and axial directions, respectively. The main difference between the coarse and fine grids is the distribution of the grid points normal to the wing surface within the thin viscous layer (to be discussed later on).

HIGHLIGHTS OF FORMULATION AND COMPUTATIONAL SCHEME

The conservative form of the dimensionless, unsteady, compressible, full Navier-Stokes equations is used for the formulation of the problem. The equations are written in terms of the time-independent, body-conformed coordinates ξ^1,ξ^2 and ξ^3 (Ref. 18).

The implicit, upwind, flux-difference splitting, finite-volume scheme is used to solve the unsteady, compressible, full Navier-Stokes equations. The scheme uses the flux-difference splitting scheme of Roe which is based on the solution of the approximate one-dimensional, Riemann problem. In the Roe scheme, the inviscid flux difference at the interface of computational cells is split into two parts; left and right flux differences. The splitting is accomplished according to the signs of the eigenvalues of the Roe averaged-Jacobian matrix of the inviscid fluxes at the cell interface. The smooth flux limiter is used to eliminate oscillations at locations of large flow gradients. The viscous- and heat-flux terms are linearized in time and the cross-derivative terms are neglected in the implicit operator and retained in the explicit terms. The viscous terms are differenced using a second-order accurate central differencing. The resulting difference equation is approximately factored and is solved in three sweeps in the ξ^1,ξ^2 and ξ^3 directions. The computational scheme is coded in the computer program "FTNS3D" which is a modified version of the CFL3D-code.

COMPUTATIONAL RESULTS

A 65° swept-back, sharp-edged, cropped delta wing with zero thickness is considered for the computational solutions. The cropping ratio (tip length/root-chord length) is 0.15. The wing angle of attack is 20°, and the freestream Mach number and Reynolds number (based on the root-chord length) are 0.85 and 3.23×10^6, respectively. The reason behind the present, selected flow conditions is because of the uncertainty of the existing experimental data[22-26] about the structure of the downstream flow field of the leading-edge vortex core. The experimental data shows that a supersonic flow region appears on the upper wing surface near the plane of symmetry. This flow region is terminated by a transverse shock (known as a terminating shock) in a similar way to the shock that terminates a supersonic pocket on a supercritical airfoil[23].

Grid:

An O-H grid of $125\times85\times84$ in the wrap-around, normal and axial directions, respectively, is used for the computational simulation. The computational domain extends two-chord length forward and five-chord length backward from the wing trailing edge. The radius of the computational domain is four-chord length. Two grids have been constructed using the same number of grid points. The first is called the coarse grid and the second is called the fine grid. For the coarse grid, the grid points in the cross flow planes have been distributed using a Joukowski transformation which produces a minimum grid size, normal to the wing surface, that varies from 5×10^{-4} at the leading edge to 3×10^{-2} at the plane of symmetry. For the fine grid, the elliptical grid lines in the cross-flow planes have been constructed such that the minimum grid size normal to the wing surface, stays constant at 5×10^{-4} from the leading edge to the plane of symmetry. Figures 1 and 2 show three-dimensional shape of the coarse and fine grids and a cross-flow plane along with its blow-ups.

Time-accurate integration of the laminar, unsteady, compressible, full Navier-Stokes equations has been carried out with $\Delta t = 0.001$ for the coarse grid and $\Delta t = 0.0002$ for the fine grid. The results showed that the leading-edge vortex core passes through a terminating shock which causes the vortex core to breakdown. Moreover, it is shown that the flow becomes unsteady behind the terminating shock.

Validation of Surface Pressure:

Figure 3 shows a comparison of the computed, spanwise surface-pressure coefficient (C_p) at different chord stations for the fine and coarse grids with the experimental data of Erickson[30] ($R_e = 3.23\times10^6$) and Hartmann[24] ($R_e = 2.38\times10^6$ and 4.57×10^6). The computed results are selected at t = 3.6. Obviously, the coarse-grid C_p-curves do not show the suction-pressure peak corresponding to the secondary vortex and the correct location of the suction-pressure peak corresponding to the primary vortex. The coarse-grid C_p-curves are similar to those of the Euler-equations solution. Therefore, they are discarded in this paper. The fine-grid C_p-curves show the correct location of the suction-pressure peak corresponding to the primary vortex and the suction-pressure peak corresponding to the secondary vortex. The fine-grid C_p-curves at x = 0.3, 0.6 and 0.8 are in fair to good agreement with the experimental data. For x = 0.9, the fine-grid C_p-curve shows a substantial, rapid increase in the pressure coefficient (a decrease in the suction pressure). Figure 4 shows the total-Mach contours and the streamlines in cross-flow planes at the chord stations of x = 0.3, 0.6, 0.8, 0.9, 0.97 and 1.0. At x = 0.3, 0.6 and 0.8, the total-Mach contours show an oblique shock under the primary vortex and a small subsonic region to the right of the shock. The streamlines show the secondary separation to the right of the shock. This separation is due to the shock interaction with the surface boundary-layer flow and is also due to the adverse, spanwise pressure gradient created by the primary vortex. At x = 0.9, the shock under the primary vortex becomes weak as observed in the total-Mach contours and the primary-vortex size increases. At x = 0.97, the shock under the primary vortex disappears and the primary vortex diffuses and reduces to a repelling focus as shown by the streamlines. At x = 1.0, the repelling focus becomes a repelling line. The details of the flow structure shown at x = 0.9, 0.97 and 1.0 indicate that the primary vortex is going through a breakdown mode which is caused by a transverse shock (terminating shock) between x = 0.8 and x = 0.9.

Terminating Shock:

To show that a terminating, transverse shock exists and has been captured computationally, the static-pressure contours and total-Mach-contours on two planes are computed and displayed in Fig. 5. In this figure, the static-pressure contours are shown on the wing surface and the plane of symmetry, and the total-Mach contours are shown on the third plane (k = 3) above the wing (in the viscous layer) and on the plane of symmetry. The plane of symmetry contours clearly show the location, shape and strength of the terminating shock. Moreover, the Mach contours show that a substantial supersonic pocket (bounded by the sonic line and terminating shock) extends from the wing vertex to the shock location of x = 0.83, which is in good agreement with the experimental data[30], where the shock is located at x = 0.84. The computed results show that the shock is a normal shock with a height of 0.4 which is equal to one-half the wing span. In the spanwise direction, the shock foot print (shown on the Mach contours at k = 3) extends beyond the primary-vortex location. A λ-type shape of the shock-system foot print, which on one side of the wing, consists of the terminating shock and the shock under the primary vortex that runs along a ray plane from the wing vertex, is seen on the Mach contours at k = 3.

Figure 6 shows the position of the ray lines from the wing vertex (which are marked by the letters A-H) and the static-pressure curves along these lines. The static-pressure curves show the spanwise locations of several points on the foot-print line of the terminating shock. The terminating shock is clearly seen to run in the spanwise direction from the plane of symmetry to the wing leading edge. It reaches its highest strength from the location of the primary vortex to the wing leading edge (from line E to line H).

Vortex-Breakdown Structure:

Having established the shock system that consists of the shock under the primary vortex and the terminating shock, the focus is directed on the structure of the flow behind the terminating shock. In Fig. 7, we show the total-Mach contours and streamlines on a ray plane at the 0.658 spanwise location, which passes through the leading-edge vortex core. Blow-ups of the velocity vectors and streamlines on this vertical plane are also shown in Fig. 7. The streamlines figures clearly show a two-bubble cell vortex breakdown. This is a typical three-dimensional vortex-breakdown mode which consists of an attracting saddle point (front) a repelling saddle point (rear), an attracting focus (top) and a repelling focus (bottom). Such a breakdown mode is similar to the one which was captured for an isolated supersonic vortex in an unbounded domain in Refs. 20 and 21. The location of the attracting saddle point is at 0.97 along the ray line, which corresponds to 0.87 along the axial direction. The attracting focus point is characterized with spiralling-in streamlines and the repelling focus point is characterized with spiralling-out streamlines. The Mach contours show that the front surface of the vortex-breakdown bubbles is enclosed by a hemi-spherical shape-like shock surface. Figures 12 and 13 show details of the flow structure on the wing plan view, on the plane of symmetry and on the ray plane at the 0.658 spanwise location (marked as J = 16 on Fig. 13). These figures and discussion give a complete construction of the flow structure including the shock system and its interaction with the leading-edge vortex core which produces vortex-breakdown of the two-bubble-cell mode.

Unsteadiness of the Vortex-Breakdown:

The computations have been carried out with time-accurate stepping beyond t = 3.6. Figures 8–11 show the results at t = 5.52. These results show that the terminating shock moves in the upstream direction and so is the

two-bubble-cell vortex breakdown behind the terminating shock. Figure 8 shows that the repelling focus is at x = 0.88 instead of x = 0.97 (Fig. 4). Figure 9 shows that the terminating shock in the plane of symmetry is at x = 0.685 instead of x = 0.83 (Fig. 5). The shock decreases in height and its thickness increases. Figure 10 shows that the size of the two-bubble cell vortex-breakdown region increases in comparison with the size at t = 3.6 (Fig. 7). Upstream of the terminating shock the flow stayed steady without any change.

Beyond the time t = 5.52, the upstream shock motion stopped and the motion reversed its direction to the downstream. The computations were not carried out beyond this instant due to its impeding cost. The unsteadiness of the terminating shock and the vortex-breakdown region behind it have also been observed experimentally by Bannik and Houtmann[23]. They also observed that the flow upstream of the terminating shock stayed steady without any change. These experimental observations undoubtedly support and validate our computational results.

CONCLUDING REMARKS

The laminar, unsteady, compressible, full Navier-Stokes equations are integrated time accurately using the implicit, upwind, flux-difference splitting, finite-volume scheme to study and construct the flow field structure of a transonic flow around a 65° sharp-edged, cropped-delta wing. A λ-shock system, which consists of a ray shock under the primary vortex core and a transverse terminating shock, has been captured. Behind the terminating shock, the leading-edge vortex core breaks down into a two-bubble cell type. The terminating shock and the vortex breakdown region behind it is time dependent and appears to be oscillatory. The flow field ahead of the terminating shock stays steady without any change. This is consistent with the fact that the supersonic pocket along with the terminating shock do not allow disturbances to propagate upstream. The present results have been validated using the available experimental data and they are in good agreement. The present paper gives a complete construction of the flow field over the wing surface and in particular the structure of the flow at the terminating shock and behind it.

ACKNOWLEDGEMENT

For the first two authors, this work is supported by the NASA-Langley Research Center under grant No. NAG-1-994 along with a partial support from the AFOSR. The Computational Resources provided by the NAS Center at Ames and the NASA Langley Research Center are acknowledged and appreciated.

REFERENCES

1. Lambourne, N. C. and Bryer, D. W., "Bursting of Leading-Edge Vortices: Some Observations and Discussion of the Phenomenon," Aeronautical Research Council, R&M 3282, 1961.

2. Sarpkaya, T., "Effect of The Adverse Pressure Gradient on Vortex Breakdown," AIAA Journal, Vol. 12, No. 12, Dec. 1974, pp. 602–607.

3. Escudier, M. P. and Zender, N., "Vortex Flow Regimes," Journal of Fluid Mechanics, Vol. 115, 1982, pp. 105–122.

4. Leibovich, S., "Vortex Stability and Breakdown: Survey and Extension," AIAA Journal, Vol. 22, No. 9, Sept. 1984, pp. 1192–1206.

5. Grabowski, W. J. and Berger, S. A., "Solutions of the Navier-Stokes Equations for Vortex Breakdown," Journal of Fluid Mechanics, Vol. 75, Part 3, 1976, pp. 525–544.

6. Hafez, M., Kuruvila, G. and Salas, M.D., "Numerical Study of Vortex Breakdown," Journal of Applied Numerical Mathematics, No. 2, 1987, pp. 292–302.

7. Salas, M. D. and Kuruvila, G., "Vortex Breakdown Simulation: A Circumspect Study of The Steady, Laminar, Axisymmetric Model," Computers and Fluids, Vol. 17, No. 1, 1989, pp. 247–262.

8. Wu, J. C. and Hwang, S., "Computational Study of Vortex Breakdown in Circular Tube," AIAA 91–1820, June 1991.

9. Menne, S. and Liul, C. Hl., "Numerical Simulation of a Three-Dimensional Vortex Breakdown," Z. Flugwiss. Weltraumforsch 14, 1990, pp. 301–308.

10. Spall, R. E., Gatski, T. B. and Ash, R. L., "The Structure and Dynamics of Bubble-Type Vortex Breakdown," Proc. R. Soc., London, A429, 1990, pp. 613–637.

11. Breuer, M. and Hänel, D., "Solution of The 3-D Incompressible Navier-Stokes Equations for the Simulation of Vortex Breakdown," Eight GAMM Conference, Delft, Netherlands, September 27–29, 1989.

12. Krause, E., "Vortex Breakdown: Physical Issues and Computational Simulation," Third International Congress of Fluid Mechanics, Cairo, Egypt, January 1990, Vol. 1, pp. 335–344.

13. Delery, J., Horowitz, E., Leuchter, O. and Solignac, J. L., "Fundamental Studies of Vortex Flows," La Recherche Aerospatiale, No. 1984–2, 1984, pp. 1–24.

14. Metwally, O., Settles, G. and Horstman, C., "An Experimental Study of Shock Wave/Vortex Interaction," AIAA 89–0082, January 1989.

15. Cutler, A. D. and Levey, B. S., "Vortex Breakdown in a Supersonic Jet," AIAA 91–1815, June 1991.

16. Rhode, D. L., Lilley, D. B. and McLaughlin, D. K., "On The Prediction of Swirling Flowfields Found in Axisymmetric Combustor Geometries," Transactions of ASME, Vol. 104, September 1982, pp. 378–384.

17. Kandil, O. A., Kandil, H. A. and Liu, C. H., "Computation of Steady and Unsteady Compressible Quasi-Axisymmetric Vortex Flow and Breakdown," AIAA 91–0752, January 1991.

18. Kandil, O. A., Kandil, H. A. and Liu, C. H., "Supersonic Quasi-Axisymmetric Vortex Breakdown," AIAA 91–3311–CP, September 1991, pp. 851–863.

19. Kandil, O. A., Kandil, H. A. and Liu, C. H., "Critical Effects of Downstream Boundary Conditions on Vortex Breakdown," AIAA 92–2601 CP, June 22-24, 1992, pp. 12–25.

20. Kandil, O. A., Kandil, H. A. and Liu, C. H., "Three-Dimensional Supersonic Vortex Breakdown," AIAA 93–0526, January 11–14, 1993.

21. Kandil, H. A., "Navier-Stokes Simulation of Quasi-Axisymmetric and Three-Dimenisonal Supersonic Vortex-Breakdown," Ph.D. Dissertation, Dept. of Mechanical Engineering and Mechanics, Old Dominion University, Norfolk, VA, May 1993.

22. Boersen, S. J. and Elsenaar, A., "Tests on the AFWAL 65° Delta Wing at NLR: A Study of Vortex Flow Development Between Mach = 0.4 and 4," Proceedings of Symposium on International Vortex Flow Experiment on Euler Code Validation, Stockholm, Sweden, October 1–3, 1986, pp. 23–36.

23. Bannik, W. J. and Houtman, E. M., "Experiments on the Transonic Flow Over a Delta Wing at High Angles of Attack," Proceedings of Symposium on International Vortex Flow Experiment on Euler Code Validation, Stockholm, Sweden, October 1–3, 1986, pp. 37–46.

24. Hartmann, K., "Force and Pressure Measurements Including Surface Flow Visualization on a Cropped Delta Wing," Proceedings of Symposium on International Vortex Flow Experiment on Euler Code Validation, Stockholm, Sweden, October 1–3, 1986, pp. 63–87.

25. Bütefisch, K. A., Pallek, D. and Sauerland, K., -H., "International Vortex Flow Experiment-Results of Three Component LDA Measurements on a 65° Delta Wing," DFVLR IB 222–87 A 34, 1987.

26. Elsenaar, A., Hjelmberg, L., Bütefisch, K. and Bannink, W. J., "The International Vortex Flow Experiment," AGARD-CP-437, Lison, Portugal, May 1988, Vol. 1., pp. 9.1–9.23.

27. Hitzel, S. M., "Wing Vortex-Flows Up into Vortex-Breakdown-A Numerical Simulation," AIAA 88-2518-CP, 1988, pp. 73–83.

28. Bannink, W. J. and Houtman, E. M., "Experimental and Computational Study of the Vortical Flow Over a Delta wing at High Angles of Attack," IUTAM Symposium on Fluid Dynamics of High Angle of Attack, University of Japan, Tokyo, Japan, September 14–17, 1992.

29. Laine, S., Siikonen, T. and Kaurinkoski, P-, "Calculation of Transonic Viscous Flow Around a Delta Wing," ICAS 92–4.2.1, Beijing, PRC, September 22-25, 1992, pp. 286–295.

30. Erickson, G. E., "Wind Tunnel Investigation of The Interaction and Breakdown Characteristics of Slender-Wing Vortices at Subsonic, Transonic and Supersonic Speeds," NASA Tech. paper 3114, November 1991.

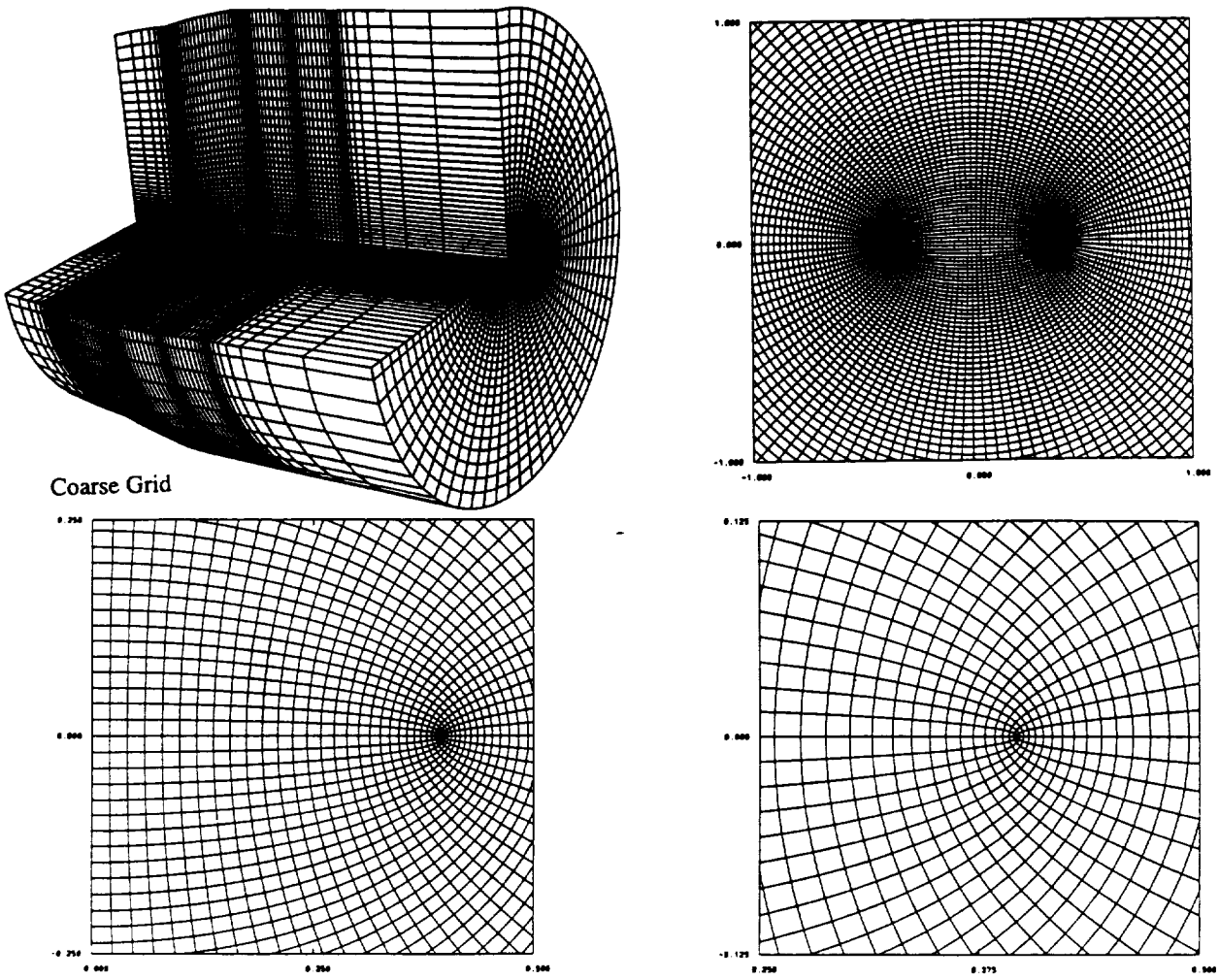

Fig. 1. Coarse grid; three-dimensional shape and cross-flow plane and its blow-up, 125×85×84

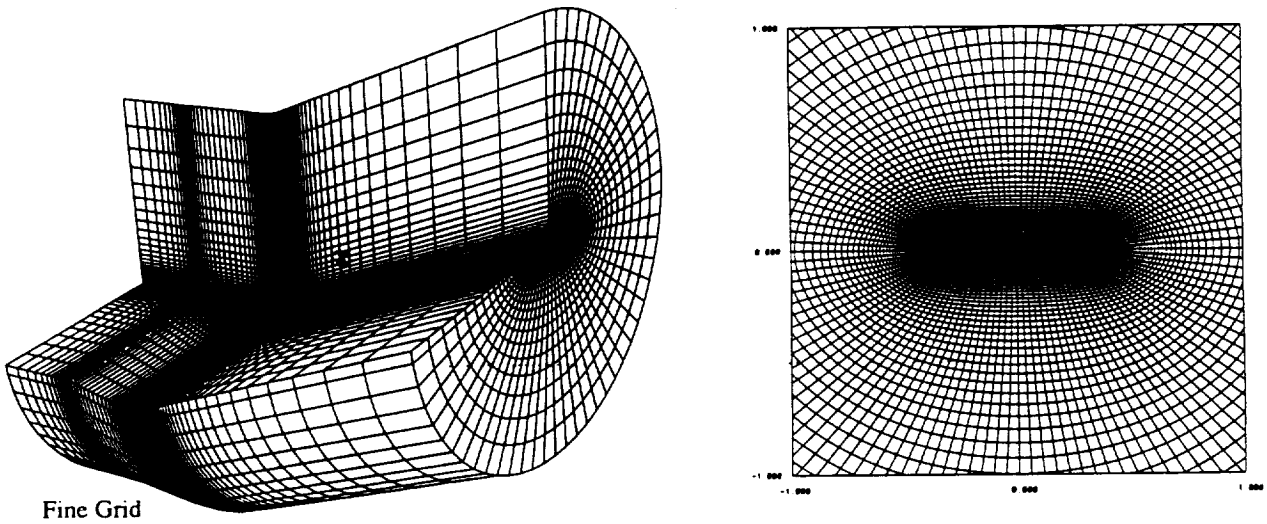

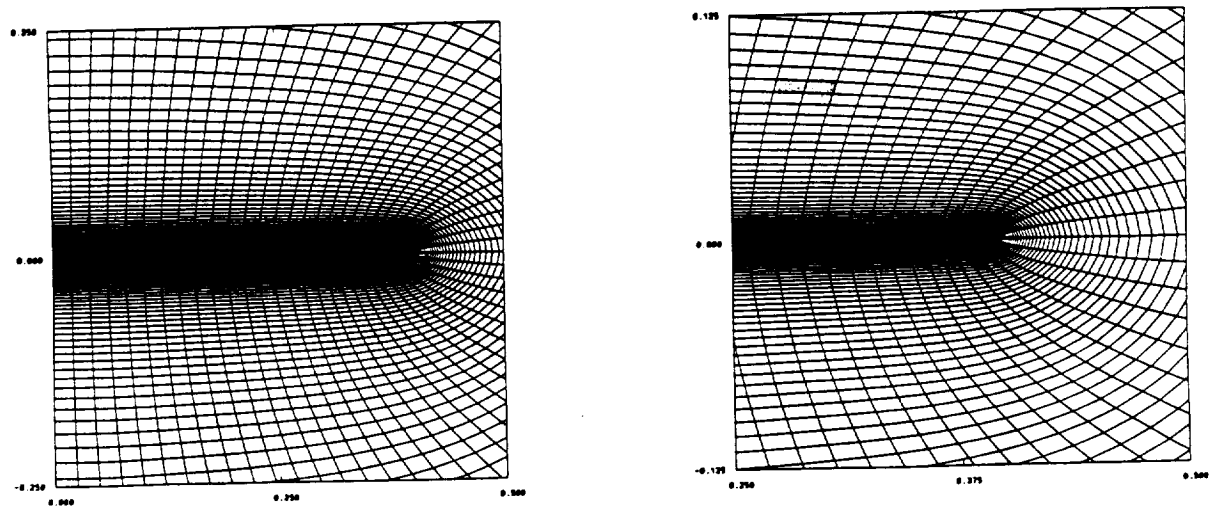

Fig. 2. Fine grid; three-dimensional shape and a cross-flow plane and its blow-up, 128×85×84

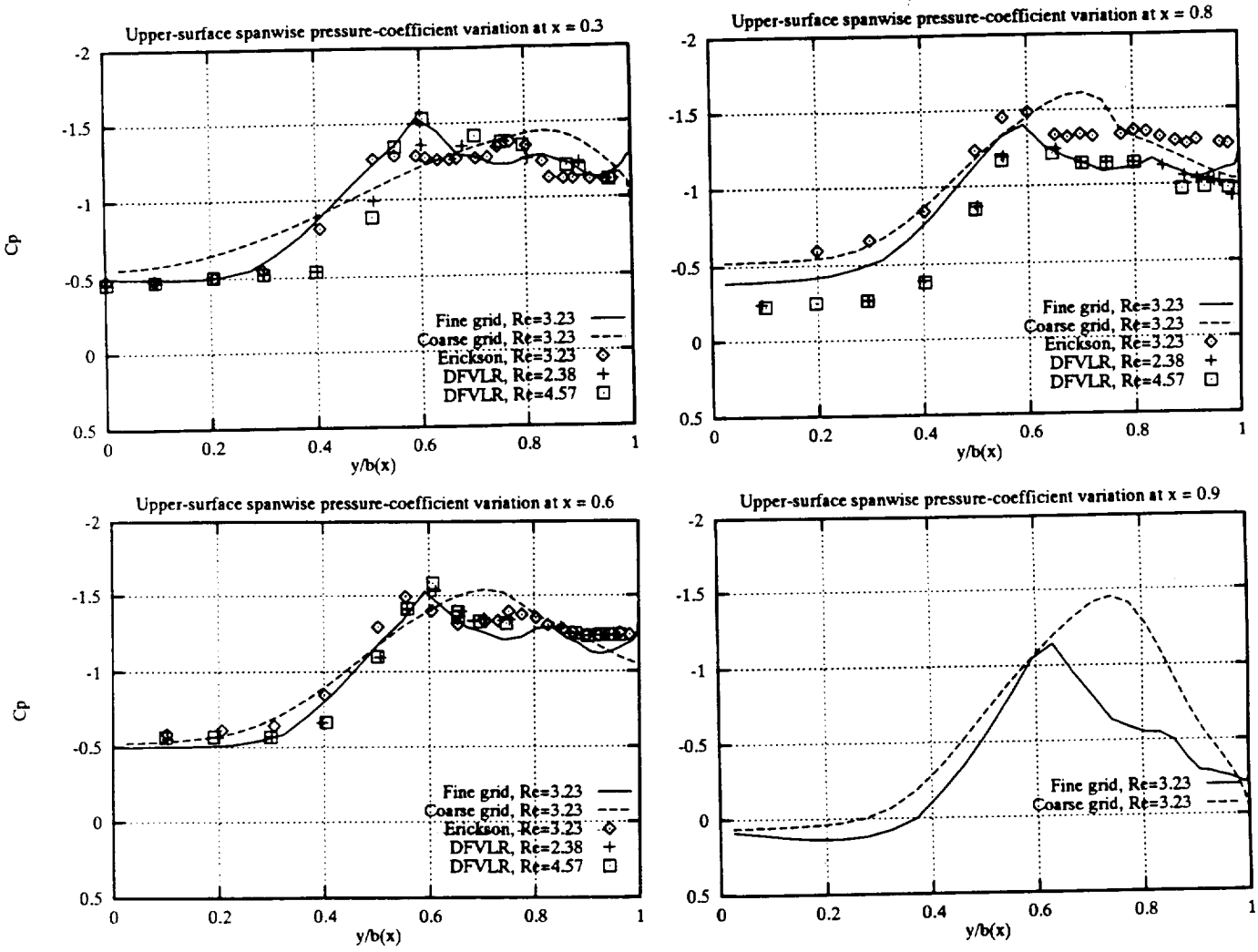

Fig. 3. Comparison of the computed and experimental spanwise, surface-pressure coefficient at different chord stations; $M_\infty = 0.85$, $\alpha = 20°$, $t = 3.6$

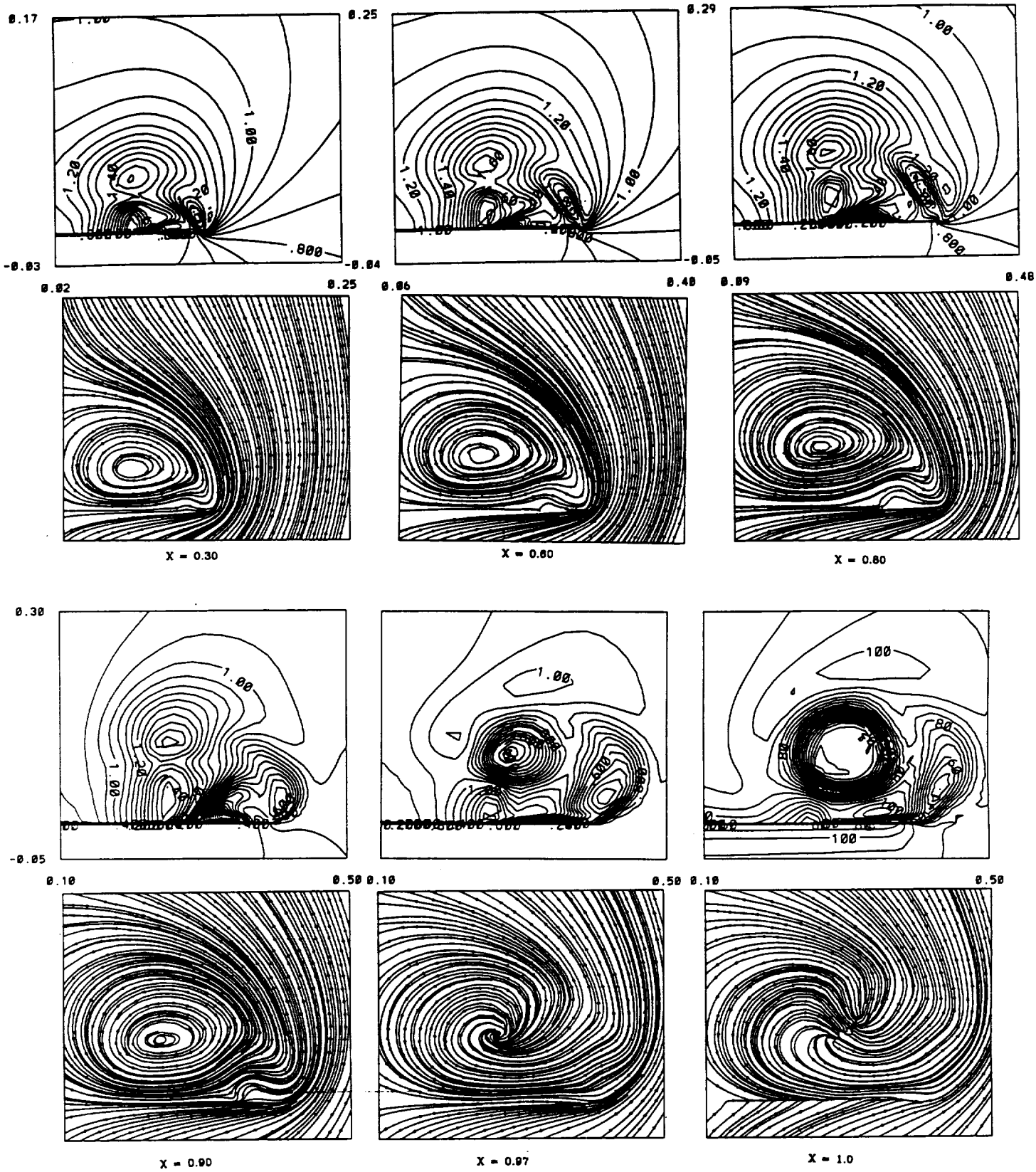

Fig. 4. Total-Mach contours and streamlines in cross-flow planes; $M_\infty = 0.85$, $\alpha = 20°$, $t = 3.6$

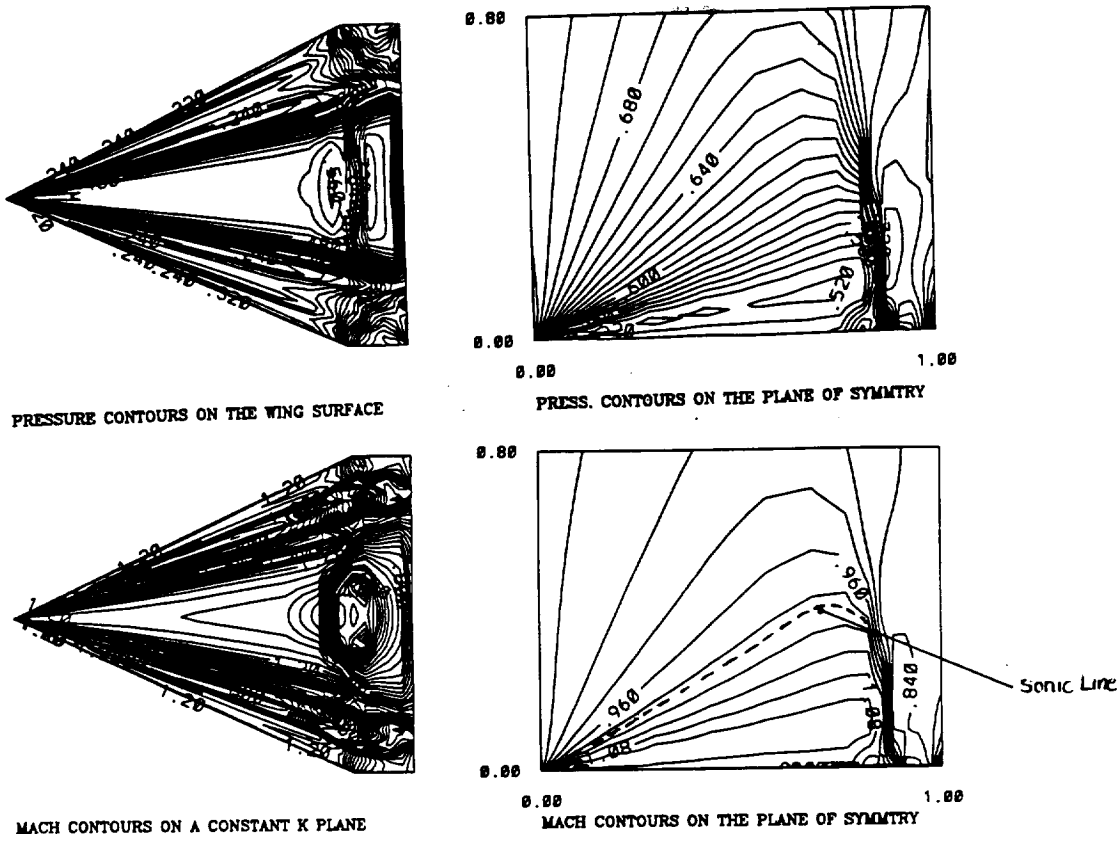

Fig. 5. Static-pressure and Mach contours on the wing and the plane of symmetry; $M_\infty = 0.85,\ \alpha = 20°,\ t = 3.6$

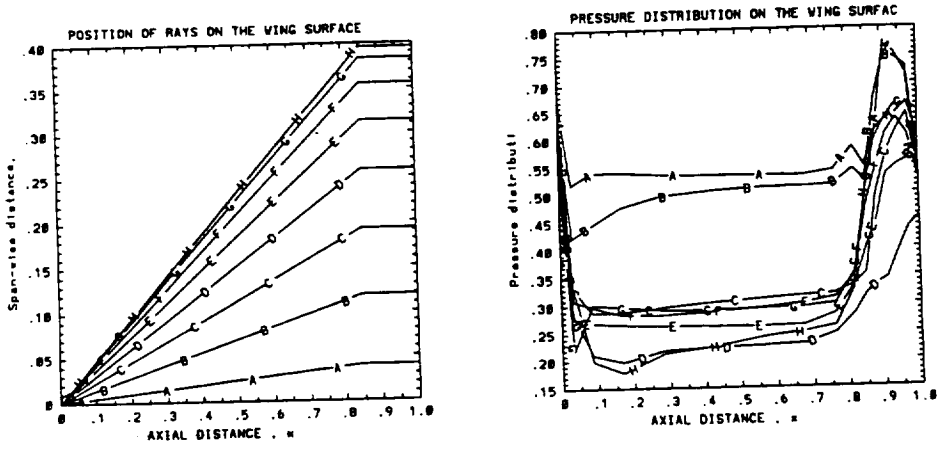

Fig. 6. Ray lines on the wing surface and the static-pressure variation along them; $M_\infty = 0.85,\ \alpha = 20°,\ t = 3.6$

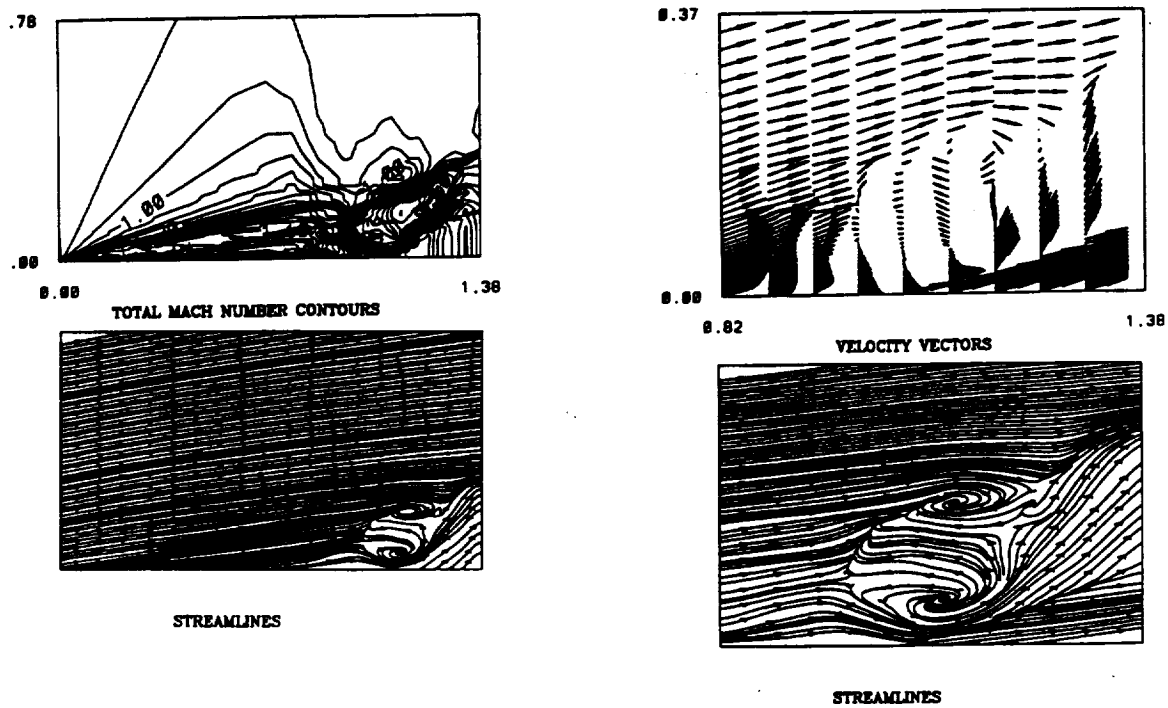

Fig. 7. Total-Mach contours, streamlines and velocity vectors on a ray plane passing through the vortex-breakdown two-bubble cell; $M_\infty = 0.85$, $\alpha = 20^\circ$, $t = 3.6$

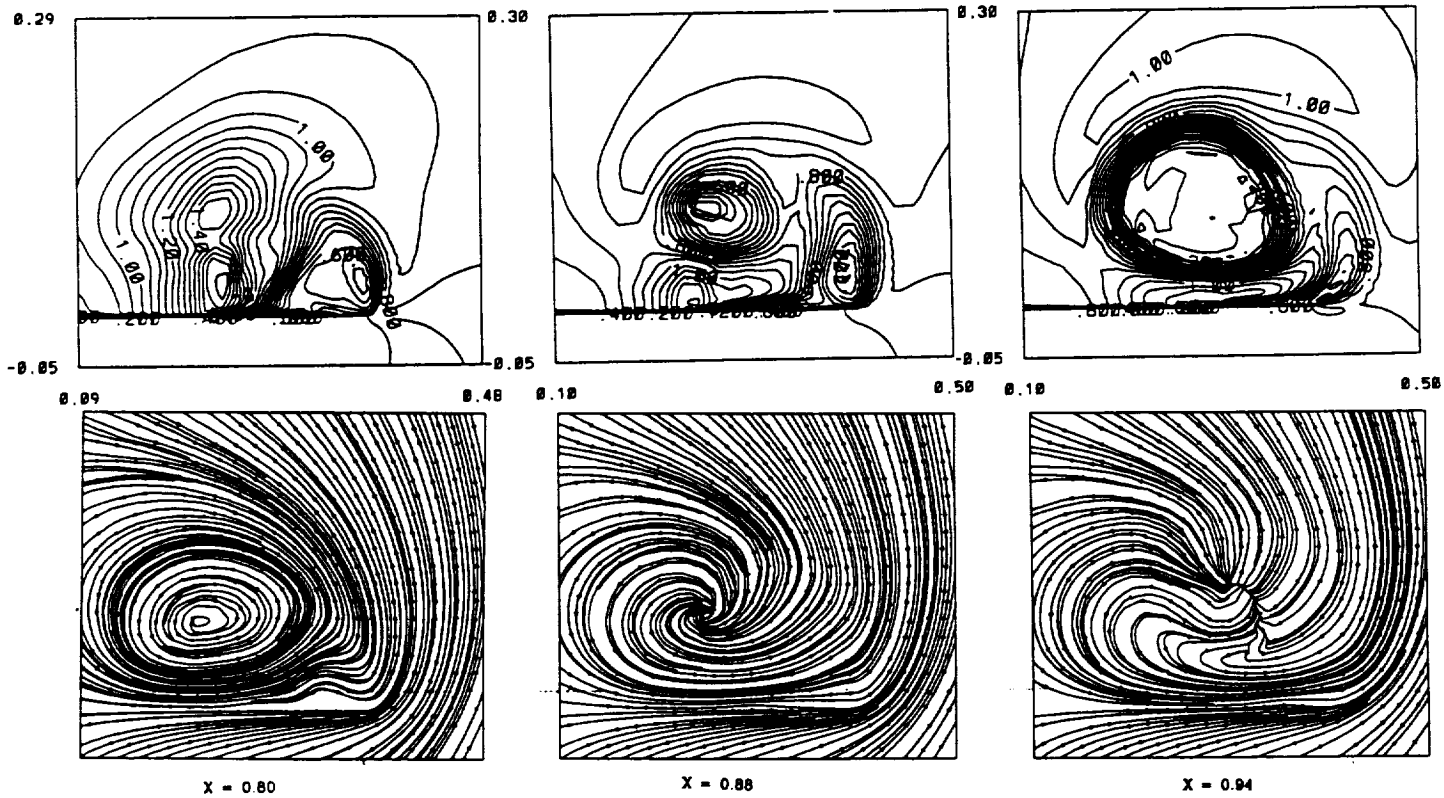

Fig. 8. Total-Mach contours and streamlines in cross-flow plane; $M_\infty = 0.85$, $\alpha = 20^\circ$, $t = 5.52$

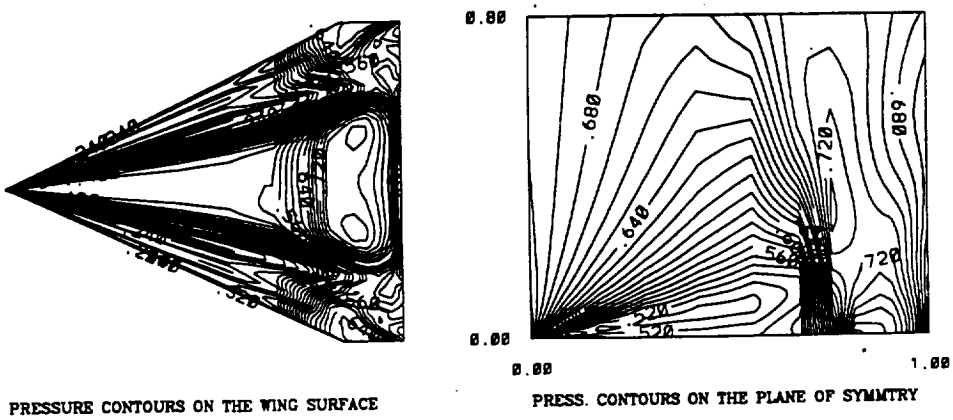

Fig. 9. Static-pressure contours on the wing and the plane of symmetry; $M_\infty = 0.85,\ \alpha = 20°,\ t = 5.52$

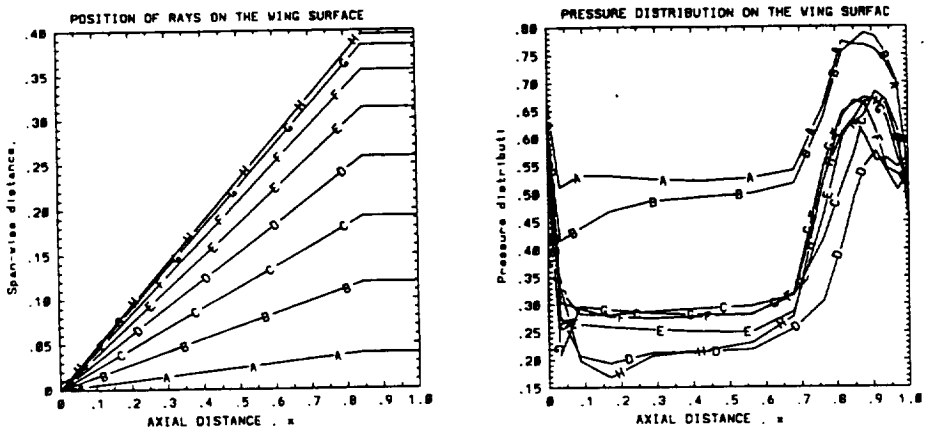

Fig. 10. Ray lines on the wing surface and the static-pressure variation along them; $M_\infty = 0.85,\ \alpha = 20°,\ t = 5.52$

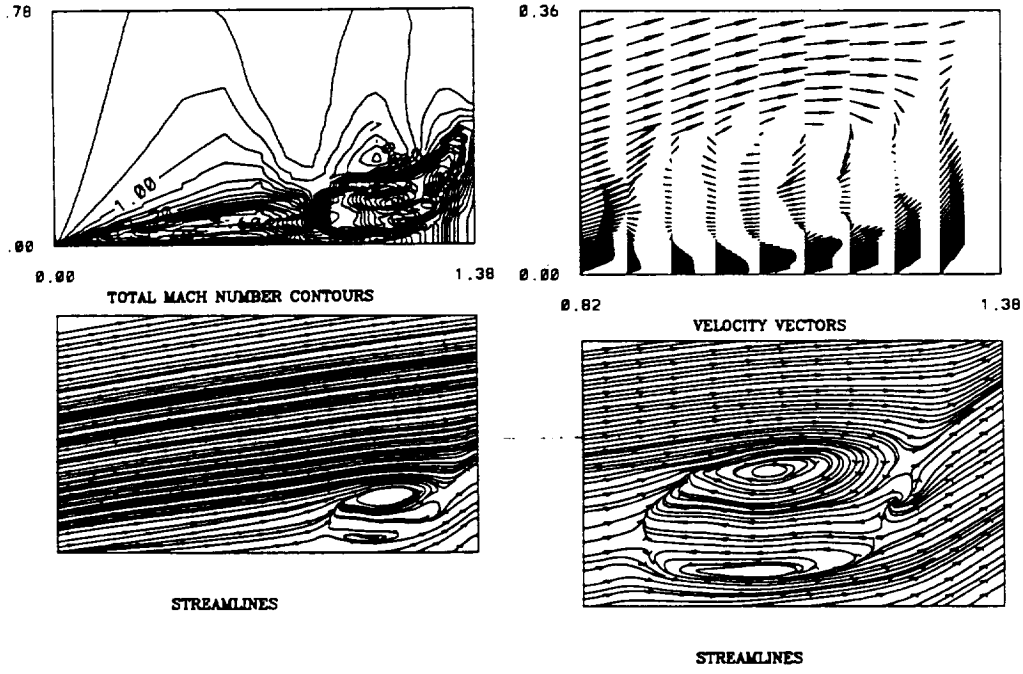

Fig. 11. Total-Mach contours, streamlines and velocity vectors on a ray plane passing through the vortex-breakdown bubbles; $M_\infty = 0.85,\ \alpha = 20°,\ t = 5.52$

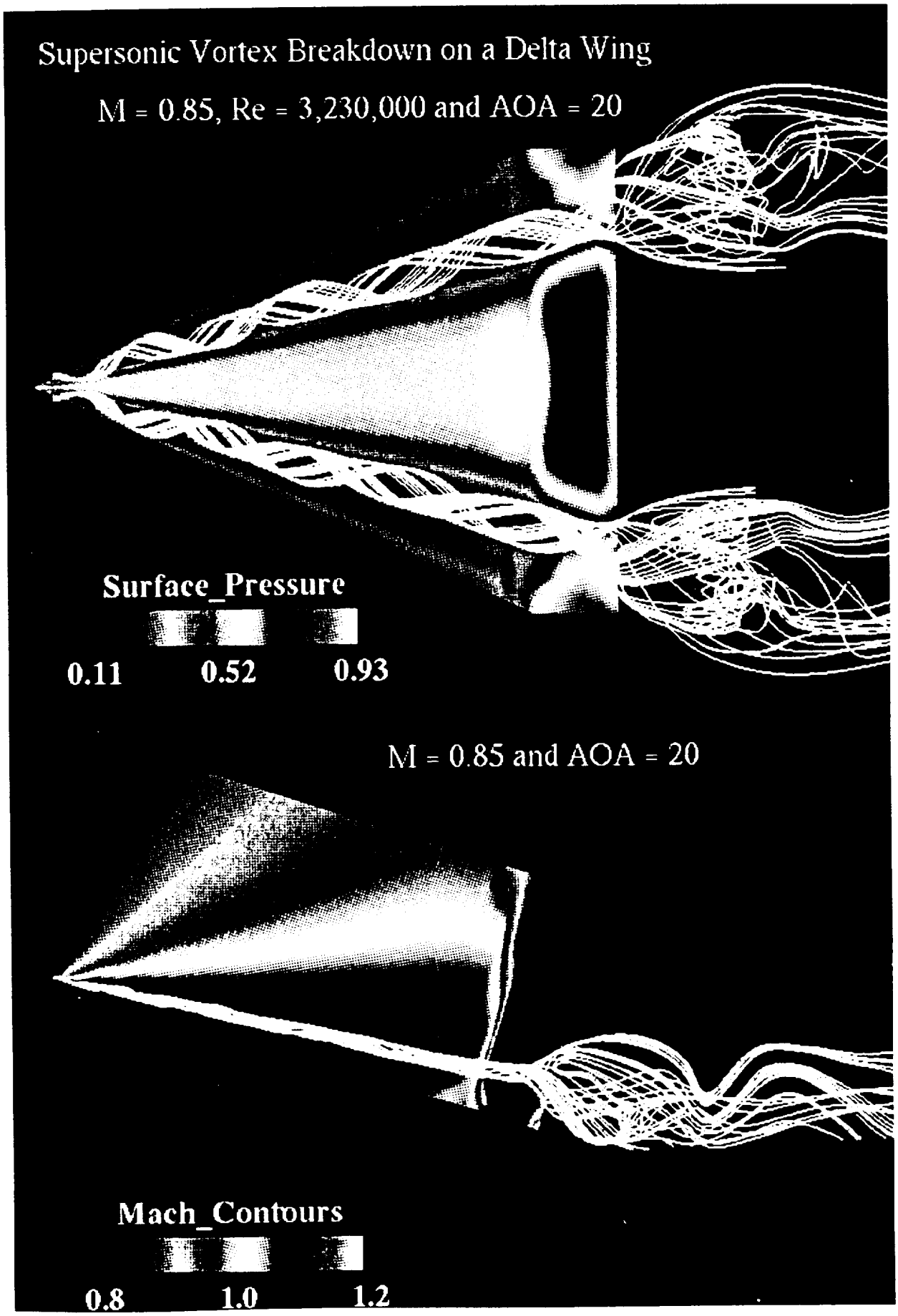

Fig. 12 Surface-pressure and Mach contours and particle trance on wing and symmetry planes; M_∞ = 0.85, α = 20°, t = 3.6

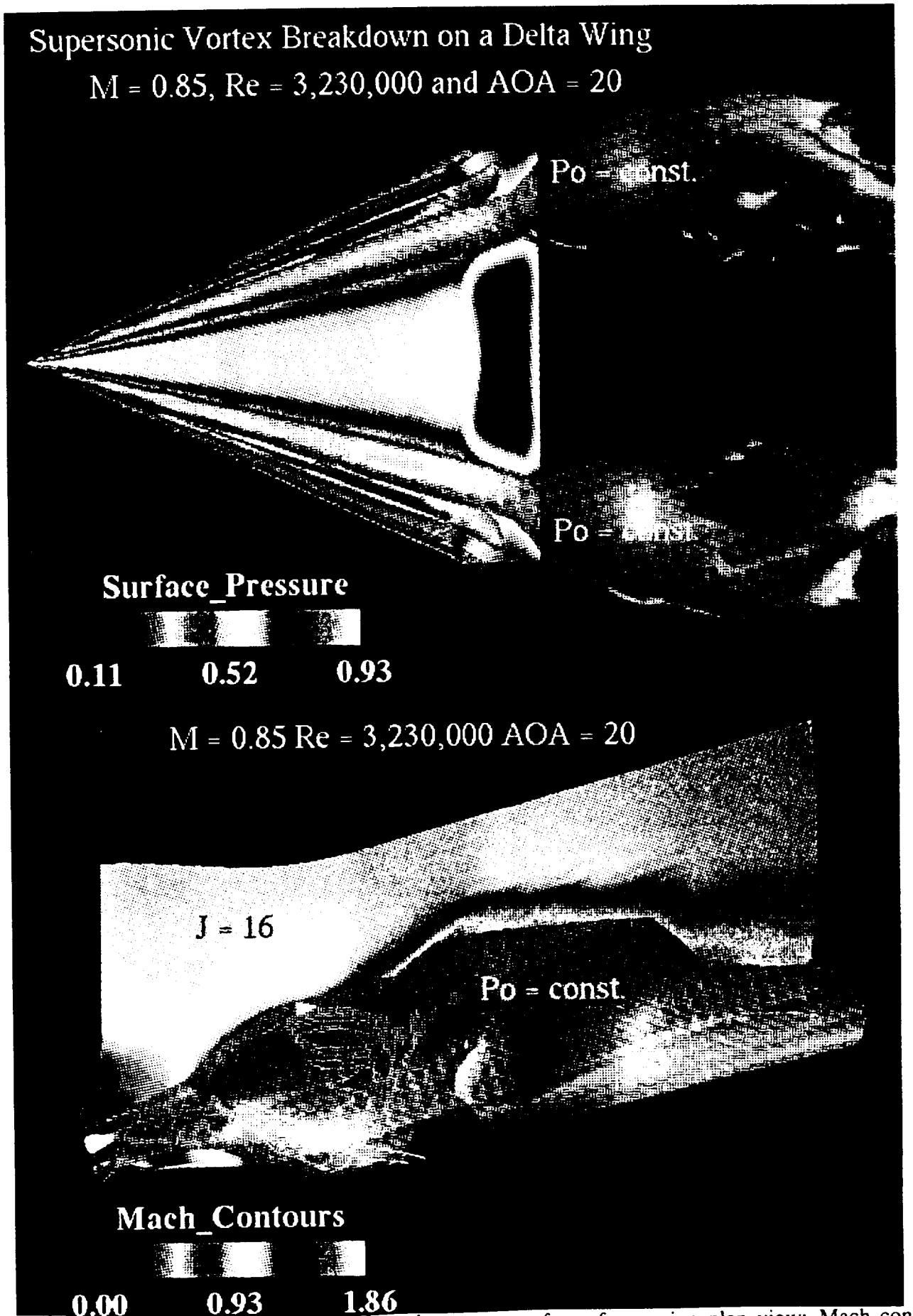

Fig. 13. Surface-pressure contours and total-pressure surfaces for a wing plan view; Mach contours and total-pressure surface on a ray plane passing through the vortex-breakdown bubble; $M_\infty = 0.85$, $\alpha = 20°$, $t = 3.6$

AIAA-93-3472-CP

SUPERSONIC VORTEX BREAKDOWN OVER A DELTA WING IN TRANSONIC FLOW

Hamdy A. Kandil and Osama A. Kandil
Old Dominion University, Norfolk, VA 23529

C. H. Liu
NASA Langley Research Center, Hampton, VA 23681

AIAA 11th Applied
Aerodynamics Conference
August 11–13, 1993/Monterey, CA

SUPERSONIC VORTEX BREAKDOWN OVER A DELTA WING IN TRANSONIC FLOW

Hamdy A. Kandil* and Osama A. Kandil**
Old Dominion University, Norfolk, VA 23529
and
C. H. Liu***
NASA Langley Research Center, Hampton, VA 23681

ABSTRACT

The effects of freestream Mach number and angle of attack on the leading-edge vortex breakdown due to the terminating shock on a 65–degree, sharp-edged, cropped delta wing are investigated computationally. The computational investigation uses the time-accurate solution of the laminar, unsteady, compressible, full Navier-Stokes equations with the implicit, upwind, flux-difference splitting, finite-volume scheme. A fine O-H grid consisting of $125\times85\times84$ points in the wrap-around, normal and axial directions, respectively, is used for all the flow cases. Keeping the Reynolds number fixed at 3.23×10^6, the Mach number is varied from 0.85 to 0.9 and the angle of attack is varied from 20° to 24°. The results show that at 20° angle of attack, the increase of the Mach number from 0.85 to 0.9 results in moving the location of the terminating shock downstream. The results also show that at 0.85 Mach number, the increase of the angle of attack from 20° to 24° results in moving the location of the terminating shock upstream. The results are in good agreement with the experimental data.

INTRODUCTION

The literature shows that vortical flows around delta wings in the low-speed regime have received a substantial volume of experimental[1–4] and computational[5–9] research work. In the high angle of attack range, vortical flows in the low-speed regime are characterized with three types of boundary-layer separation, namely; primary, secondary and tertiary separations. The primary separated flow rolls up into a strong primary vortex core which produces a strong suction-pressure peak on the wing surface. The spanwise adverse-pressure gradient of the primary vortex causes the spanwise, outboard-moving, boundary-layer flow to separate forming a secondary vortex with opposite sense of rotation to and smaller strength than that of the primary vortex. The spanwise adverse-pressure gradient of the secondary vortex causes the spanwise, inboard-moving, boundary-layer flow to separate forming a tertiary vortex with same sense of rotation as and substantially small strength than that of the primary vortex. The spanwise surface-pressure curves are characterized with three suction-pressure peaks which varies in strength corresponding to the locations of the primary, secondary and tertiary vortices. When the angle of attack reaches a critical value, the axial-pressure gradient and the high swirl ratio of the primary vortex produce a stagnation point along the path line of the primary-vortex core, and vortex breakdown of the primary core develops. Depending on the swirl ratio, axial pressure gradient and Reynolds number, the primary-core vortex-breakdown mode might be a bubble type, a spiral type or a bubble-spiral type.

As the freestream Mach number increases, the vortical flow around the delta wing changes substantially due to the compressibility effects. In the supersonic flow regime, shock waves appear beneath or above the primary vortex, depending on the freestream normal Mach number and normal angle of attack. Experimental data[10, 11] and the computational results[12–14] have shown these types of vortical-flow structures. The foot print of these shock waves runs along a ray line from the wing vertex. If the shock wave is beneath the primary vortex, it interacts with the spanwise, outboard-moving, boundary-layer flow and causes, in addition to the adverse pressure gradient produced by the primary vortex, secondary-flow separation. If the shock wave is above the primary vortex, it flattens the primary vortex and the spanwise surface pressure curve. Comparison of the surface pressure distribution over a delta wing in low-speed and supersonic-speed regimes, shows that the suction-pressure peak corresponding to the primary vortex is lower for the supersonic flow than that for the low-speed flow.

In the transonic-flow regime, research work on vortical flows around delta wings was given adequate attention only recently. Understanding the steady and unsteady, transonic, vortical-flow structures around delta wings in the moderate-high angle of attack range is important for increasing the performance quality of the new generation of supermaneuver aircraft (e.g. YF22). Recent experimental measurements of transonic flows around a 65° cropped delta wing[15–21] show that a complex shock-wave system appears over the upper wing surface. The shock-wave system consists of a ray shock wave beneath the leading-edge primary vortex and a transverse, time-dependent[16], normal-shock wave (known as a terminating shock) which runs from the plane of symmetry to the wing leading edge. The terminating shock wave interacts

* Research Associate, Dept. of Aerospace Engineering, Member AIAA.
** Professor, Eminent Scholar and Chairman of Dept. of Aerospace Engineering, Associate Fellow AIAA.
*** Senior Research Scientist, Computational Aerodynamic Branch, Associate Fellow AIAA.

with the primary-vortex core causing it to breakdown at an angle of attack as low as 18°. Such a critical angle of attack is substantially smaller than the critical angle of attack of vortex breakdown in the low-speed regime. Reference 21 contains extensive flow measurements for the 65° cropped delta wing with and without leading-edge extension (LEX). A complete reconstruction of the three-dimensional flow field at and behind the terminating shock was not possible experimentally.

Computational simulations for transonic delta-wing flows have been developed on a very limited scale by using the Euler equations[20, 22] and the thin-layer Navier-Stokes equations[23]. The Euler-equations solutions were not capable of fully resolving the flow in the terminating shock region and the thin-layer Navier-Stokes-equations solutions did not address that region. In Ref. 24 by the present authors, the laminar, unsteady, compressible, full Navier-Stokes equations are integrated time accurately using the implicit, upwind, flux-difference splitting, finite-volume scheme to study and construct the flow field structure of a transonic flow around a 65° sharp-edged, cropped-delta wing at 20° angle to attack, 0.85 Mach number and 3.23×10^6 Reynolds number. A fine O-H grid consisting of $125\times85\times84$ points in the wrap-around, normal and axial directions, respectively, is used for the computational solution. A λ-shock system, which consists of a ray shock under the primary vortex core and a transverse terminating shock, has been captured. Behind the terminating shock, the leading-edge vortex core breaks down into a two-bubble cell type. The terminating shock and the vortex breakdown region behind it are time dependent and appear to be oscillatory. The flow field ahead of the terminating shock is steady and includes a supersonic pocket which is surrounded by the ray shock and the terminating shock. The flow inside the pocket does not change due to changes in the flow downstream. This is consistent with the fact that the supersonic pocket along with the terminating shock do not allow disturbances to propagate upstream. These results have been validated using the available experimental data and they are in good agreement. This work gives a complete construction of the flow field over the wing surface and in particular the structure of the flow at the terminating shock and behind it.

In this paper, a parametric study is carried out to investigate the effects of freestream Mach number and angle of attack on the terminating shock and the leading-edge, primary-vortex breakdown for the same 65° sharp-edged, cropped delta wing. The computational investigation uses the same equations, computational scheme and grid of Ref. 24. Keeping the Reynolds number fixed at 3.23×10^6, the Mach number is changed from 0.85 to 0.9 while the angle of attack is fixed at 20°, and the angle of attack is changed from 20° to 24° while the Mach number is fixed at 0.85.

HIGHLIGHTS OF FORMULATION AND COMPUTATIONAL SCHEME

The conservative form of the dimensionless, unsteady, compressible, full Navier-Stokes equations is used for the formulation of the problem. The equations are written in terms of the time-independent, body-conformed coordinates ξ^1, ξ^2 and ξ^3 (Ref. 25).

The implicit, upwind, flux-difference splitting, finite-volume scheme is used to solve the unsteady, compressible, full Navier-Stokes equations. The scheme uses the flux-difference splitting scheme of Roe which is based on the solution of the approximate one-dimensional, Riemann problem. In the Roe scheme, the inviscid flux difference at the interface of computational cells is split into two parts; left and right flux differences. The splitting is accomplished according to the signs of the eigenvalues of the Roe averaged-Jacobian matrix of the inviscid fluxes at the cell interface. The smooth flux limiter is used to eliminate oscillations at locations of large flow gradients. The viscous- and heat-flux terms are linearized in time and the cross-derivative terms are neglected in the implicit operator and retained in the explicit terms. The viscous terms are differenced using a second-order accurate central differencing. The resulting difference equation is approximately factored and is solved in three sweeps in the ξ^1, ξ^2 and ξ^3 directions. The computational scheme is coded in the computer program "FTNS3D" which is a modified version of the CFL3D-code.

COMPUTATIONAL RESULTS

A 65° swept-back, sharp-edged, cropped delta wing of zero thickness is considered for the computational solutions. The cropping ratio (tip length/root-chord length) is 0.15. An O-H grid of $125\times85\times84$ in the wrap-around, normal and axial directions, respectively, is used. The computational domain extends two-chord length forward and five-chord length backward from the wing trailing edge. The radius of the computational domain is four-chord length. The minimum grid size normal to the wing surface is 5×10^{-4} from the leading edge to the plane of symmetry. Figure 1 shows a three-dimensional shape of the grid and a cross-flow plane.

Time-accurate integration of the laminar, unsteady, compressible, full Navier-Stokes equations has been carried out with $\Delta t = 0.0002$. Three flow conditions are used to study the effect of increasing the Mach number while the angle of attack is kept constant and the effect of increasing the angle of attack while the Mach number is kept constant. In all the three cases, the Reynolds number, R_e, is 3.23×10^6 based on the root-chord length.

Case I ($M_\infty = 0.85$, $\alpha = 20°$)

For this case, the freestream Mach number, M_∞, and angle of attack, α, are 0.85 and 20°, respectively. Figure 2 shows a comparison of the computed, spanwise, surface-pressure coefficient (C_p) at different chord stations (x =

0.3, 0.6 and 0.8) with the experimental data of Erickson[21] ($R_e = 3.23\times10^6$) and Hartmann[17] ($R_e = 2.38\times10^6$ and 4.57×10^6). The computational results show the correct location and level of the suction-pressure peak corresponding to the primary vortex in comparison with the experimental data. They also show a smaller suction-pressure peak corresponding to the secondary vortex. The computational results are in fair to good agreement with the experimental data. For the chord station x = 0.9, the C_p-curve shows a rapid increase in the pressure coefficient (a decrease in the suction-pressure coefficient). For example, the suction-pressure-peak coefficient increases from a value of –1.4 at x = 0.8 to a value of –1.15 at x = 0.9. Figure 3 shows the total-Mach contours and streamlines at the chord stations of x = 0.60, 0.90 and 0.97. At x = 0.60, the Mach contours show an oblique shock beneath the primary vortex and a subsonic, separated region to its right. The streamlines show a secondary separated flow and the corresponding secondary vortex. This separation is due to the shock interaction with the surface boundary-layer flow and is also due to the adverse, spanwise pressure gradient created by the primary vortex. At x = 0.90, the shock beneath the primary vortex becomes weak and the primary-vortex size increases. At x = 0.97, the shock beneath the primary vortex disappears and the primary vortex diffuses and reduces to a repelling focus, as shown by the streamlines. The details of the flow structure at x = 0.90 and 0.97 in addition to the spanwise, pressure-distribution curve at x = 0.90 clearly indicate that the primary vortex is experiencing a vortex breakdown due to a transverse shock (terminating shock) which is located between x = 0.80 and x = 0.90.

Figure 4 shows the static pressure contours on the wing and symmetry planes. The contours clearly show the location, shape and strength of the terminating shock. A substantial supersonic pocket which is bounded by the terminating shock and the ray shocks (shocks beneath the primary-vortex cores) is observed on the wing plane. The terminating shock is located at x = 0.83 at the plane of symmetry, which is in good agreement with the experimental data[21], where the shock is located at x = 0.84 at the plane of symmetry. Figure 5 shows the position of ray lines from the wing vertex (which are marked by the letters A-H) and the static-pressure variation along these lines. The static-pressure curves give several points to generate the foot-print line of the terminating shock. The terminating shock is found to extend from the plane of symmetry to the wing leading edge. It reaches its highest strength at the location of the primary vortex (lines E-G). Figure 6 shows the total-Mach contours and streamlines on a vertical ray plane at the 0.68 spanwise location which passes through the vortex breakdown. Blow-ups of the velocity vectors and streamlines on this ray plane are also shown in Fig. 6. The streamlines conclusively show a two-bubble cell vortex breakdown. It is a typical three-dimensional vortex breakdown mode which consists of an attracting saddle point (front), a repelling saddle point (rear), an attracting focus (top), and a repelling focus (bottom). Such a breakdown mode is similar to the one which was captured for an isolated supersonic vortex in an unbounded domain in Refs. 26 and 27. The location of the attracting saddle point is at 0.97 along the ray line which corresponds to a location of 0.87 along the axial direction. The Mach contours show that the front surface of the vortex-breakdown bubbles is enclosed by a hemispherical shape-like shock surface. In Fig. 18, the details of the flow structure on the wing and symmetry planes are shown.

Having established the flow structure of this case, the Mach number is increased to 0.9 while the angle of attack is kept fixed at 20°.

Case II ($M_\infty = 0.90$, $\alpha = 20°$)

The results of this case are given in Figs. 7–11 and 19. Figure 7 shows the computational spanwise, surface-pressure coefficient at different chord stations along with the experimental data of Erickson[21]. The computational results are in good agreement with the experimental data at x = 0.3 and 0.6. At x = 0.8, the computational results underestimates the pressure coefficient of the experimental data. The locations of the primary and secondary vortex cores are in good agreement with those of the experimental data. It is noticed that the levels of C_p for the present case are lower than those of Case I (Fig. 2). Again, the pressure level decreases rapidly at x = 0.90. Figure 8 shows the total-Mach contours and streamlines in cross-flow planes at x = 0.60, 0.90 and 0.97. The shock beneath the primary vortex is observed in the Figures at x = 0.60 and x = 0.90. For x = 0.90, the shock beneath the primary vortex is still strong in comparison with that of Case I (Fig. 3). At x = 0.97, the repelling focus is observed indicating that vortex breakdown has occurred. Figure 9 shows that the terminating shock in the cross-flow plane is located at x = 0.93 within the boundary-layer, which is in good comparison with the experimentally measured shock of Ref. 21, where it is located at x = 0.95. The static-pressure contours on the wing plane show that the terminating shock for Case II (Fig. 9) is closer to the trailing edge that of Case I (Fig. 4). It should be noted here that the terminating-shock location in the outer flow is ahead of its location in the boundary-layer flow. The static-pressure variations along the ray lines of Fig. 10 clearly show that the terminating-shock foot print is located between x = 0.925 and x = 0.95, and that it extends from the plane of symmetry to the wing leading edge. Figure 11 shows the Mach contours and streamlines on a vertical ray plane passing through the vortex breakdown. It is noticed that the vortex breakdown shape is different from and smaller than that of Case I (Fig. 6). The attracting saddle point, attracting focus and repelling saddle point are clearly observed. The repelling focus is very small. This indicates that the terminating shock becomes smaller in strength than that of Case I. Figure 19 shows the details of this flow case on the wing and symmetry planes.

It is concluded that as the freestream Mach number increases slightly from 0.85 to 0.9, the terminating shock strength decreases and its location moves downstream from x = 0.84 to x = 0.93. Moreover, the surface pressure levels become smaller than those of Case I.

Next, the Mach number is kept fixed at 0.85 and the angle of attack is increased to 24°.

Case III (M_∞ = 0.85, α = 24°)

The results of this case are given in Figs. 12–17 and 20. The computational surface-pressure result at x = 0.3 (Fig. 12) is in good agreement with the experimental data of Erickson[21]. However, the computational results, at x = 0.6 and 0.8 are either overpredicting or underpredicting the experimental data. Figures 13, 14 and 15 show that the terminating shock moves upstream to x = 0.753 in the boundary-layer flow at the plane of symmetry. This is in good agreement with the experimental data of Ref. 21, where the shock is located at x = 0.75 in the boundary layer flow. The terminating-shock location in the outer flow is ahead of its location in the boundary layer. Figure 16 shows that the vortex-breakdown region is larger than those of Cases I and II. Moreover, the attracting and repelling foci are smaller than those of Case I. Figure 20 shows the details of this case on the wing and symmetry planes.

Thus, it is seen that as the angle of attack increases from 20° to 24° while the Mach number is kept fixed at 0.85, the terminating shock moves upstream and the vortex-breakdown region becomes large. Moreover, the surface pressure levels become larger than those of Case I.

The computational results show that the flow at the terminating shock and behind it is time dependent and it indicates oscillatory motion (The computations have not been carried out beyond t = 6.0 or 30,000 time steps with Δt = 0.0002). In Fig. 17, we show snapshots of the streamlines and their blow-ups on a ray plane passing through the vortex-breakdown region. The snapshots are shown at t = 4.22, 5.16 and 5.52. It is clearly seen that the vortex breakdown moves upstream showing different modes. In the same time, the terminating shock is also moving upstream and slows down to reverse its direction of motion. This is in complete agreement with the experimental observations of Bannik and Houtmann[16].

CONCLUDING REMARKS

The laminar, unsteady, compressible, full Navier-Stokes equations are integrated time accurately using the implicit, upwind, flux-difference splitting finite-volume scheme to study the transonic flow field around a 65° sharp-edged, cropped delta wing. First, the flow field has been constructed for a Reynolds number of 3.23×10^6, a Mach number of 0.85 and an angle of attack of 20° (Case I). A λ-shock system consisting of a ray shock beneath the primary vortex core and a transverse terminating shock has been captured. Behind the terminating shock, the leading-edge vortex core breaks down. Keeping the Reynolds number constant and the angle of attack fixed at 20°, the Mach number is increased to 0.90. The results of this case (Case II) show that the terminating shock moves downstream and the vortex-breakdown region becomes smaller than that of Case I. Keeping the Reynolds number constant and the Mach number fixed at 0.85, the angle of attack is increased to 20°. The results of this case (Case III) show that the terminating shock moves upstream and the vortex-breakdown region becomes larger than that of Case I. The computational results are in good agreement with the experimental data. However, it must be emphasized that the flow at the terminating shock and behind it is time dependent while the flow ahead of the terminating shock is steady. The present paper shows the structure of the flow field behind the terminating shock for the first time.

ACKNOWLEDGEMENT

For the first two authors, this work is supported by the NASA-Langley Research Center under grant No. NAG-1–994 along with a partial support from the AFOSR. The Computational Resources provided by the NAS Center at Ames and the NASA Langley Research Center are acknowledged and appreciated.

REFERENCES

1. Marsden, D. J., Simpson, R. W. and Rainbird, W. J., "The Flow Over Delta Wings at Low Speeds with Leading Edge Separation," College of Aeronautics, Cranfield, Rep. CoA-114, 1957.

2. Lambourne, N. C. and Bryer, D. W., "Some Measurements in the Vortex Flow Generated by a Sharp Leading Edge Having 65 Degrees of Sweep," Aeronautical Research Council, CP No. 477, 1960.

3. Hummel, O., "On the Vortex Formation Over a Slender Wing at Large Angles of Incidences," AGARD CP-247, January 1979, pp. 15.1–15.7.

4. Verhaagen, N. G., "An Experimental Investigation of the Vortex Flow Over Delta and Double Delta Wings at Low Speed," AGARD CP-342, April 1983, pp. 7.1–7.16.

5. Kandil, O. A., "Numerical Prediction of Vortex Cores from the Leading and Trailing Edges of Delta Wings," ICAS Paper No. 14.2, 12th Congress of the International Council of Aeronautical Sciences, Munich, Germany, October 1980.

6. Hoeijmakers, H. W. M., "Aerodynamics of Vortical Type Flows in Three Dimensions," AGARD CP-342, July 1983, pp. 18.1–18.35.

7. Newsome, R. W. and Kandil, O. A., "Vortical Flow Aerodynamics-Physical Aspects and Numerical Simulation," AIAA Paper 87–0205, January 1987.

8. Thomas, J. L., Taylor, S. L. and Anderson, K., "Navier-Stokes Computations of Vortical Flows Over Low Aspect Wings," AIAA Paper 87–0207, January 1987.

9. Kandil, O. A. and Chuang, H. A., "Computation of Vortex-Dominated Flow for a Delta Wing Undergoing Pitching Oscillation," AIAA Journal, Vol. 28, No. 9, September 1990, pp. 1589–1595.

10. Stanbrook, A. and Squire, L. C., "Possible Types of Flow at Swept Leading Edges," Aeronautical Quarterly, Vol. XV, Feb. 1964.

11. Miller, D. S. and Wood, R. W., "Lee-Side Flow Over Delta Wings at Supersonic Speeds," NASA TP 2430, 1985.

12. Kandil, O. A. and Chuang, A. H., "Influence of Numerical Dissipation on Computational Euler Equations for Vortex-Dominated Flows," AIAA Journal, Vol. 25, No. 11, November 1987, pp. 1426–1434.

13. Newsome, R. W. and Thomas, J. L., "Computation of Leading-Edge Vortex Flows," NACA CP-2416, October 1985, pp. 305–330.

14. Murman, E. M., Goodsell, A., Powell, K. and Landahl, M., "Leading Edge Vortex Solutions with Large Total Pressure Loss," AIAA Paper 87–0039, January 1987.

15. Boersen, S. J. and Elsenaar, A., "Tests on the AFWAL 65° Delta Wing at NLR: A Study of Vortex Flow Development Between Mach = 0.4 and 4," Proceedings of Symposium on International Vortex Flow Experiment on Euler Code Validation, Stockholm, Sweden, October 1–3, 1986, pp. 23–36.

16. Bannik, W. J. and Houtman, E. M., "Experiments on the Transonic Flow Over a Delta Wing at High Angles of Attack," Proceedings of Symposium on International Vortex Flow Experiment on Euler Code Validation, Stockholm, Sweden, October 1–3, 1986, pp. 37–46.

17. Hartmann, K., "Force and Pressure Measurements Including Surface Flow Visualization on a Cropped Delta Wing," Proceedings of Symposium on International Vortex Flow Experiment on Euler Code Validation, Stockholm, Sweden, October 1–3, 1986, pp. 63–87.

18. Bütefisch, K. A., Pallek, D. and Sauerland, K. H., "International Vortex Flow Experiment-Results of Three Component LDA Measurements on a 65° Delta Wing," DFVLR IB 222–87 A 34, 1987.

19. Elsenaar, A., Hjelmberg, L., Bütefisch, K. and Bannink, W. J., "The International Vortex Flow Experiment," AGARD-CP-437, Lison, Portugal, May 1988, Vol. 1., pp. 9.1–9.23.

20. Bannink, W. J. and Houtman, E. M., "Experimental and Computational Study of the Vortical Flow Over a Delta wing at High Angles of Attack," IUTAM Symposium on Fluid Dynamics of High Angle of Attack, University of Japan, Tokyo, Japan, September 14–17, 1992.

21. Erickson, G. E., "Wind Tunnel Investigation of The Interaction and Breakdown Characteristics of Slender-Wing Vortices at Subsonic, Transonic and Supersonic Speeds," NASA Tech. paper 3114, November 1991.

22. Hitzel, S. M., "Wing Vortex-Flows Up into Vortex-Breakdown-A Numerical Simulation," AIAA 88-2518-CP, 1988, pp. 73–83.

23. Laine, S., Siikonen, T. and Kaurinkoski, P-, "Calculation of Transonic Viscous Flow Around a Delta Wing," ICAS 92–4.2.1, Beijing, PRC, September 22-25, 1992, pp. 286–295.

24. Kandil, O. A., Kandil, H. A. and Liu, C. H., "Shock-Vortex Interaction Over a 65-Degree Delta Wing in Transonic Flow," AIAA Paper 93–2973, AIAA 24th Fluid Dynamics Conference, Orlando, FL, July 6–9, 1993.

25. Kandil, O. A., Kandil, H. A. and Liu, C. H., "Supersonic Quasi-Axisymmetric Vortex Breakdown," AIAA 91–3311–CP, September 1991, pp. 851–863.

26. Kandil, O. A., Kandil, H. A. and Liu, C. H., "Three-Dimensional Supersonic Vortex Breakdown," AIAA 93–0526, January 11–14, 1993.

27. Kandil, H. A., "Navier-Stokes Simulation of Quasi-Axisymmetry and Three-Dimensional Supersonic Vortex-Breakdown," Ph.D. Dissertation, Dept. of Mechanical Engineering and Mechanics, Old Dominion University, Norfolk, VA, May 1993.

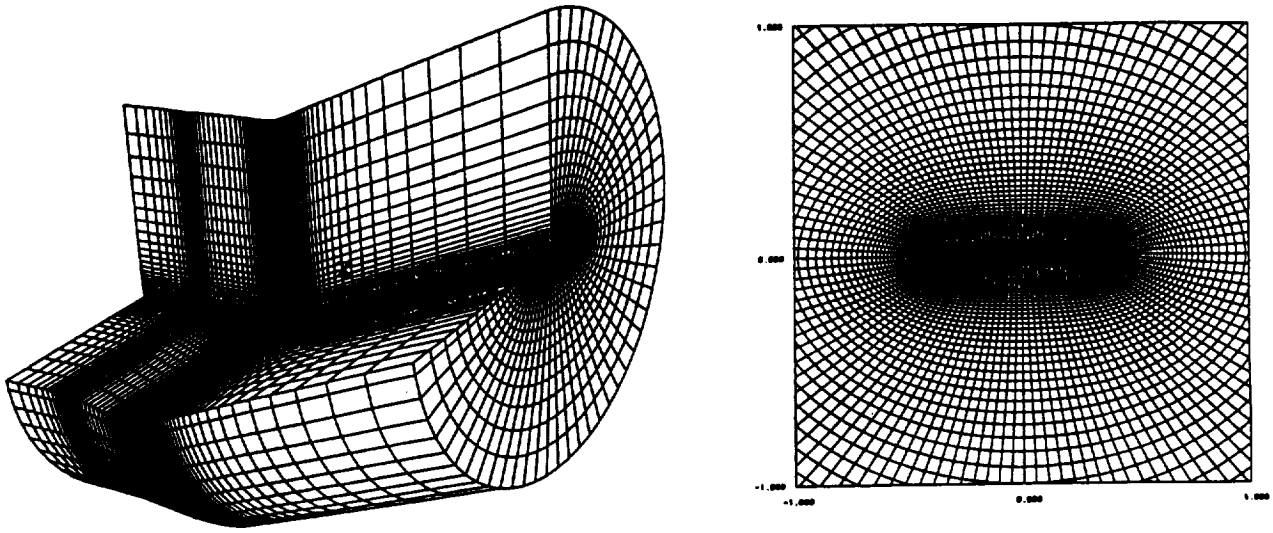

Fig. 1 Three-dimensional shape and cross-flow plane of a fine grid, 125×85×84.

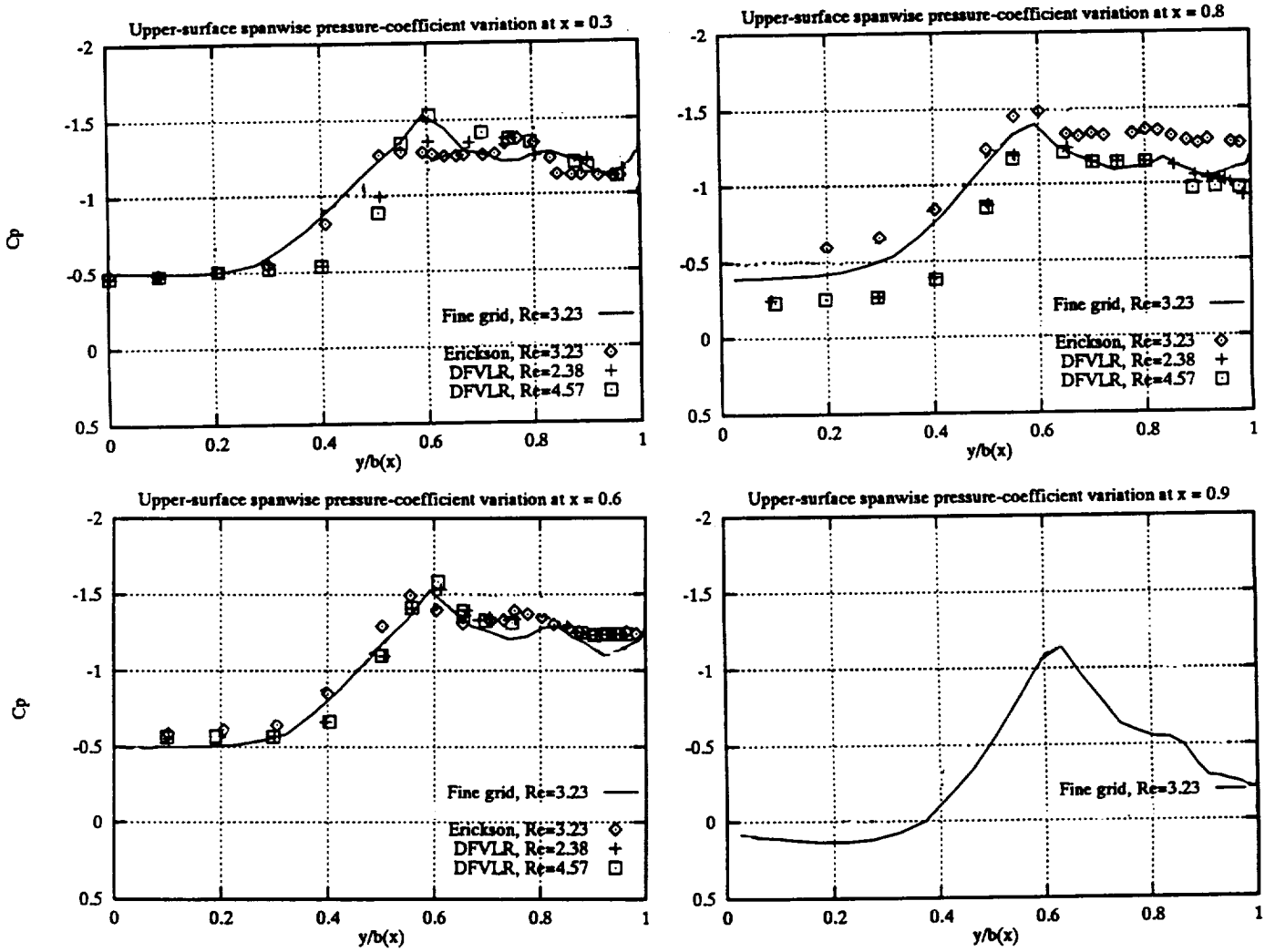

Fig. 2 Comparison of the computed and experimental spanwise, surface-pressure coefficient at different chord stations; $M_\infty = 0.85$, $\alpha = 20°$.

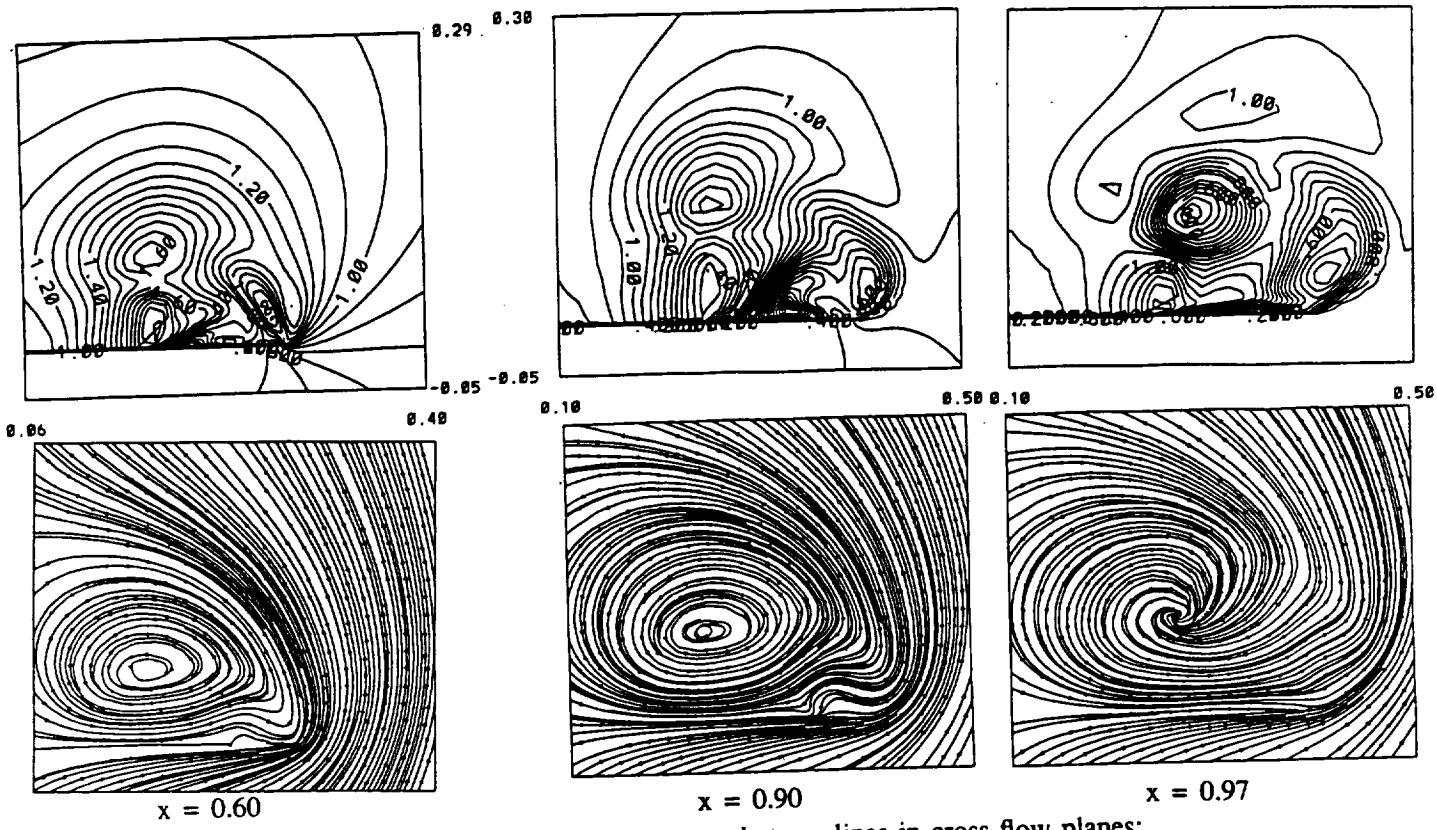

Fig. 3 Total-Mach contours and streamlines in cross-flow planes; $M_\infty = 0.85$, $\alpha = 20°$.

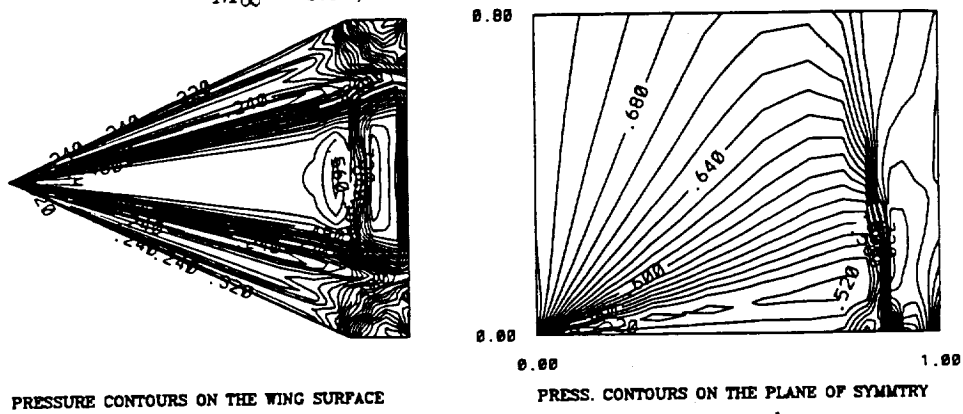

Fig. 4 Static-pressure contours on the wing and symmetry planes; $M_\infty = 0.85$, $\alpha = 20°$.

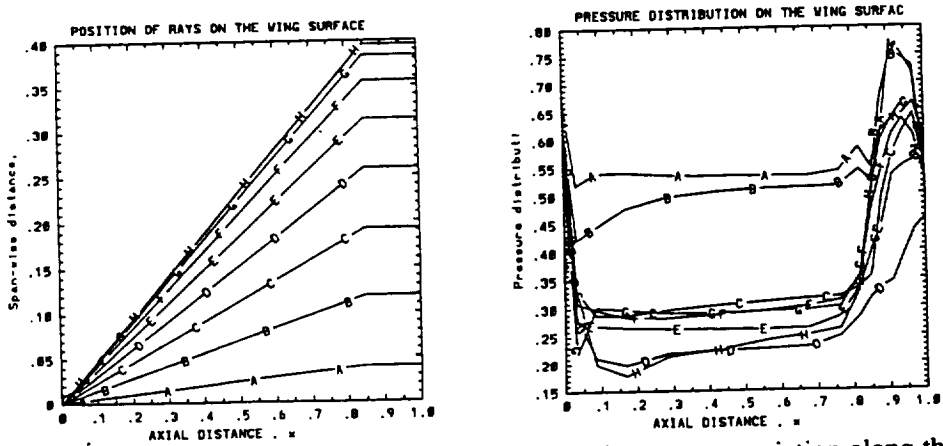

Fig. 5 Ray lines on the wing surface and the static-pressure variation along them; $M_\infty = 0.85$, $\alpha = 20°$.

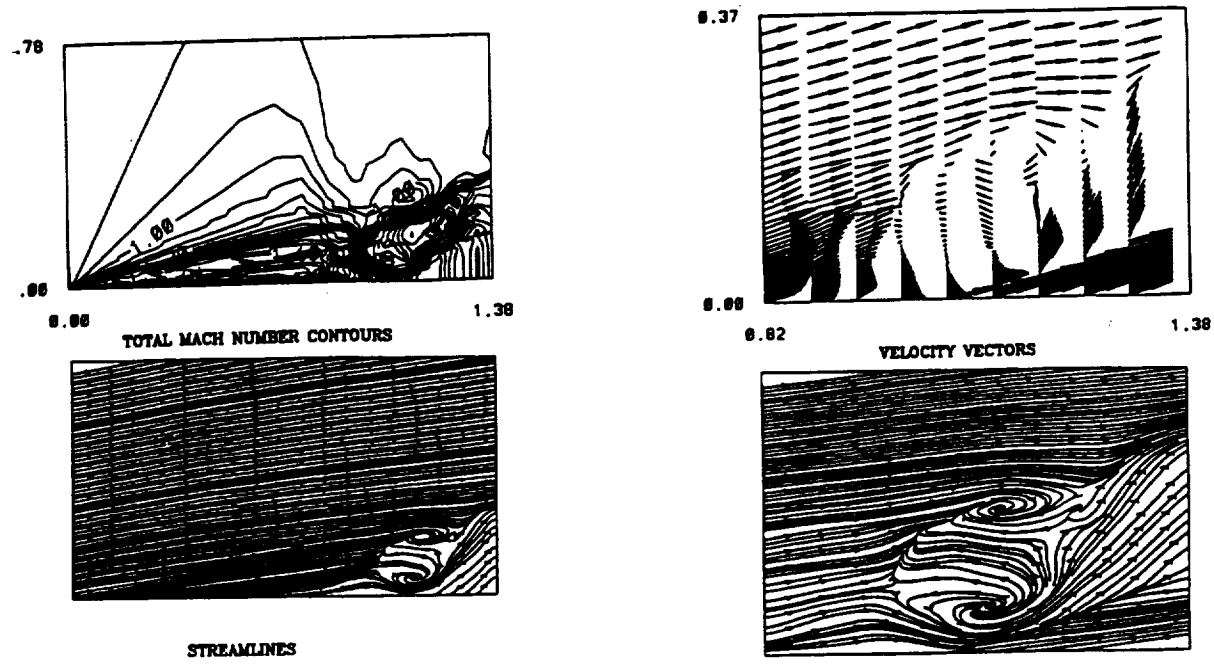

Fig. 6 Total-Mach contours, streamlines and velocity vectors on a ray plane passing through the vortex breakdown; $M_\infty = 0.85$, $\alpha = 20°$.

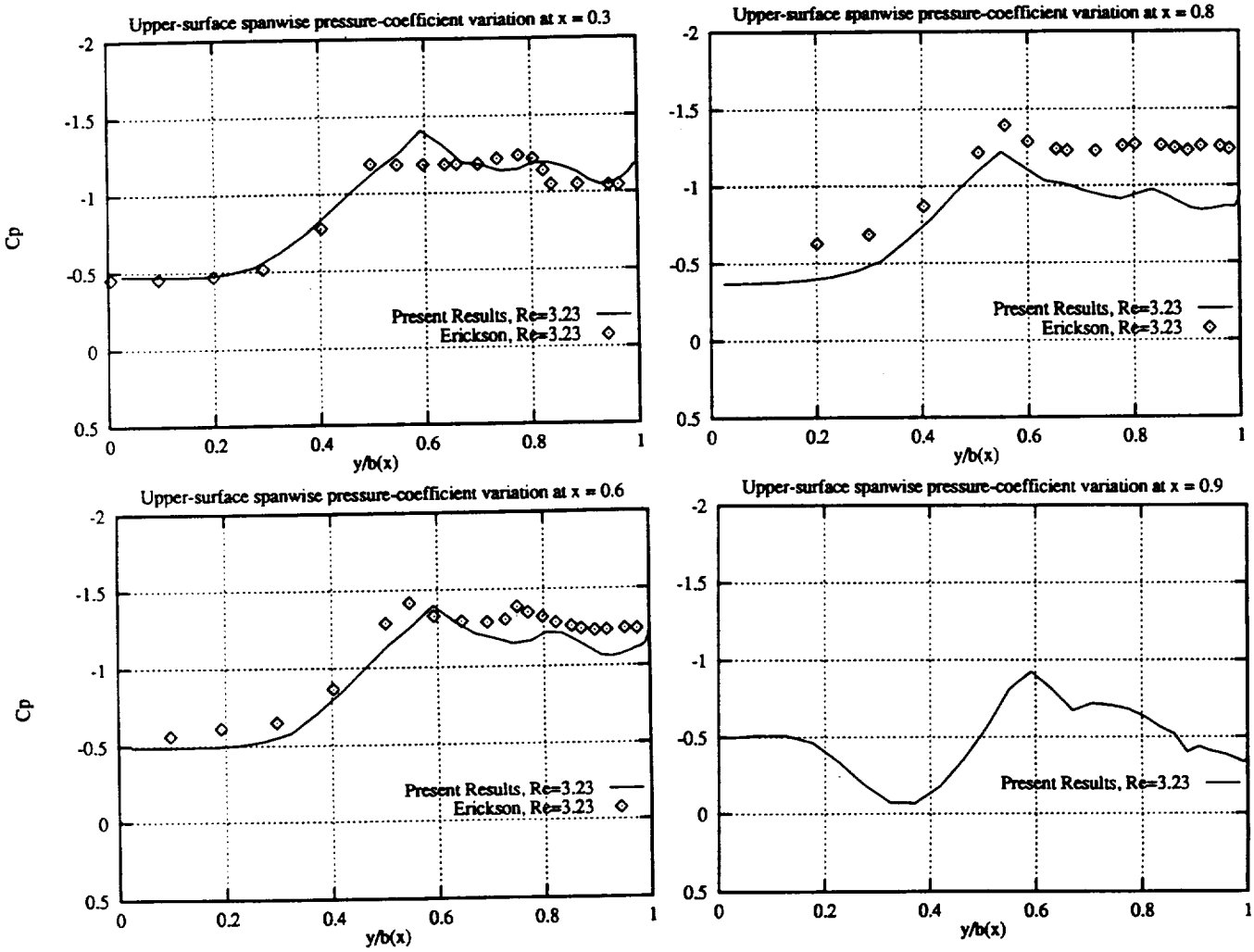

Fig. 7 Comparison of the computed and experimental spanwise, surface-pressure coefficient at different chord stations; $M_\infty = 0.90$, $\alpha = 20°$.

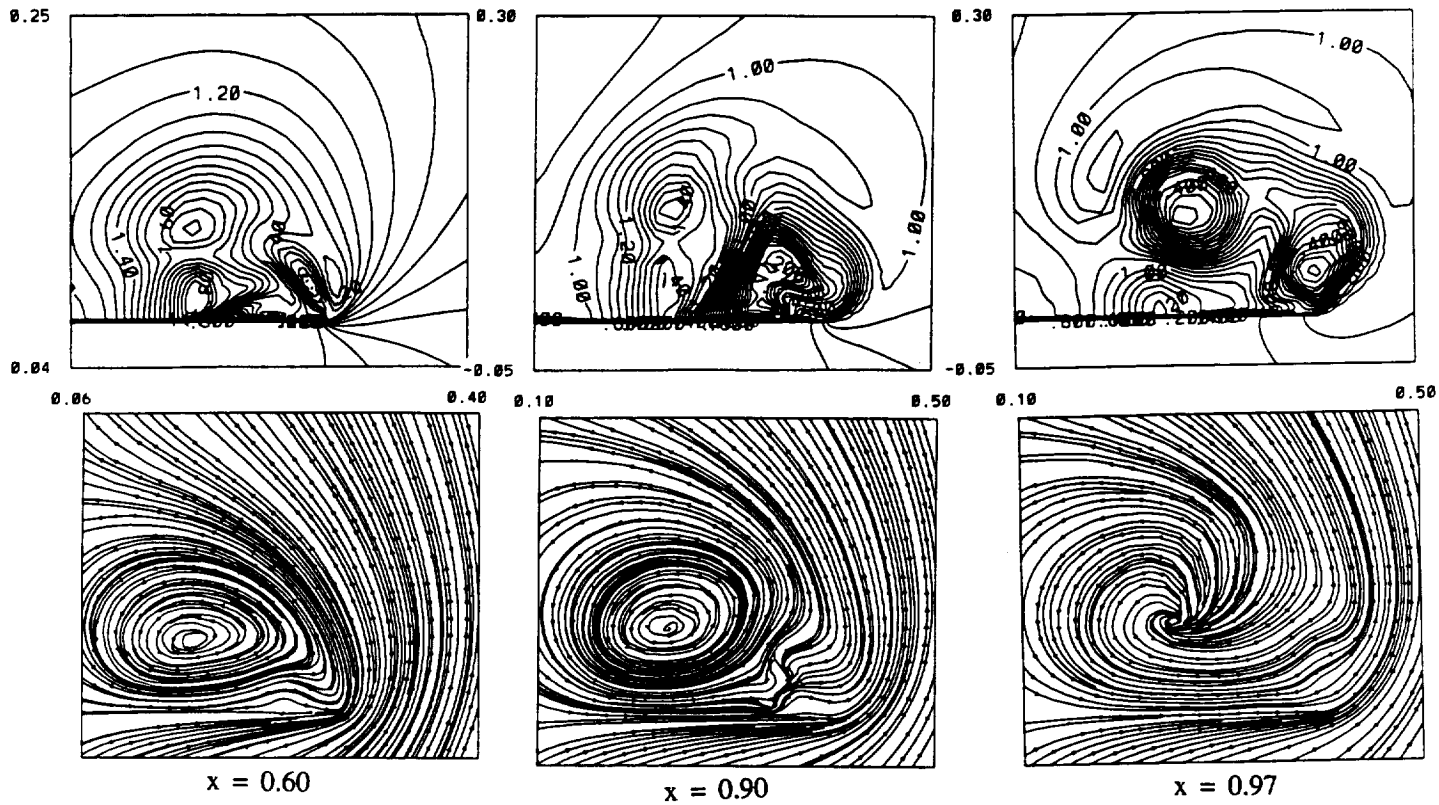

Fig. 8 Total-Mach contours and streamlines in cross-flow planes; $M_\infty = 0.90$, $\alpha = 20°$.

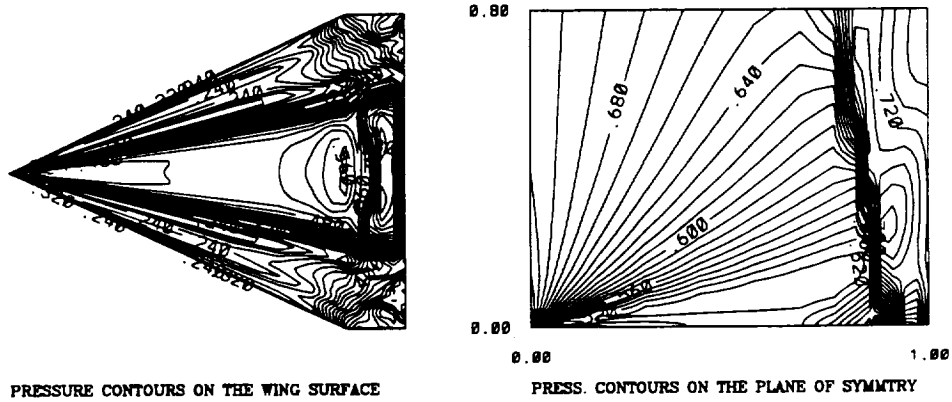

Fig. 9 Static-pressure contours on the wing and symmetry planes; $M_\infty = 0.90$, $\alpha = 20°$.

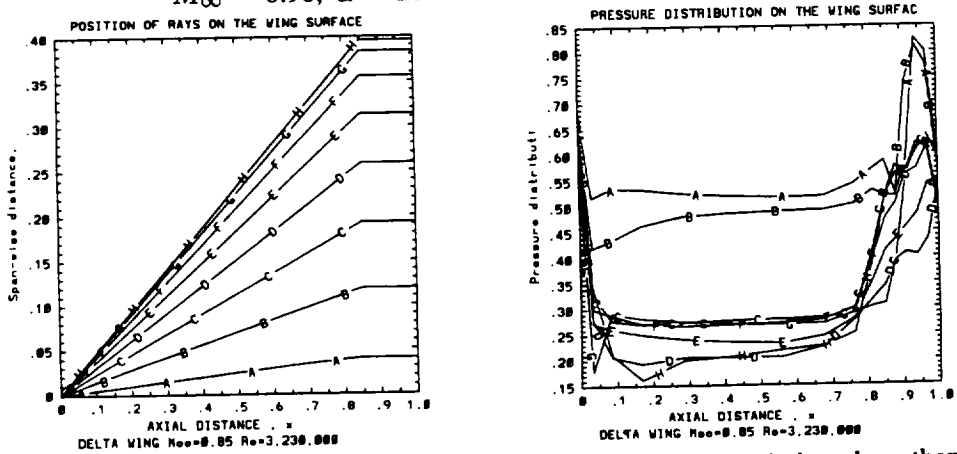

Fig. 10 Ray lines on the wing surface and the static-pressure variation along them; $M_\infty = 0.90$, $\alpha = 20°$.

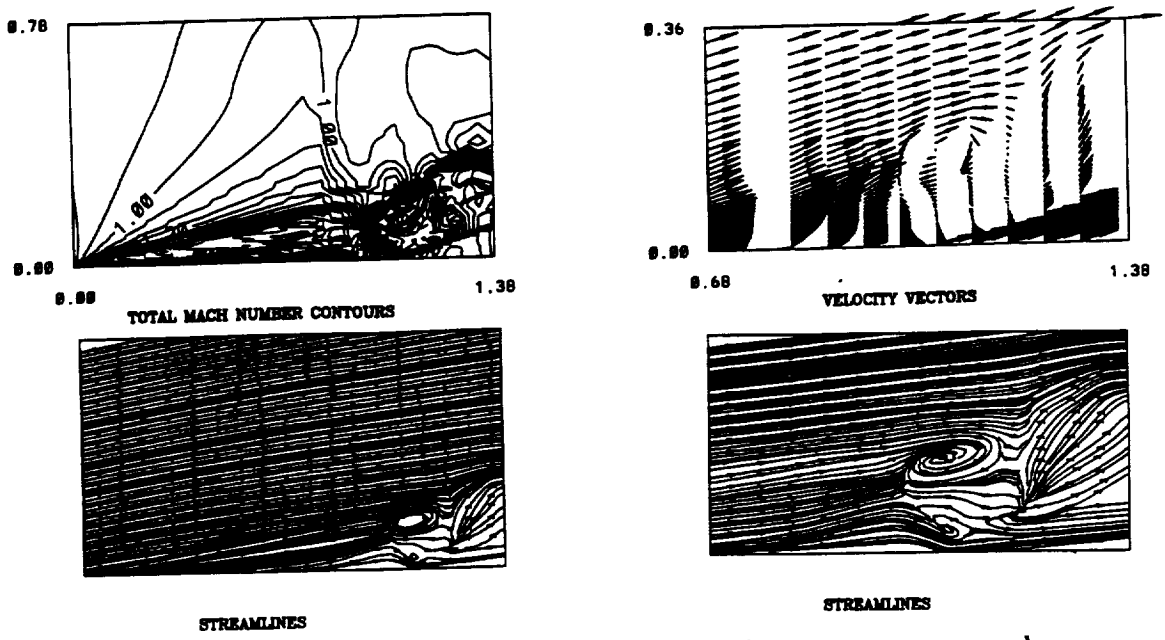

Fig. 11 Total-Mach contours, streamlines and velocity vectors on a ray plane passing through the vortex breakdown; $M_\infty = 0.9$, $\alpha = 20°$.

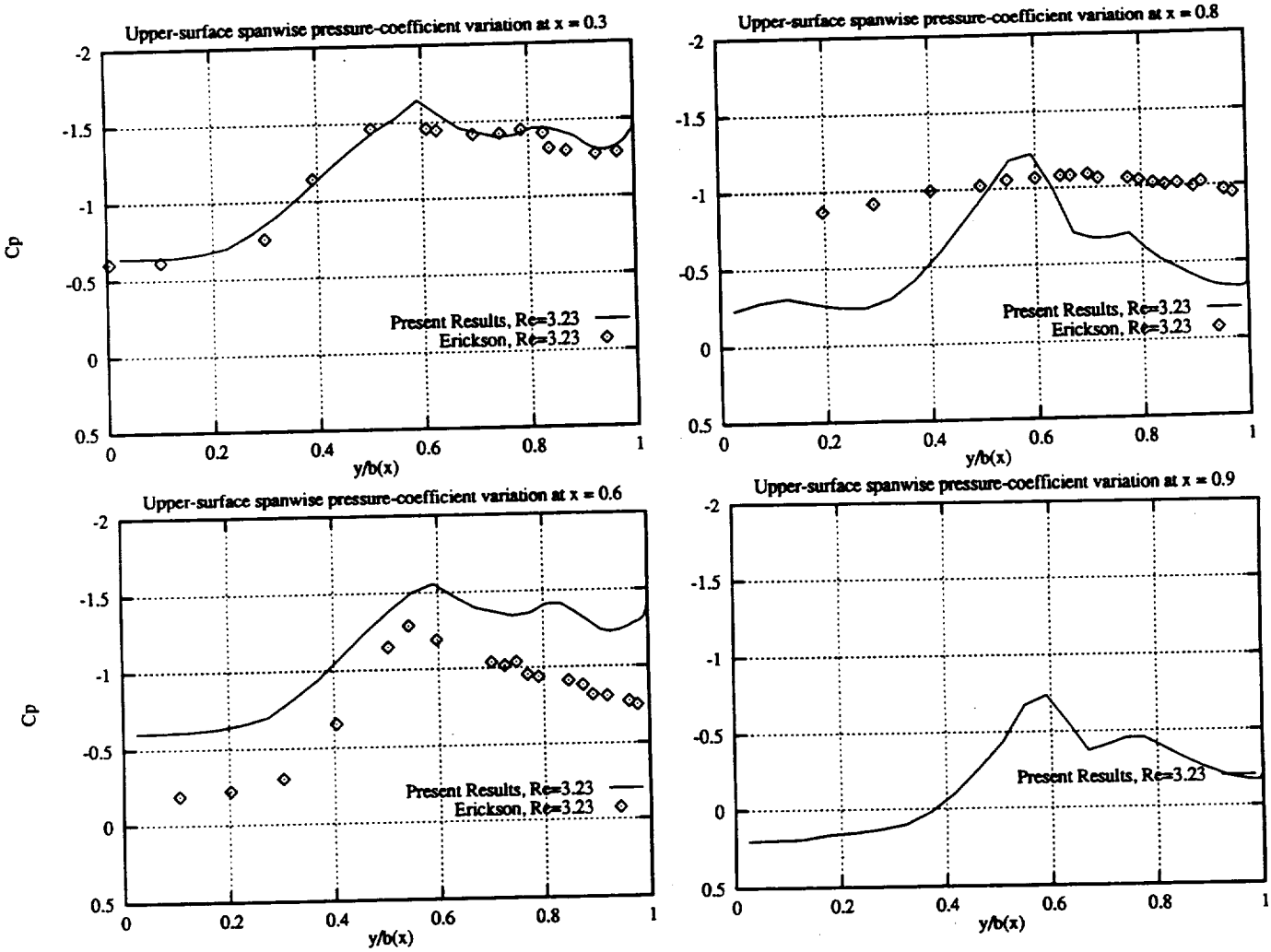

Fig. 12 Comparison of the computed and experimental spanwise, surface-pressure coefficient at different chord stations; $M_\infty = 0.85$, $\alpha = 24°$.

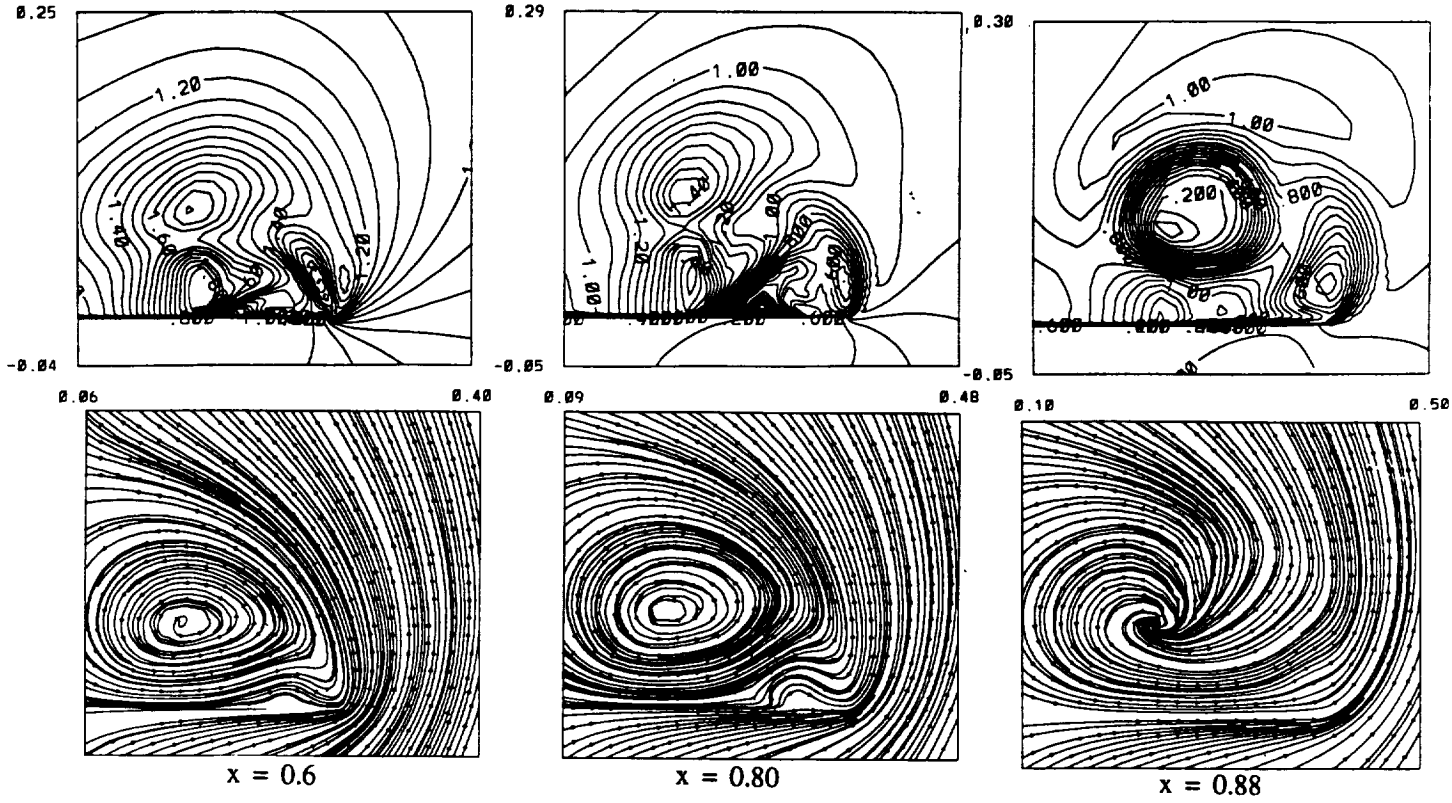

Fig. 13 Total-Mach contours and streamlines in cross-flow planes; $M_\infty = 0.85$, $\alpha = 24°$.

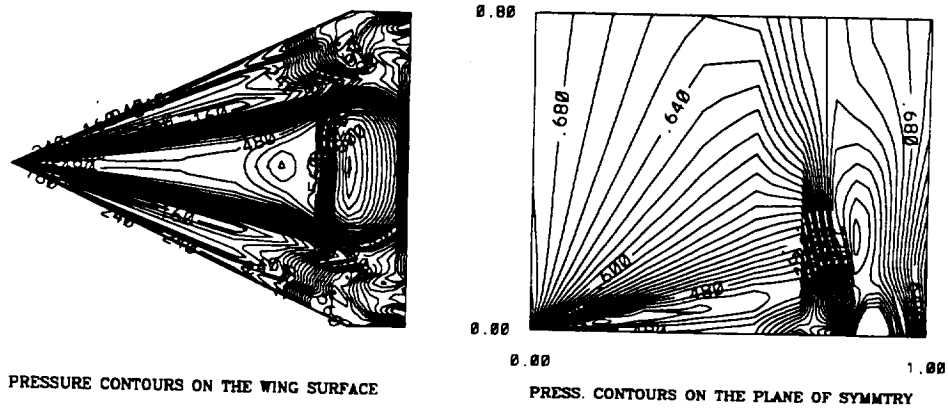

Fig. 14 Static-pressure contours on the wing and symmetry planes; $M_\infty = 0.85$, $\alpha = 24°$.

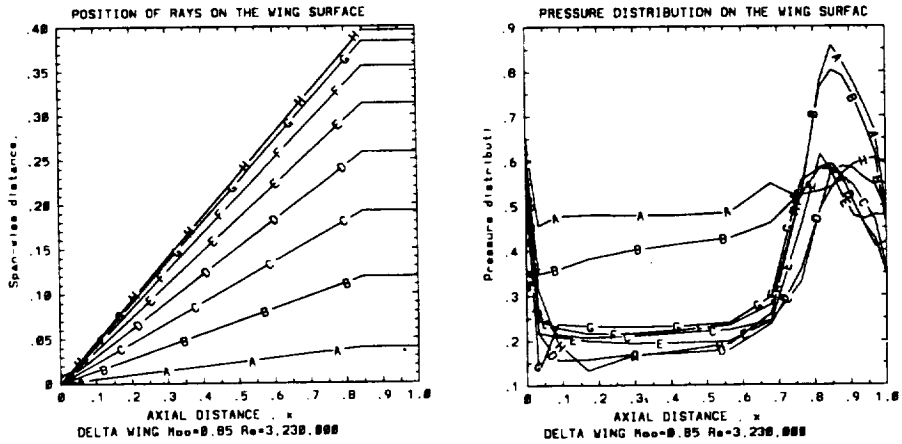

Fig. 15 Ray lines on the wing surface and the static-pressure variation along them; $M_\infty = 0.85$, $\alpha = 24°$.

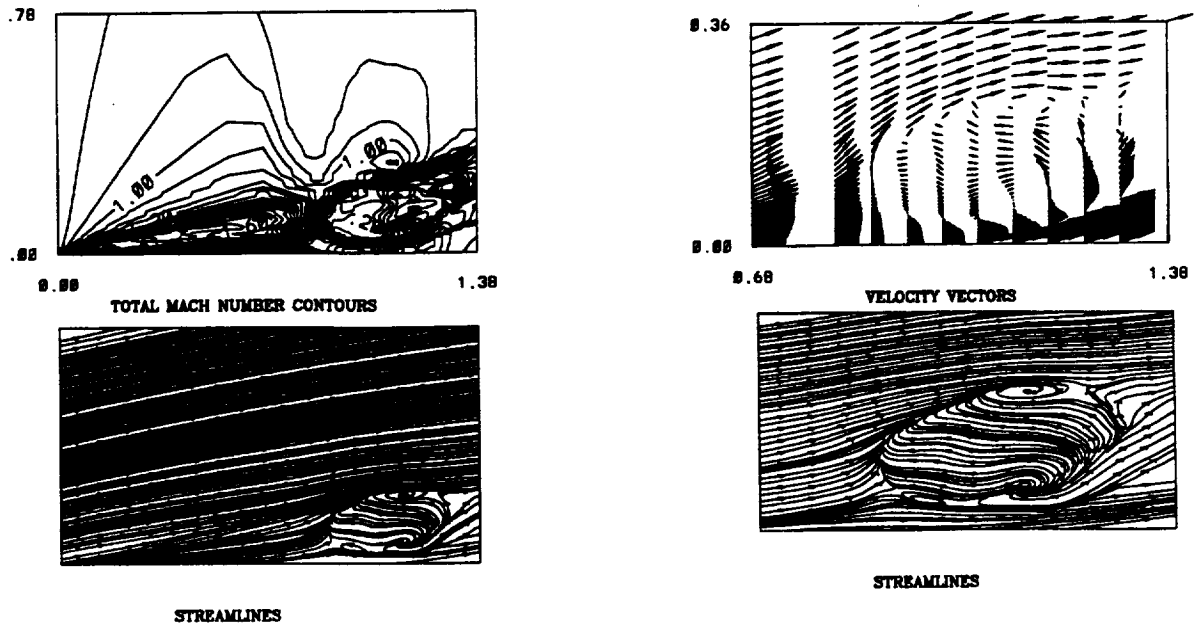

Fig. 16 Total-Mach contours, streamlines and velocity vectors on a ray plane passing through the vortex breakdown; $M_\infty = 0.85$, $\alpha = 24°$.

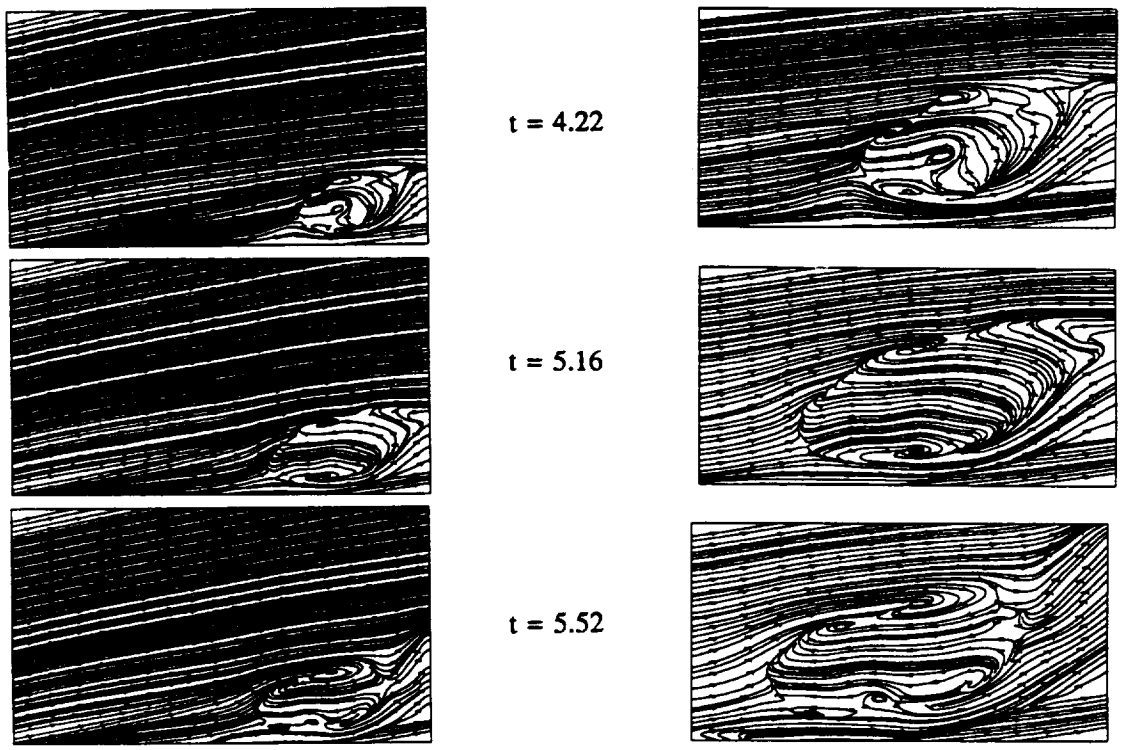

Fig. 17 Streamlines and blow-up on a ray plane passing through the vortex breakdown at different time levels; $M_\infty = 0.85$, $\alpha = 24°$.

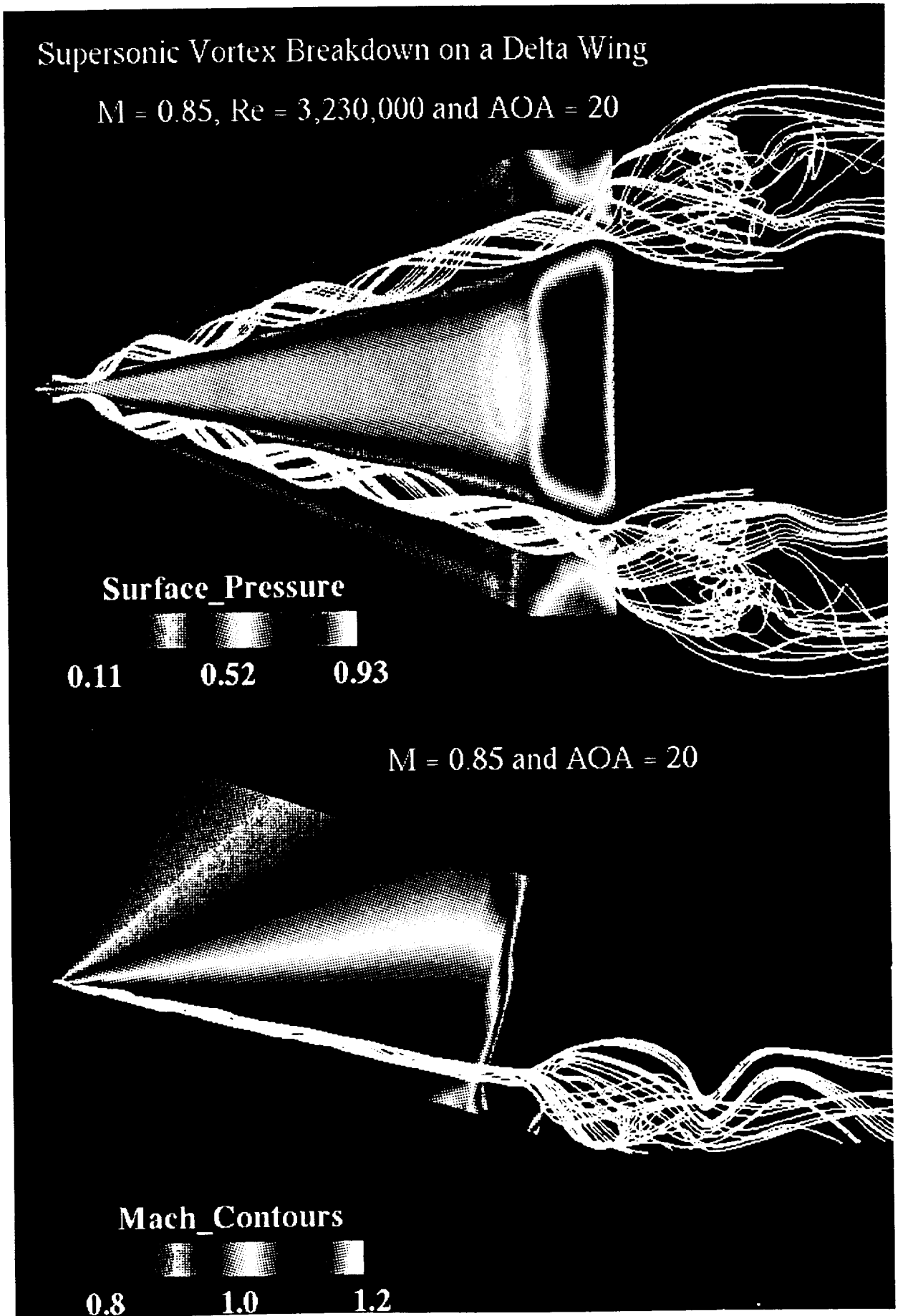

Fig. 18 Surface-pressure and Mach contours and particle trace on wing and symmetry planes; $M_\infty = 0.85$, $\alpha = 20°$.

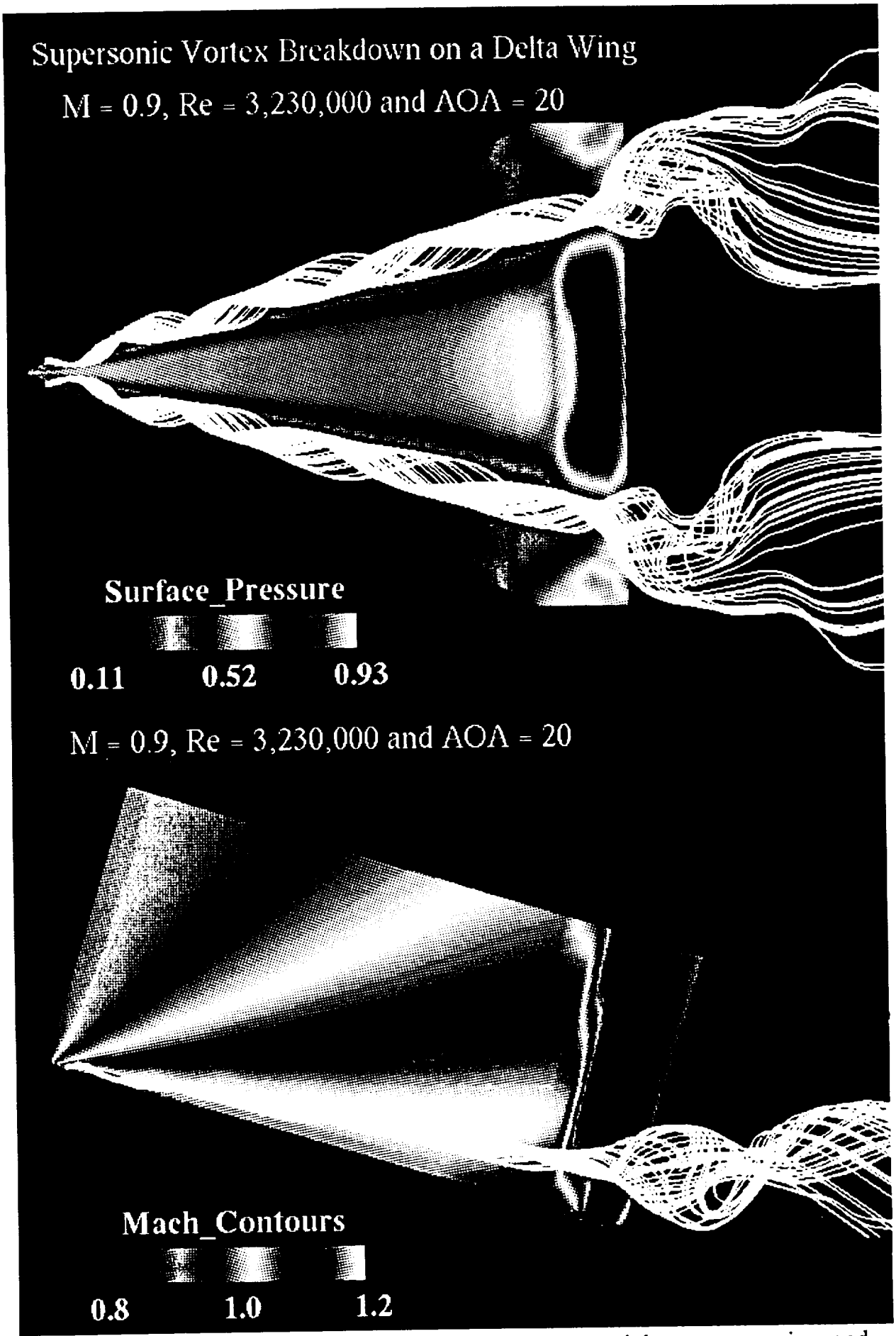

Fig. 19 Surface-pressure and Mach contours and particle trace on wing and symmetry planes; $M_\infty = 0.90$, $\alpha = 20°$.

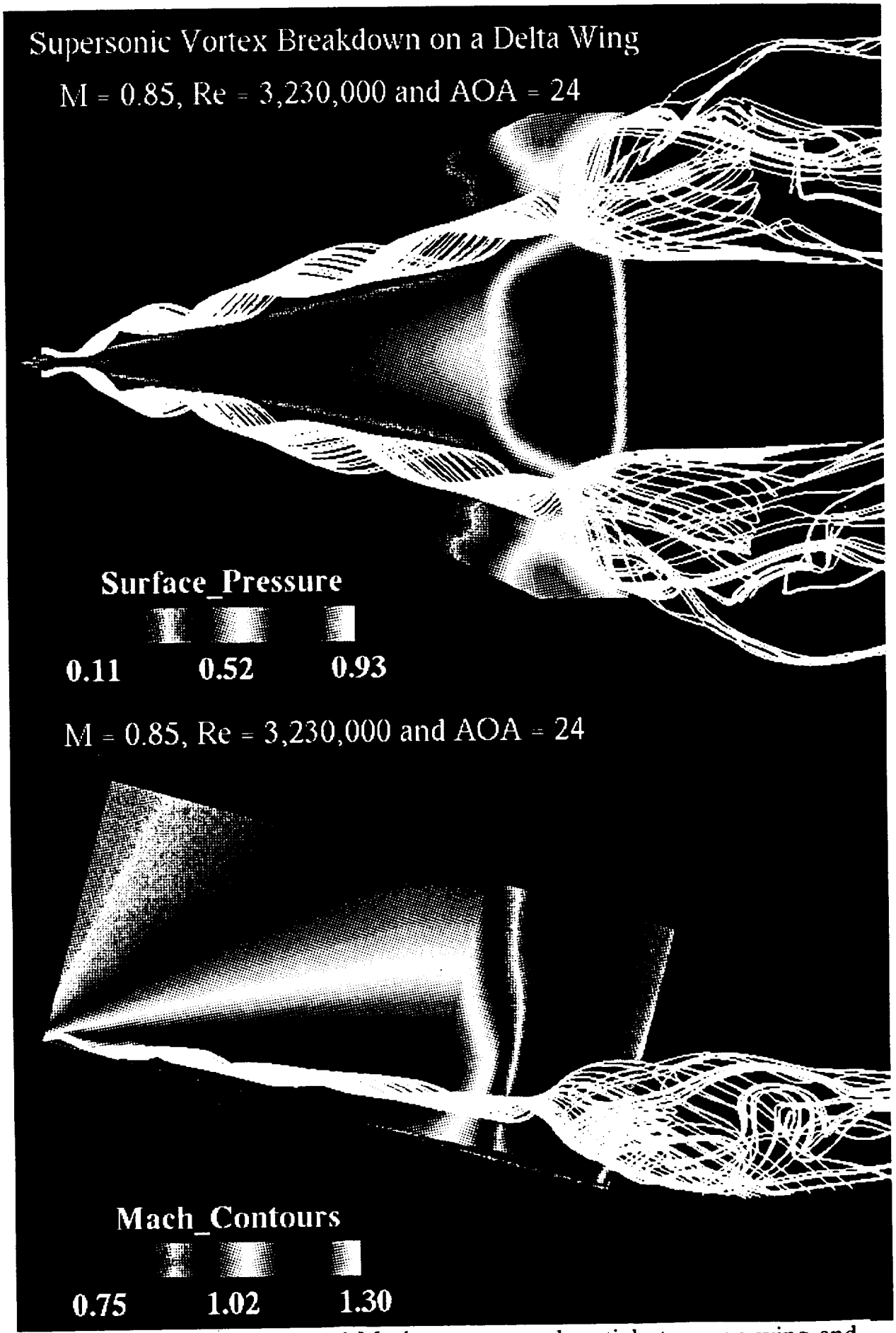

Fig. 20 Surface-pressure and Mach contours and particle trace on wing and symmetry planes; $M_\infty = 0.85$, $\alpha = 24°$.

ICAS 92-4.7.2

PREDICTION AND CONTROL OF SLENDER WING ROCK

Osama A. Kandil and Ahmed A. Salman
Old Dominion University, Norfolk, Virginia, USA

18th Congress, International
Council of the Aeronautical Sciences

Beijing, Peoples Republic of China
September 20-25, 1992

PREDICTION AND CONTROL OF SLENDER-WING ROCK

Osama A. Kandil* and Ahmed A. Salman**
Old Dominion University, Norfolk, VA 23529, USA

ABSTRACT

The unsteady Euler equations and the Euler equations of rigid-body dynamics, both written in the moving frame of reference, are sequentially solved to simulate the limit-cycle rock motion of slender delta wings. The governing equations of fluid flow and dynamics of the present multi-disciplinary problem are solved using an implicit, approximately-factored, central-difference like, finite-volume scheme and a four-stage Runge-Kutta scheme, respectively. For the control of wing-rock motion, leading-edge flaps are forced to oscillate anti-symmetrically at prescribed frequency and amplitude which are tuned in order to suppress the rock motion. Since the computational grid deforms due to the leading-edge flaps motion, the grid is dynamically deformed using the Navier-displacement (ND) equations. Computational applications cover locally-conical and three-dimensional solutions for the wing-rock simulation and its control.

INTRODUCTION

The dynamic phenomenon of wing rock is characterized by large-amplitude, high-frequency, rolling oscillation with a limit-cycle amplitude. The rolling oscillation is self excited and it is triggered by vortex-flow asymmetry or vortex breakdown on highly swept delta wings at high angles of attack. The study of this phenomenon is vital for the dynamic stability and controllability of high performance aircraft during maneuvering and landing.

The literature shows that several experimental investigations[1-6] have been conducted to gain basic understanding of the phenomenon. Nguyen, et al.[1] tested a flat-plate delta wing with 80° leading-edge sweep for forced-oscillation, rotary and free-to-roll tests. The free-to-roll tests showed that the wing exhibited a rock motion at angles of attack greater than 25°, and that the rock motion reached the same limit-cycle response irrespective of the initial conditions. Levin and Katz[2] tested two delta wings with leading-edge sweeps of 76° and 80°. They found that only the wing with the 80° sweep would undergo a rock motion. Nelson and his co-workers[3-5] conducted a series of experimental studies to investigate the mechanisms responsible for wing rock on a delta wing with 80° leading-edge sweep. Their analysis revealed that the primary mechanism for the phenomenon was a time lag in the position of the vortices normal to the wing surface. Moreover, they concluded, through the analysis of separate contributions of the wing upper and lower surface-pressure distributions, that the upper surface pressure provides all of the instability and little damping in the roll moment and that the lower surface pressure provides the classical roll damping hysteresis. Morris and Ward[6] conducted dynamic measurements in both a water tunnel and a wind tunnel on a delta wing with leading-edge sweep of 80°. Their results showed that the measured hysteresis loops in the water tunnel were opposite in direction to those of the wind tunnel. They concluded that the hysteresis direction does not play as decisive a role as previously thought in initiating and sustaining wing rock.

Erickson[7,8] analyzed experimental data for aircraft configurations at high angles of attack in an attempt to reveal the flow processes which generate wing rock. He concluded that wing rock phenomenon for slender wings is caused by asymmetric-leading-edge vortices and that the vortex breakdown provides a limiter to the growth of wing-rock amplitude. He also identified another two mechanisms for limit-cycle oscillations in roll for advanced aircraft.

The literature review showed that numerical simulation of this phenomenon for low speeds has recently been presented by Konstadinopoulos, et al.[9]. This has been followed by developments of analytical models to investigate the parameters affecting this phenomenon. Nayfeh, et al.[10-11] have presented two analytical models and Hsu and Lan[12] have presented one analytical model. The improved analytical model of Nayfeh, et al.[11] proved to be superior in comparison with the Hsu and Lan model and more accurate than their first model of reference[10]. The model of reference[11] accurately fitted the rolling moment coefficient, which was computed by a vortex-lattice method, using five terms which included the linear aerodynamic damping and restoring moments and the nonlinear aerodynamic damping moments. With this model, it was shown on the phase plane that both the wing rock and wing-roll divergence were possible responses for the wing. Hsu and Lan's model cannot predict wing-roll divergence. A serious question which can be raised regarding the work in references 9-12 is: how accurate the fluid dynamics solution is, using the vortex lattice method? Moreover, the fluid dynamics model limits its applicability to low-speed flows and to angles of attack below the critical value for vortex breakdown. Moreover, the vortex lattice model also cannot predict separated flows from smooth surfaces.

*Professor and Eminent Scholar, Department of Mechanical Engineering and Mechanics, Associate Fellow AIAA
**Graduate Student, Same Department, Member AIAA.

The first computational unsteady solution for the forced-rolling oscillation of a delta wing, which was based on the unsteady Euler equations, was presented by Kandil and Chuang[13]. The solution used the locally-conical flow assumption for supersonic flows in order to reduce the computational time by an order of magnitude as compared to that of the three-dimensional solutions. Forced-pitching oscillation of airfoils were also considered in a later paper by Kandil and Chuang[14]. The first unsteady three-dimensional Euler solution for the forced-pitching oscillation of a delta wing was also presented by Kandil and Chuang[15]. The unsteady Navier-Stokes solutions were also used by Kandil and Chuang[16] for the forced-rolling oscillation of a delta wing under the locally-conical flow assumption. Batina[17] developed a conical Euler solver, which was based on the use of unstructured grids, and used it to solve for the flow around a delta wing undergoing forced-rolling oscillation under the locally-conical flow assumption. Later on, Lee and Batina[18] extended the Euler solver to include a free-to-roll capability to solve for a freely rolling delta wing which exhibited wing rock. The solution was based on the locally-conical flow assumption. In Ref. 19, the present authors studied symmetric and anti-symmetric forced-rolling oscillations of the leading-edge flaps of a delta wing. A hinge is considered at the 75% location of the local half span and the leading-edge flaps are forced to oscillate both symmetrically and anti-symmetrically. The Navier-Stokes and Euler equations are used to solve the problem along with the Navier-displacement equation to account for the grid deformation due to the leading-edge flaps motion. In a later paper by the authors[20], the effects of symmetric and anti-symmetric flaps oscillation with varying frequencies have been investigated for two flow conditions. With the aid of these studies, the authors[21,22] studied the wing rock phenomenon as well as its active control using anti-symmetric tuned oscillations of the wing leading-edge flaps. The sequential solutions of unsteady Euler equations and the Navier-displacement equations along with the Euler equation of rigid-body rolling motion were used to obtain the solutions for these problems. The locally-conical flow assumption was also used throughout these solutions. Simulation of wing-rock and wing-divergence motions was presented by the authors for the three-dimensional flows in Ref. 23.

In the present paper, the unsteady Euler equations and the Euler equations of rigid-body dynamics, both written in the moving frame of reference, are used to simulate the limit-cycle rock motion of slender delta wings. Controlling the wing-rock motion is achieved by using anti-symmetric forced-oscillation of the wing leading-edge flaps. For the active control of wing rock, the grid is dynamically deformed using the ND equations.

FORMULATION

The formulation of the problem consists of three sets of equations. The first set is the unsteady, compressible, Euler equations which are written relative to a moving frame of reference. This set is used to compute the flowfield for steady or unsteady flows. The second set is the unsteady, linearized, Navier-displacement equations which are used in the moving frame of reference to compute the grid displacements whenever the leading-edge flaps oscillate. If the leading-edge flaps do not oscillate, the ND equations are not used. The third set is the Euler equations of rigid-body motion for the wing only or for the wing and its flaps. This set is used to compute the wing motion for the wing-rock problem. It is solved in sequence with the first set. For the control of wing-rock motion, this set is solved in sequence with the first and second sets.

Unsteady Euler Equations

Using the transformation equations from the space-fixed frame of reference to a moving frame of reference (Refs. 13-15), the non-dimensional, unsteady, compressible, Euler equations are transformed to the moving frame of reference. Such a transformation eliminates the motion of the computational grid for rigid wings having time-dependent rigid-body motion. Since the flaps of the wings are allowed very small relative rigid-body motion per time step of the integration scheme, one must consider the computational grid as time-dependent whenever the grid is updated, and the grid speed in Eqs. (4) and (5) must be computed. Hence, the Euler equations are given by

$$\frac{\partial \bar{Q}}{\partial t} + \frac{\partial \bar{E}_l}{\partial \xi^l} = \bar{S} \tag{1}$$

where

$$\bar{Q} \equiv \text{flowfield vector} = \frac{\hat{q}}{J} = \frac{1}{J}[\rho, \rho u_1, \rho u_2, \rho u_3, \rho e]^t \tag{2}$$

$$\xi^m = \xi^m(x_1, x_2, x_3, t) \tag{3}$$

$$\begin{aligned}\bar{E}_m \equiv \text{inviscid flux} &= \frac{1}{J}\left(\partial_k \xi^m \hat{E}_k + \frac{\partial \xi^m}{\partial t}\hat{q}\right) \\ &= \frac{1}{J}[\rho U_m, \rho u_1 U_m + \partial_1 \xi^m p, \rho u_2 U_m \\ &\quad + \partial_2 \xi^m p, \rho u_3 U_m + \partial_3 \xi^m p, \rho U_m h - \frac{\partial \xi^m}{\partial t} p]^t\end{aligned} \tag{4}$$

$$U_m = \partial_k \xi^m u_k + \frac{\partial \xi^m}{\partial t} \tag{5}$$

$$\bar{S} \equiv \text{source term due to rigid-body motion} = \frac{1}{J}\hat{S}$$
$$= \frac{1}{J}\{0, -\rho(a_t)_1, -\rho(a_t)_2, -\rho(a_t)_3, -\rho[\bar{V}\cdot\bar{a}_o + (\bar{\omega}\mathrm{x}\bar{r})\cdot\bar{a}_o + \bar{V}_o\cdot(\bar{a}_t - \bar{\omega}\mathrm{x}\bar{V}) + \bar{V}\cdot(\dot{\bar{\omega}}\mathrm{x}\bar{r}) + (\bar{\omega}\mathrm{x}\bar{r})\cdot(\dot{\bar{\omega}}\mathrm{x}\bar{r})]\}^t \quad (6)$$

$$\bar{V} = \bar{V}_a - \bar{V}_t \equiv \text{relative velocity} \quad (7)$$

$$\bar{V}_t = \bar{V}_o + \bar{\omega}\mathrm{x}\bar{r} \quad (8)$$

$$\bar{a}_t = \bar{a}_o + \dot{\bar{\omega}}\mathrm{x}\bar{r} + 2\bar{\omega}\mathrm{x}\bar{V}_o + \bar{\omega}\mathrm{x}(\bar{\omega}\mathrm{x}\bar{r}) \quad (9)$$

$$p = \rho(\gamma-1)\left(e - \frac{V^2}{2} + \frac{V_t^2}{2}\right) \quad (10)$$

$$h = \frac{\gamma p}{\rho(\gamma-1)} + \frac{V^2}{2} - \frac{V_t^2}{2} \quad (11)$$

The reference parameters for the dimensionless form of the equations are $L, a_\infty, L/a_\infty$ and ρ_∞ for the length, velocity, time and density, respectively. Here, L is a reference length which is taken as the wing root-chord length.

In Eqs. (1)-(11), the indicial notation is used for convenience. Hence the indices k, l, n and s are summation indices and m is a free index. The range of k, l, m, n, and s is 1–3 and $\partial_k \equiv \frac{\partial}{\partial x_k}$.

The term $\frac{\partial \xi^m}{\partial t}$ represents the mth component of the grid velocity. It is set equal to zero when the grid is not being updated. In Eqs. (1)-(11), ρ is the density, u_n the relative fluid velocity component, $\bar{V}_o$ and $\bar{a}_o$ translation velocity and acceleration of the moving frame, $\bar{V}_t$ and $\bar{a}_t$ the transformation velocity and acceleration from the space-fixed to the moving frames of reference, $\bar{\omega}$ and $\dot{\bar{\omega}}$ the angular velocity and acceleration of the moving frame, $\bar{r}$ the fluid position vector, p the pressure, e and h the total energy and enthalpy per unit mass relative to the moving frame and γ the gas index which is set equal to 1.4.

Unsteady, Linearized Navier-Displacement Equations

The details of the derivation of these equations are given by the authors in Ref. 20. The dimensionless form of these equations is given by

$$-\nabla p + \frac{\mu M_\infty}{R_{em}}\frac{\partial}{\partial t}\left[\frac{1}{3}\nabla(\nabla\cdot\bar{u}) + \nabla^2\bar{u}\right] = \rho\frac{\partial^2\bar{u}}{\partial t^2} \quad (12)$$

where $\bar{u}$ is the displacement vector of a grid point. For each grid point (a fluid element), Eq. (12) is integrated over a short time range $(t - t_o)$ where λ, μ and ρ are kept constants. This yields the equation

$$-\int_{t_o}^{t}\nabla p dt + \frac{\mu M_\infty}{R_{em}}\left[\frac{1}{3}\nabla(\nabla\cdot\bar{u}) + \nabla^2\bar{u}\right] = \rho\frac{\partial\bar{u}}{\partial t} + \bar{C}_o(\bar{r}) \quad (13)$$

In Eq. (12), we use R_{em} to refer to the mesh point Reynolds number which is different from the flow Reynolds number. This has been done in order to provide a limiter for the grid displacement to avoid grid distortion or overlapping, particularly in regions of high flow reversal. Equation (13) is the vector form of the ND equations to be used for computing the grid-points displacement $\bar{u}$ subject to displacement boundary and initial conditions. The equation is a parabolic equation in time which is integrated by using the alternating direction implicit (ADI) scheme. The constant $\bar{C}_o(\bar{r})$ in Eq. (13) is computed from the preceding time-range integrations.

Euler Equation of Rolling Rigid Wing With and Without Oscillating Leading-Edge Flaps:

Figure 1 shows a sketch of a wing and its flaps which are undergoing rolling motions. The rolling motion of the flaps is anti-symmetric. The wing is fixed to an axile which rotates in bearings. The bearings damping coefficient is λ. Torsional springs of stiffness $\hat{k}$ are assumed at the ends of the axle. The xyz axes which are fixed to the wing are assumed to coincide with the principal axes of inertia of the wing-flaps configuration. At section A-A, the wing half span is l_1 and the flap width is l_2. The masses of the wing and each flap are m_1 and m_2, respectively, and their respective mass-moment of inertias around their centers of mass are I_{c1} and I_{c2}. The generalized coordinates of the system are taken as θ_1 and θ_2, which are measured from the horizontal position. If the aerodynamic moment of the wing and its flaps about the x-axis is C_r and if one uses the Lagrangian dynamics for obtaining the governing equations of motion, one gets the following equation for the θ_1 coordinate

$$C_r - \left(2I_{xx2} - \frac{m_2}{2}l_2^2 - m_2 l_1 l_2\cos\theta_{21}\right)\ddot{\theta}_{21} + m_2 l_1 l_2\dot{\theta}_{21}^2\sin\theta_{21} = \left(I_{xx1} + 2I_{xx2} - \frac{m_2}{2}l_2^2 - m_2 l_1 l_2\cos\theta_{21}\right)\ddot{\theta}_1 - m_2 l_1 l_2\dot{\theta}_1^2\sin\theta_{21} - 2m_2 l_1 l_2\dot{\theta}_1\dot{\theta}_{21}\sin\theta_{21} + \lambda\dot{\theta}_1 + \hat{k}\theta_1 \quad (14)$$

where $\theta_{21} = \theta_2 - \theta_1$, I_{1xx} and I_{2xx} are the mass moment of inertia of the wing and the flap, respectively, around the wing axis of rotation. If the angles θ_1 and θ_{21} are assumed to be small, then the linearized equation reduces to

$$C_r - \left(2I_{xx2} - \frac{m_2}{2}l_2^2 - m_2 l_1 l_2\right)\ddot{\theta}_{21} = \left(I_{xx1} + 2I_{xx2} - \frac{m_2}{2}l_2^2 - m_2 l_1 l_2\right)\ddot{\theta}_1 + \lambda_1\dot{\theta}_1 + \hat{k}\theta_1 \quad (15)$$

On the other hand, if the flaps are not deflected and the wing and its flaps roll as a rigid body, Eq. (15) becomes

$$C_r = I_{zz}\ddot{\theta}_1 + \lambda\dot{\theta}_1 + \hat{k}\theta_1 \qquad (16)$$

where I_{zz} is the mass moment of inertial of the composite wing-flaps configuration without relative motion.

Equation (16) governs the wing-rock problem while Eq. (15) governs the linearized control of wing-rock problem by using a prescribed motion of the leading-edge flaps.

COMPUTATIONAL SCHEMES

The computational scheme used to solve Eqs. (1)-(11) is an implicit, approximately-factored, centrally-differenced, finite-volume scheme[13-15]. Added second-order and fourth-order explicit dissipation terms are used in the difference equation on its right-hand side terms, which represent the explicit part of the scheme. The Jacobian matrices of the implicit operator on the left-hand side of the difference equation are centrally-differenced in space, and implicit second-order dissipation terms are added for the scheme stability. The left-hand side spatial operator is approximately factored and the difference equation is solved in three sweeps in the ξ^1, ξ^2 and ξ^3 directions, respectively.

For the wing-rock problem, Eq. (16) is solved using a four-stage Runge-Kutta scheme. Starting from known initial conditions for θ and $\dot{\theta}$, the equation is explicitly integrated in time in sequence with the fluid dynamics equations, Eqs. (1-11). Equation (16) is used to solve for θ, $\dot{\theta}$ and $\ddot{\theta}$ while Eqs. (1-11) are used to solve for C_r. If the initial C_r is nonzero, a case of asymmetric steady flow at initial conditions, the initial values of θ and $\dot{\theta}$ are set equal to zero and the motion is initiated by the initial rolling moment.

For the control of the wing-rock problem using flaps oscillation, the motion of the flaps; θ_{21}, $\dot{\theta}_{21}$ and $\ddot{\theta}_{21}$ are specified and Eq. (14) (nonlinear equation) or Eq. (15) (linearized equation) is used to solve for θ_1, $\dot{\theta}_1$ and $\ddot{\theta}_1$. The fluid dynamics equations, Eqs. (1)-(11), and the grid-deformation equation, Eq. (13), are sequentially used to solve for C_r.

COMPUTATIONAL APPLICATIONS AND DISCUSSION

Simulation of Wing-Rock-Motion (Locally-Conical Flow)

A delta wing of sweep-back angle of 80°, at an angle of attack of 35° and a Mach number of 1.4 is considered. The wing has an elliptic section with sharpened leading edges. The wing mass-moment of inertia about its x axis is 0.02, the bearing damping coefficient is 0.2 and the spring stiffness is 0.74. The unsteady Euler equations are solved for locally-conical flows. The computational grid is of 64×64×2 in the wrap around, normal and axial directions, respectively. For these flow conditions, the steady flow is asymmetric, and hence $C_r \neq 0$ at t = 0. Therefore, we set $\theta_1^o = \dot{\theta}_1^o = 0$. The Euler equations of fluid flow and of rigid-body dynamics are sequentially integrated accurately in time with $\Delta t = 0.0025$. Figures 2 and 3 show the results of this case. Figure 2 shows the time responses of θ_1, C_r and C_n and the corresponding phase planes of $\dot{\theta}_1$ vz θ_1, C_r vz θ_1 and C_n vz θ_1. The time responses show the long time, $t \simeq 7$, it takes to build up the growing roll-angle response. The responses clearly show that the θ_1 and C_r continuously increase in time with increasing frequencies. The limit-cycle response is reached at $t \simeq 21$ which is clearly shown on the phase planes. The mean amplitude of θ_1 is –0.5°, its maximum is 40° and its minimum is –41°. Figure 3 shows snap shots of the surface-pressure coefficient and cross-flow velocity at the instants corresponding to points 1 and 2 on Fig. 2. The strong asymmetric motion of the primary vortices are clearly seen. Also, the surface-pressure-coefficient response clearly shows the generation of the restoring rolling moment to the wing motion.

Active Control of Wing Rock Using Leading-Edge Flaps Oscillation

The next step is to control the wing rock response of the previous case. For this purpose a leading-edge flap hinge is assumed to be at the 76% location of the local-half-span length. The flaps motion is introduced at $t_o = 13.02$ when $\theta_1 = -4°$ and $C_r = 0.0$. The flaps motion is anti-symmetric and is given by $\theta_{21}(t) = \theta_{21\,max} \sin k_f(t - t_o)$, where k_f is the flap reduced frequency. With the aid of the previous values of θ_1, C_r and k of the wing (can be measured by sensors to feed back the leading-edge flaps motion), we chose $\theta_{21\,max} = -0.5°$ and $k_f = 6.7$. Equation (15) for the wing-flaps motion is sequentially integrated accurately in time, with $\Delta t = 0.0025$, along with the Euler equations of fluid flow, and the ND equation is used for the grid deformation. Figure 4 shows the time responses of θ_1 and C_r for the wing. It is clearly seen that θ_1 response is damped within $t - t_o = 13$ with a mean value of 5°. However, the wing is still oscillating periodically around this mean position with a small amplitude. Next, the flaps motion is modified by dividing the amplitude $\theta_{21\,max}$ by $1 + (t - t_o)$ so that it decays with time. Figure 5 shows the steady response of the wing at t = 30. The wing assumes an equilibrium position of 5° without any oscillation. To check that this is a stable equilibrium position, the wing is disturbed at t = 40 with a small $\dot{\theta}_1$. Figure 5 also shows the time responses of θ_1 and C_r after the disturbance confirming that the equilibrium position is stable. Figure 6 shows the phase planes of the whole response history of θ_1 and C_r. Figures 7–9 show the same results as those of Figs. 4–6 when the same control is applied at $t_o = 23.27$, which is during the limit cycle response.

Simulation of Wing-Rock Motion (Three-Dimensional Flow)

Next, we consider the three-dimensional-flow simulation of the wing-rock problem.

A sharp-edged delta wing with a leading-edge sweep of 80° is considered for the computational applications. The angle of attack is set at 30° and the freestream Mach number is chosen as 0.3 for low speed simulation. The wing mass-moment of inertia about its axis is 0.285, the bearings damping coefficient is 0.15 and the torsional springs stiffness is 0.74. The unsteady Euler equations are solved for the three-dimensional flows. The boundary of the computational domain consists of a hemispherical surface with it center at the wing trailing edge on its line of geometric symmetry. The hemispherical surface is connected to a cylindrical aftersurface with its axis coinciding with the wing axis. The hemispherical and cylindrical radii are two root-chord lengths and the downstream, circular exit boundary is at two root-chord lengths from the wing trailing edge. The grid consists of $48\times32\times32$ grid points in the wrap-around, normal and axial directions, respectively. The grid is generated in the crossflow planes using a modified Joukowski transformation, which is applied at the grid-chord stations with exponential clustering at the wing surface.

Since the steady flow solution is asymmetric, C_r in Eq. (16) is of non-zero value and hence Eq. (16) is initially inhomogeneous. At t = 0, we set $\theta^o = \dot{\theta}^o = 0$ and release the wing with its initial M_x value as the driving rolling moment. At $t = \Delta t$, Eq. (16) of the wing dynamics is integrated to obtain θ_1 and hence $\dot{\theta}_1$ and $\ddot{\theta}_1$ ($\Delta t = 0.005$). Then, Eqs. (1-11) of the fluid flow are integrated to obtain the components of the flowfield vector and hence p and C_r. Next, t is increased to $2\Delta t$ and the sequential integration of the dynamics equation and the fluid flow equations is repeated. The sequential solutions are repeated until the limit-cycle amplitude response is reached

In Fig. 10, we show the roll angle, rolling-moment coefficient, C_r, and normal-force coefficient, C_n, versus time. Significant transient responses develop in the time range of $t = 0 \rightarrow 22$, wherein the amplitudes of the responses increase and decrease. Thereafter, $t > 22$, the amplitudes of the responses continuously increase until $t = 95$. At $t \geq 95$, the amplitudes and frequencies of the responses become periodic reaching the limit-cycle response. During the limit-cycle response, the maximum roll angle, $\theta_{1\,max}$, is 10°, the minimum roll angle, $\theta_{1\,min}$, is -11° and the period of oscillation is 3.53, which corresponds to a frequency of 1.78. With $\Delta t = 0.005$, each cycle of oscillation in the limit-cycle response requires 706 time steps. The shown responses, up to $t = 140$, required 28,000 time steps.

Next, we consider one cycle of the limit-cycle response and analyze the roll angle, rolling-moment-coefficient and normal-force-coefficient responses to gain physical insight of the wing-rock phenomenon. For this purpose, we show in Fig. 11 θ_1, C_r and C_n vz. t in the range of $t = 135.19 \rightarrow 138.72$. This period of oscillation is marked by the numbers 1, 2, 3, 4 and 5 in Fig. 11. In the first quarter of the cycle ($1 \rightarrow 2$), the roll angle of the left side of the wing decreases from $0° \rightarrow -11°$ and the wing rolls in the clockwise (CW) direction, the rolling-moment coefficient increases and changes sign from $-0.057 \rightarrow 0.0 \rightarrow +0.023$ and the normal-force coefficient decreases and then increases from $2.68 \rightarrow 2.65 \rightarrow 2.75$. It is important to notice that the rolling moment changes its sign which means that the rolling moment during the first part of this quarter of the cycle is in the CW direction (the same direction as the motion) and in the second part of this quarter of the cycle is in the CCW direction (the opposite direction of the motion). Hence, the rolling moment increases the negative angle in the first part and then it limits the growth of the roll angle in the second part. In the second quarter of the cycle ($2 \rightarrow 3$) the roll angle increases from $-11° \rightarrow 0$ and the wing rolls in the CCW direction, the rolling-moment coefficient increases and then decreases from $+0.023 \rightarrow 0.045 \rightarrow 0.04$ and the normal-force coefficients increases and then decreases from $2.75 \rightarrow 3.0 \rightarrow 2.84$. The rolling-moment coefficient is in the CCW direction (the same direction as the motion). In the third quarter of the cycle ($3 \rightarrow 4$) the roll angle increases from $0 \rightarrow 10°$ and the wing keeps its rolling motion in the CCW direction, the rolling-moment coefficient decreases and changes sign from $+0.04 \rightarrow 0 \rightarrow -0.038$ and the normal-force coefficient decreases and then increases from $2.84 \rightarrow 2.78 \rightarrow 2.86$. Again, it is noticed that the rolling moment changes its sign from CCW to CW directions and limits the roll angle growth.

In Figs. 12 and 13, we show snapshots at points 2 and 4, respectively; of the cross-flow-velocity vectors and the static-pressure contours at the chord stations of 0.54, 0.63 and 0.79 and the surface-pressure coefficient at the chord stations of 0.54 and 0.63. In Fig. 12, the primary vortex on the right side is nearer to the upper wing surface than the one on the left side. Moreover, the primary vortex on the right is further away from the plane of geometric symmetry in comparison to the one on the left. The surface-pressure curves show large peaks on the right side and that the surface-pressure difference on the right side is larger than the one on the left side. This results into a CCW rolling moment at this maximum negative roll angle of -11°. In Fig. 13, the opposite process occurs; the surface-pressure difference on the left side is larger than the one on the right side and this results into a CW rolling moment at this maximum positive roll angle of +10°. These results are consistent with those of the experimental data of Refs. 3 and 4.

In Fig. 14, we show the variations of the maximum static pressure of the vortex cores of the primary vortices

on the left and right sides versus the roll angle for the chord station of 0.54. The numbers on the figures correspond to those in Fig. 11. Since the maximum static pressure of the core is proportional to the vortex-core strength, it is obviously seen that the primary vortex on the right side has a greater strength at point 2 as compared to that on the left side. The strength differential between the right and left vortices along with the locations of the vortex cores contributes substantially to the net total CCW rolling moment which limits the negative growth of the roll angle and reverses the wing motion. Similarly, it is concluded that the strength differential between the left and right vortices at point 4 substantially contributes to the net total CW rolling moment which limits the positive growth of the roll angle and reverses the wing motion.

In Fig. 15, we split the rolling-moment coefficient into restoring and damping components similar to Konstadinopoulos, et al.[9]. First, the rolling-moment coefficient C_r is fitted using the following expansions in terms of θ and $\dot{\theta}$:

$$\begin{aligned} C_r = {} & a_1\theta + a_2\dot{\theta} + a_3\theta^3 + a_4\theta^2\dot{\theta} \\ & + a_5\dot{\theta}^2\theta + a_6\dot{\theta}^3 + a_7\theta^5 + a_8\theta^4\dot{\theta} \\ & + a_9\theta^2\dot{\theta}^3 + a_{10}\dot{\theta}^2\theta^3 + a_{11}\dot{\theta}^4\theta + a_{12}\dot{\theta}^5 \end{aligned} \tag{17}$$

The coefficients $a_1 - a_{12}$ are determined using a least-squares fit. A comparison of the original ($-\circ-$) and fitted ($-\times-$) rolling-moment coefficients is shown in Fig. 15. Next, we split the fitted-rolling-moment coefficient into a restoring part, M_r, and a damping part, M_d, as follows:

$$\begin{aligned} M_r = {} & \left(a_1 + a_5\dot{\theta}^2 + a_{11}\dot{\theta}^4\right)\theta \\ & + \left(a_3 + a_{10}\dot{\theta}^2\right)\theta^3 + a_7\theta^5 \end{aligned} \tag{18}$$

$$\begin{aligned} M_d = {} & \left(a_2 + a_4\theta^2 + a_8\theta^4\right)\dot{\theta} \\ & + \left(a_6 + a_9\theta^2\right)\dot{\theta}^3 + a_{12}\dot{\theta}^5 \end{aligned} \tag{19}$$

In Fig. 15, we also show M_r and θ versus time, and M_d and $\dot{\theta}$ versus time. Moreover, we show on these figures the numbers 1, 2, 3, 4 and 5 which correspond to the same numbers in Figs. 11 and 14. In the first quarter of the cycle (1→2), the roll angle θ decreases from $0 \rightarrow -11°$, the restoring rolling moment becomes negative during the first part and positive during the second part and the damping rolling moment, which is negative at point 1, increases during the first part and becomes almost zero during the second part. It is very interesting to notice that M_r and M_d are negative during the first part and hence they are in the same direction as the motion. During the second part, M_r becomes positive reaching its maximum at point 2 when $\theta_{max} = -11°$ and hence it limits the angle growth. During the same second part, M_d becomes almost zero indicating a loss of damping rolling moment. In the second quarter of the cycle (2→3), M_r stays almost constant during the first part and drops to zero in the second part when the roll angle becomes 0°. During the same second quarter, M_d continuously increases from 0 to a maximum positive value when the roll angle becomes 0. In the third quarter of the cycle (3-4), a similar interaction of θ, M_r and M_d as that of the first quarter (1-2) occurs except with opposite signs. These conclusions are exactly similar to those of Ref. 9. Hence, the loss of damping rolling moment is responsible for the wing-rock motion.

CONCLUDING REMARKS

The multidisciplinary problem of wing-rock motion and its active control has been simulated using the unsteady, compressible, Euler equations; the Euler equation of rigid-body dynamiocs and the ND equations for the grid deformation. The fluid flow Euler equations are solved using an implicit, approximately factored, central-difference, finite-volume scheme; rigid-body Euler equation is solved using a four-stage, Runge-Kutta scheme and the ND equations are solved using an ADI scheme. Simulation of the wing-rock problem is obtained for a delta wing which is mounted on an axle with torsional springs and the axle is free to rotate in bearings with viscous damping. The wing starts its motion under the effect of an initial rolling moment due to the initially asymmetric flow at zero roll angle and zero angular velocity. For the active control of wing-rock motion, a tuned anti-symmetric leading-edge flaps oscillation is used to achieve that purpose. Also, it has been shown that the hysteresis responses of position and strength of the asymmetric right and left primary vortices are responsible for the wing rock motion. Moreover, it has also been shown that the loss of aerodynamic damping rolling moment at the zero angular velocity value is a main reason for the wing rock motion. These conclusions are consistent with the previous findings of the experimental[3,4] and computational[9] research work.

ACKNOWLEDGEMENT

This research work has been supported by the NASA Langley Research Center under grant number NAG-1-648. The authors would like also to acknowledge the computational resources provided on the CRAY computers by the NAS-Ames Research Center and by ACD-Langley Research Center.

REFERENCES

1. Nguyen, L. T., Yip, L. and Chambers, X., Jr., "Self-Induced Wing Rock of Slender Delta Wings," AIAA Paper No. 81-1883, August 1981.

2. Levin, D. and Katz, J., "Dynamic Load Measurements with Delta Wings Undergoing Self-Induced Roll-Oscillations," Journal of Aircraft, Vol. 21, January 1985, pp. 30-36.

3. Jun, Y. W. and Nelson, R. C., "Leading Edge Vortex Dynamics on a Delta Wing Undergoing a Wing Rock Motion," AIAA-87-0332, January 1987.

4. Arena, A. S., Jr. and Nelson, R. C., "The Effect of Asymmetric Vortex Wake Characteristics on a Slender Delta Wing Undergoing Wing Rock Motion," AIAA 89-3348-CP, August 1989, pp. 16-24.

5. Arena, A. S. and Nelson, R. C., " Unsteady Surface Pressure Measurements on a Slender Delta Wing Undergoing Limit Cycle Wing Rock," AIAA paper No. 91-0434, January 1991.

6. Morris, S. L. and Ward, D. T., "A Video-Based Experimental Investigation of Wing Rock," AIAA 89-3349-CP, August 1989, pp. 25-35.

7. Ericsson, L. E., "The Fluid Mechanics of Slender Wing Rock," Journal of Aircraft, Vol. 21, May 1984, pp. 322-328.

8. Ericsson, L. E., "Various Sources of Wing Rock," Journal of Aircraft, Vol. 27, June 1990, pp. 488-494.

9. Konstandinopoulos, P., Mook, D. T. and Nayfeh, A. H., "Subsonic Wing Rock of Slender Delta Wings," Journal of Aircraft, Vol. 22, March 1985, pp. 223-228.

10. Elzebda, J. M., Nayfeh, A. H. and Mook, D. T., "Development of an Analytical Model of Wing Rock for Slender Delta Wings," Journal of Aircraft, Vol. 26, August 1989, pp. 737-743.

11. Nayfeh, A. H., Elzebda, J. M. and Mook, D. T., "Analytical Study of the Subsonic Wing-Rock Phenomenon for Slender Delta Wings," Journal of Aircraft, Vol. 26, September 1989, pp. 805-809.

12. Hsu, C. and Lan, C. E., "Theory of Wing Rock," Journal of Aircraft, Vol. 22, Oct. 1985, pp. 920-924.

13. Kandil, O. A. and Chuang, H. A., "Computation of Steady and Unsteady Vortex Dominated Flows with Shock Waves," AIAA Journal, Vol. 26, No. 5, 1988, pp. 524–531.

14. Kandil, O. A. and Chuang, H. A., "Unsteady Transonic Airfoil Computation Using Implicit Euler Scheme on Body-Fixed Grid," AIAA Journal, Vol. 27, No. 8, August 1989, pp 1031-1037.

15. Kandil, O. A. and Chuang, H. A., "Unsteady Delta-Wing Flow Computation Using an Implicit Factored Euler Scheme," First National Fluid Dynamics Congress, July 1988. Also AIAA Journal, Vol. 28, No. 9, September 1990, pp. 1589-1595.

16. Kandil, O. A. and Chuang, H. A., "Unsteady Navier-Stokes Computations Past Oscillating Delta Wing at High Incidence," AIAA-89-0081, January 1989. Also AIAA Journal, Vol. 28, No. 9, September 1990, pp. 1565-1572.

17. Batina, J. T., "Vortex-Dominated Conical-Flow Computations Using Unstructured Adaptively-Refined Meshes," AIAA Journal, Vol. 28, No. 11, Nov. 1990, pp. 1925-1932.

18. Lee, E. M. and Batina, J. T., "Conical Methodology for Unsteady Vortical Flows about Rolling Delta Wings," AIAA-91-0730, January 1991.

19. Kandil, O. A. and Salman, A. A., "Unsteady Vortex-Dominated Flow Around Wings with Oscillating Leading-Edge Flaps," AIAA 91-0435, January 1991.

20. Kandil, O. A. and Salman, A. A., "Unsteady Supersonic Flow Around Delta Wings with Symmetric and Asymmetric Flaps Oscillation," AIAA 91-1105-CP, April 1991, Vol. 3, pp. 1888-1903.

21. Kandil, O. A. and Salman, A. A., "Effect of Leading-Edge Flap Oscillation on Unsteady Delta Wing Flow and Rock Control," AIAA-91-1796, June 1991.

22. Kandil, O. A. and Salman, A. A., "Recent Advances in Unsteady Computations and Applications of Vortex Dominated Flows," Invited paper, 4th International Symposium on Computational Fluid Dynamics, University of California, Davis, September 9-12, 1991, pp. 570-575.

23. Kandil, O. A. and Salman, A. A., "Three-Dimensional Simulation of Slender Delta Wing Rock and Divergence," AIAA 92–0280, January 1991.

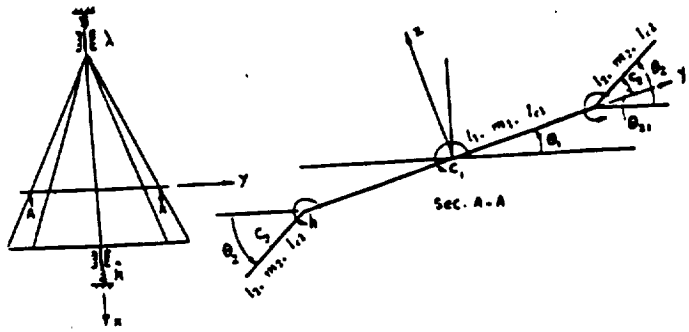

Fig. 1 Wing-Flaps Dynamics for Rolling Motion.

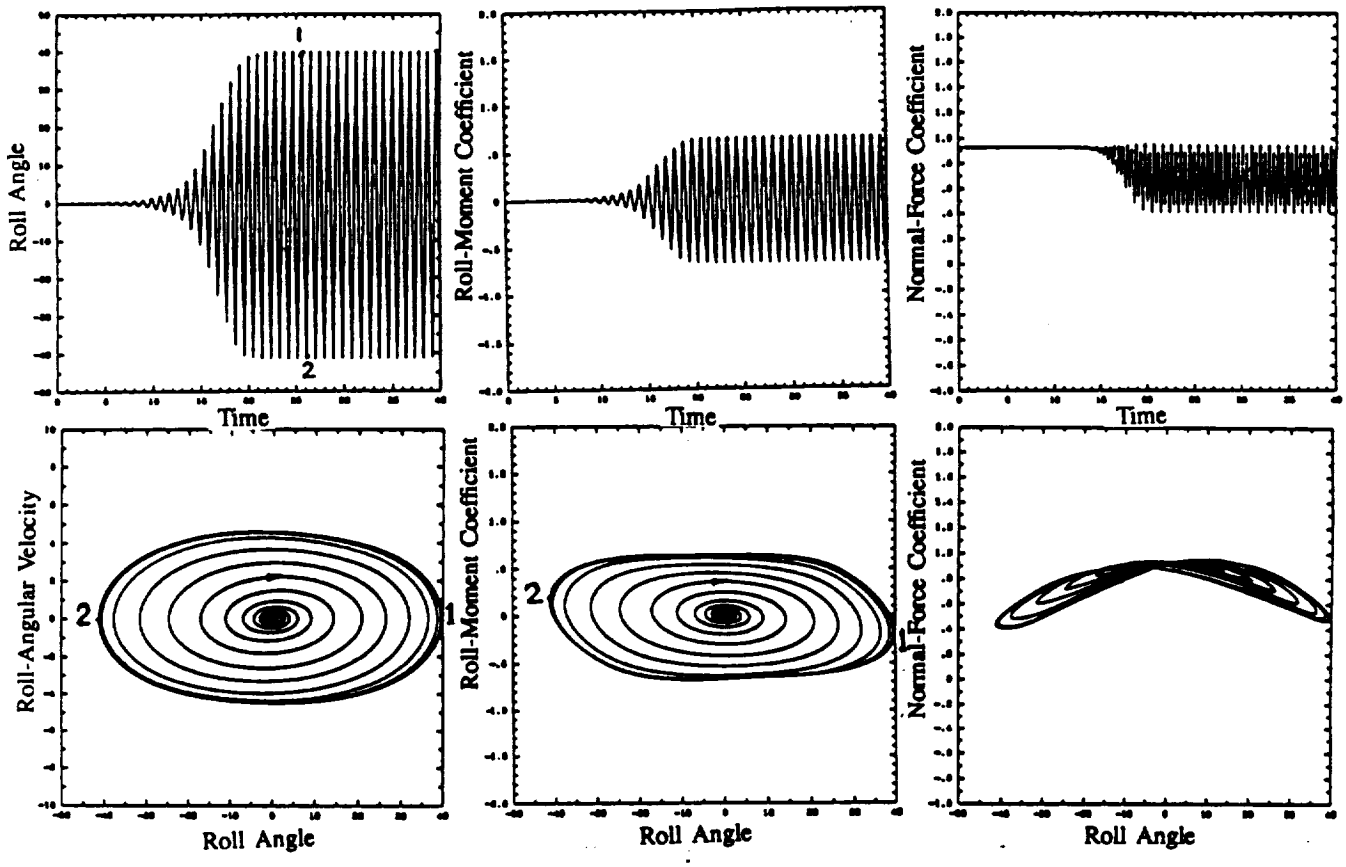

Fig. 2 Roll-Angle, Roll-Moment-Coefficient and Normal-Force-Coefficient Responses for an Unstable Rolling Motion (Wing Rock), $\beta = 80°$, $\alpha = 35°$, $M_\infty = 1.4$, $I_{xx} = 0.02$, $\lambda = 0.$, $\hat{k} = 0.74$, $\Delta t = 0.0025$, $\theta_1^\circ = \dot{\theta}_1^\circ = 0.$

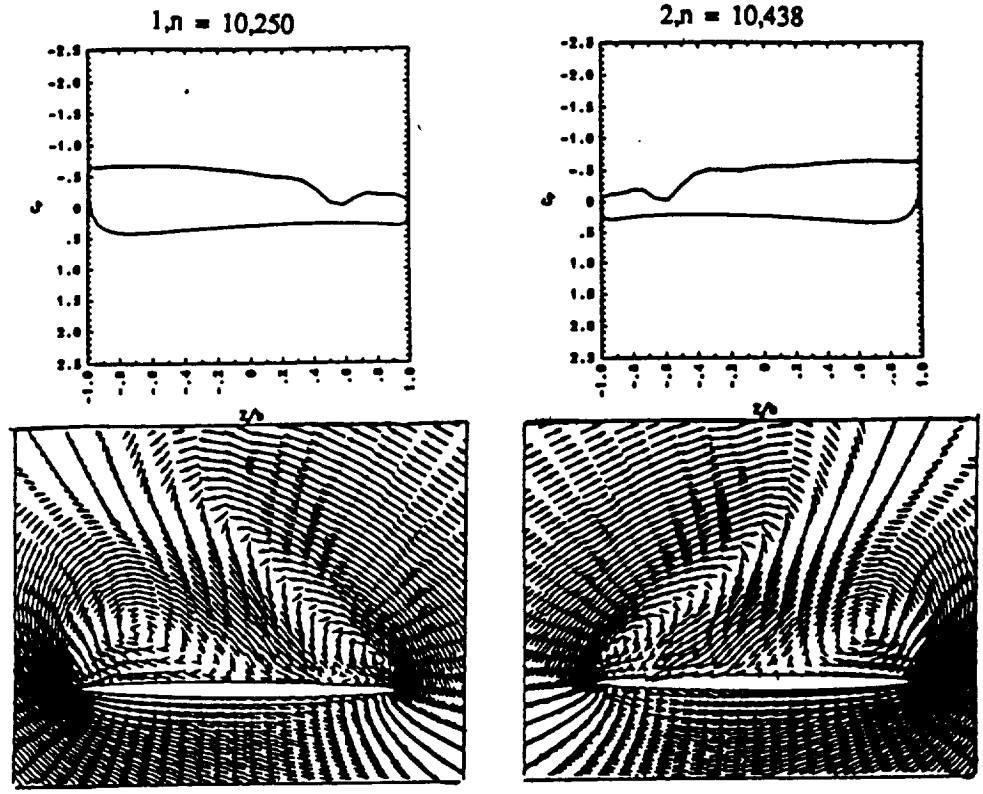

Fig. 3 Surface-Pressure Coefficient and Cross-Flow Velocity During the Limit-Cycle Response, $\beta = 80°$, $\alpha = 35°$, $M_\infty = 1.4$, $\Gamma_{xx} = 0.02$, $\lambda = 0.$, $\hat{k} = 0.74$, $\Delta t = 0.0025$, $\theta_1^o = \dot{\theta}_1^o = 0.$

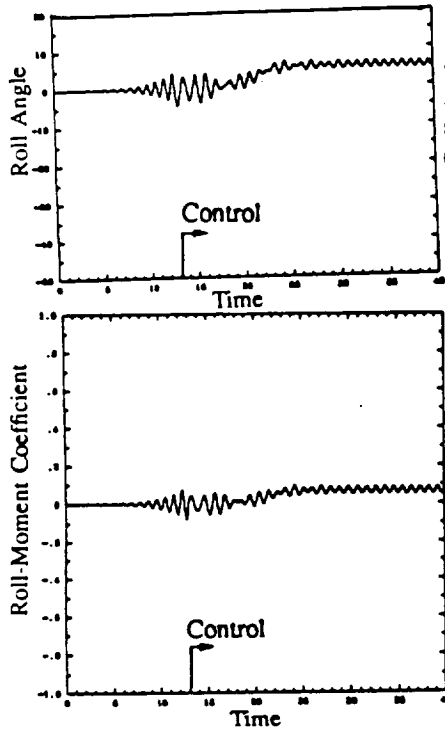

Fig. 4 Leading-Edge Flaps Active Control, $\theta_{21} = \theta_{21\,max} \sin k_f(t - t_o)$, $\alpha = 35°$, $M_\infty = 1.4$, $t_o = 13.02$

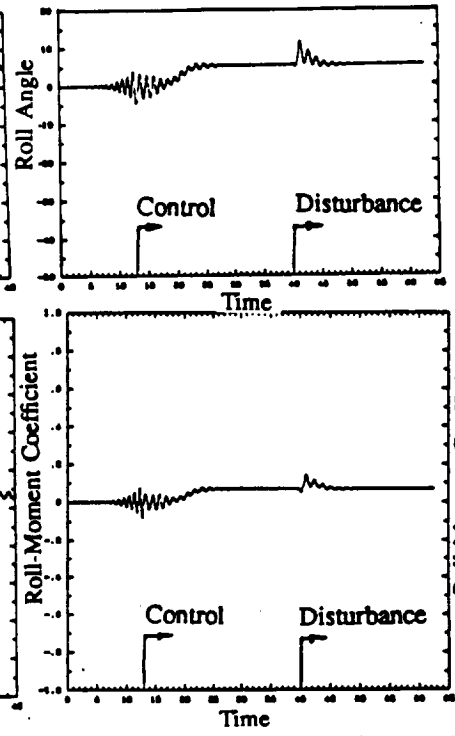

Fig. 5 Decaying-amplitude active control followed by disturbance, $\theta_{21} = \frac{\theta_{21\,max}}{1+(t-t_o)} \sin k_f(t - t_o)$, $\alpha = 35°$, $M_\infty = 1.4$, $t_o = 13.02$

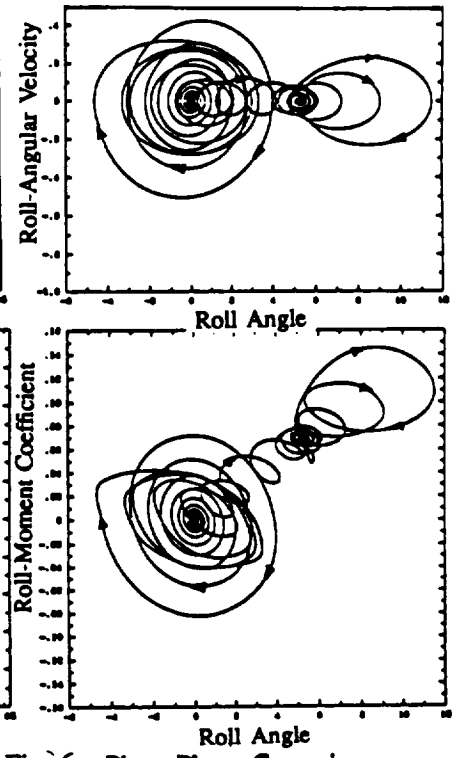

Fig. 6 Phase Planes Covering History of Responses; Instability, Control and Disturbance, $\alpha = 35°$, $M_\infty = 1.4$, $t_o = 13.02$

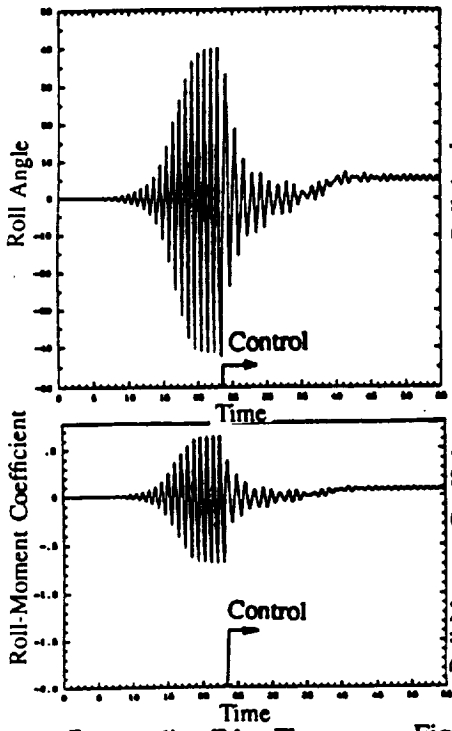

Fig. 7 Leading-Edge Flaps Active Control, $\theta_{21} = \theta_{21\,max} \sin k_f(t - t_o)$, $\alpha = 35°$, $M_\infty = 1.4$, $t_o = 23.7$

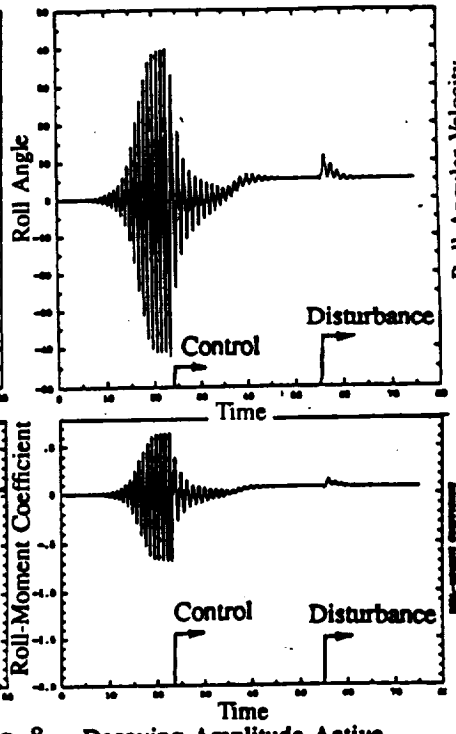

Fig. 8 Decaying-Amplitude Active Control Followed by Disturbance, $\theta_{21} = \frac{\theta_{21\,max}}{1+(t-t_o)} \sin k_f(t - t_o)$, $\alpha = 35°$, $M_\infty = 1.4$, $t_o = 23.7$

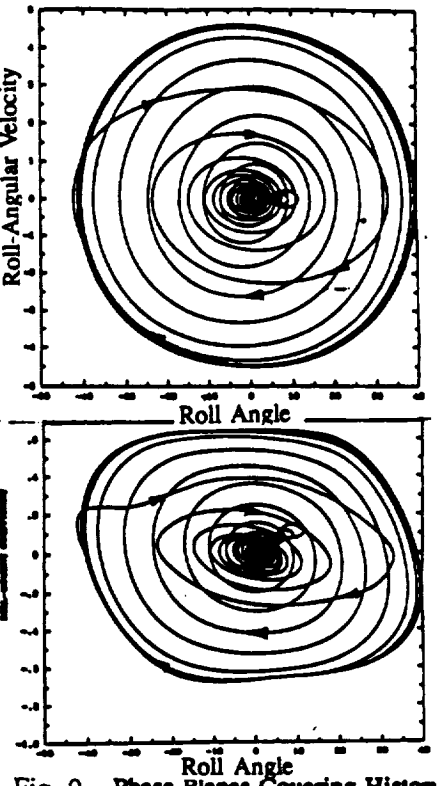

Fig. 9 Phase Planes Covering History of Response; Instability, Control and Disturbance, $\alpha = 35°$, $M_\infty = 1.4$, $t_o = 23.7$

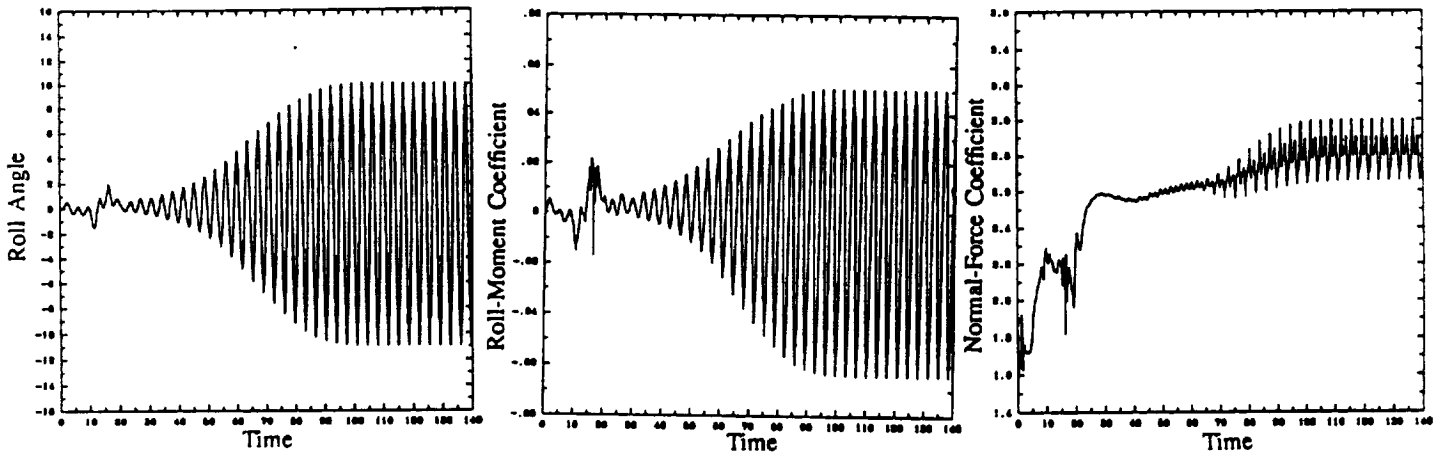

Fig. 10. Roll angle, roll-moment-coefficient and normal-force-coefficient response for wing-rock motion; delta wing, $\alpha = 30°$, $M_\infty = 0.3$, $I_{xx} = 0.285$, $\lambda = 0.15$, $\hat{k} = 0.74$, $\theta_i^\circ = \dot{\theta}_i^\circ = 0$.

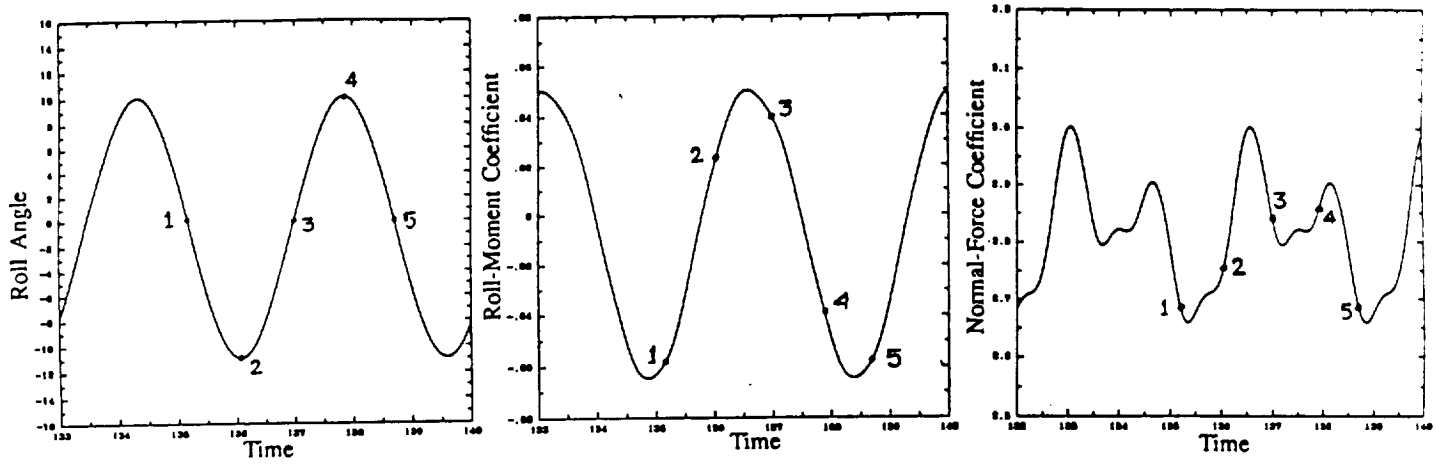

Fig. 11. Time responses for wing-rock motion during the limit cycle response.

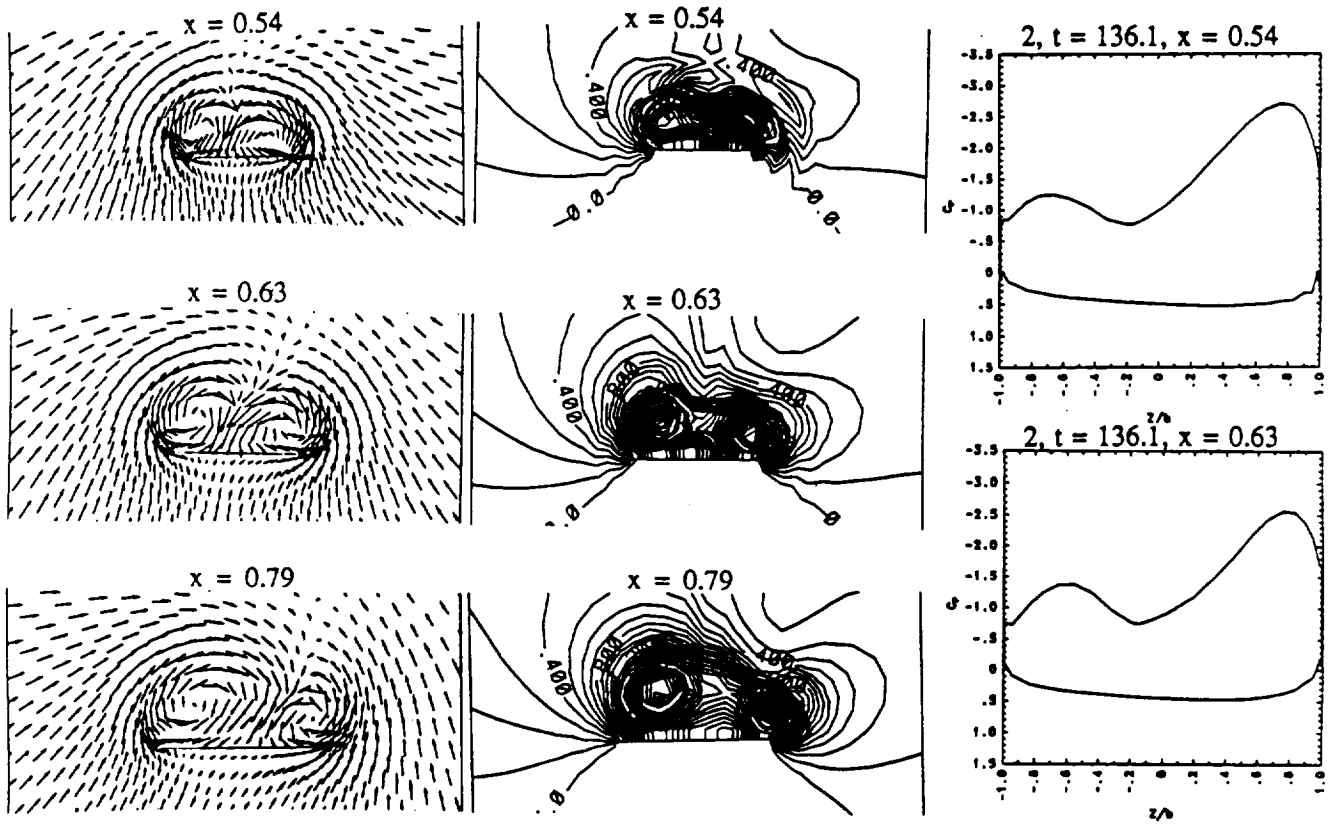

Fig. 12. Snapshot at point 2 of crossflow velocity, static-pressure contours and surface pressure for wing-rock motion.

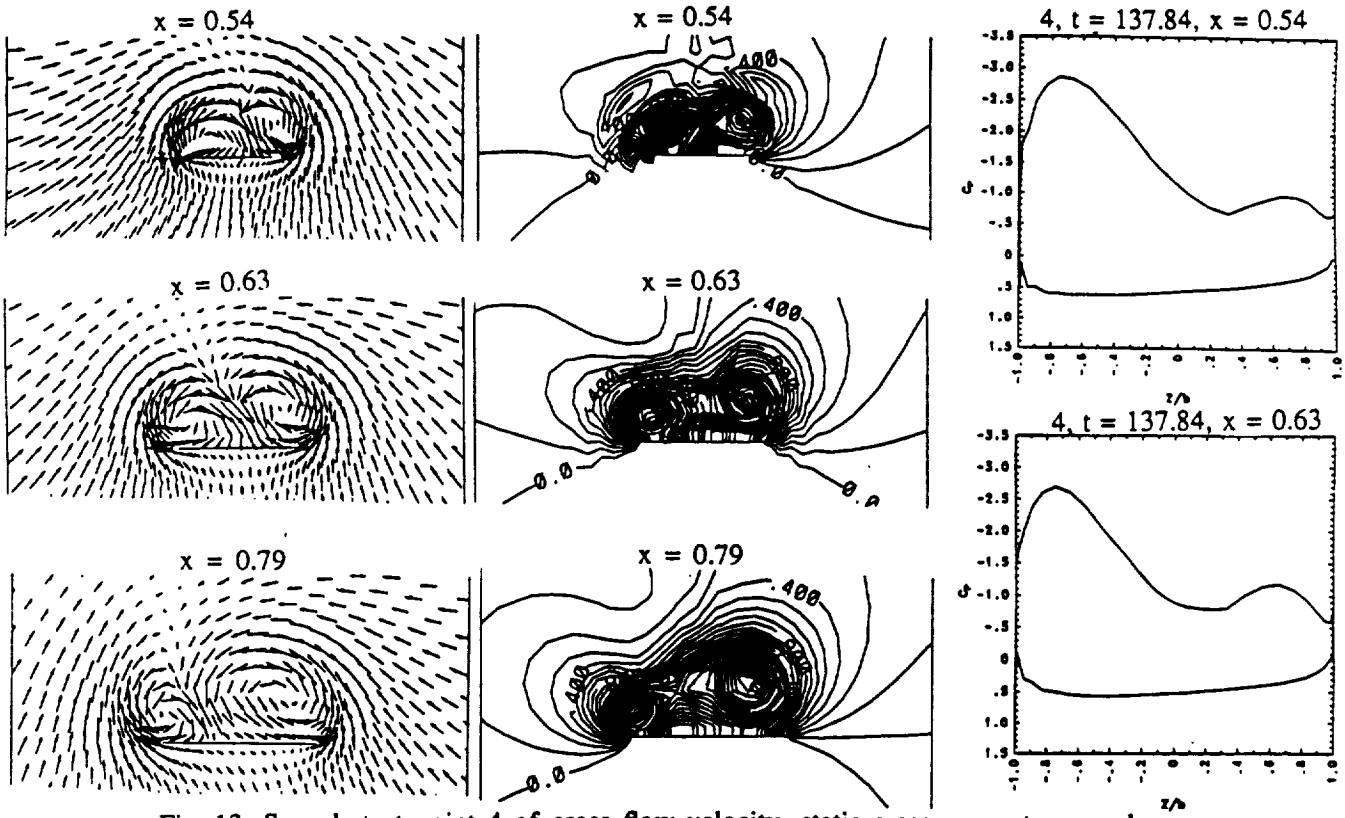

Fig. 13. Snapshot at point 4 of cross flow velocity, static-pressure contours and surface pressure for wing-rock motion.

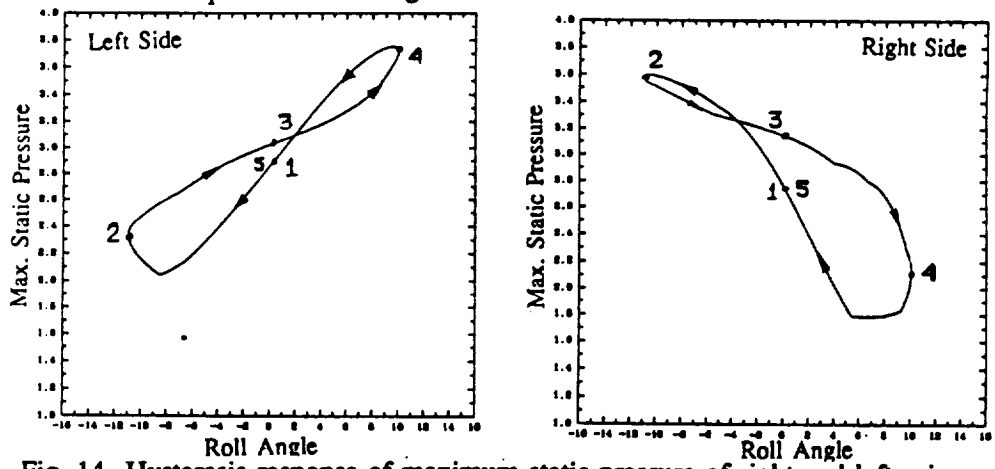

Fig. 14. Hysteresis response of maximum static pressure of right and left primary vortices for wing-rock motion during the limit-cycle response.

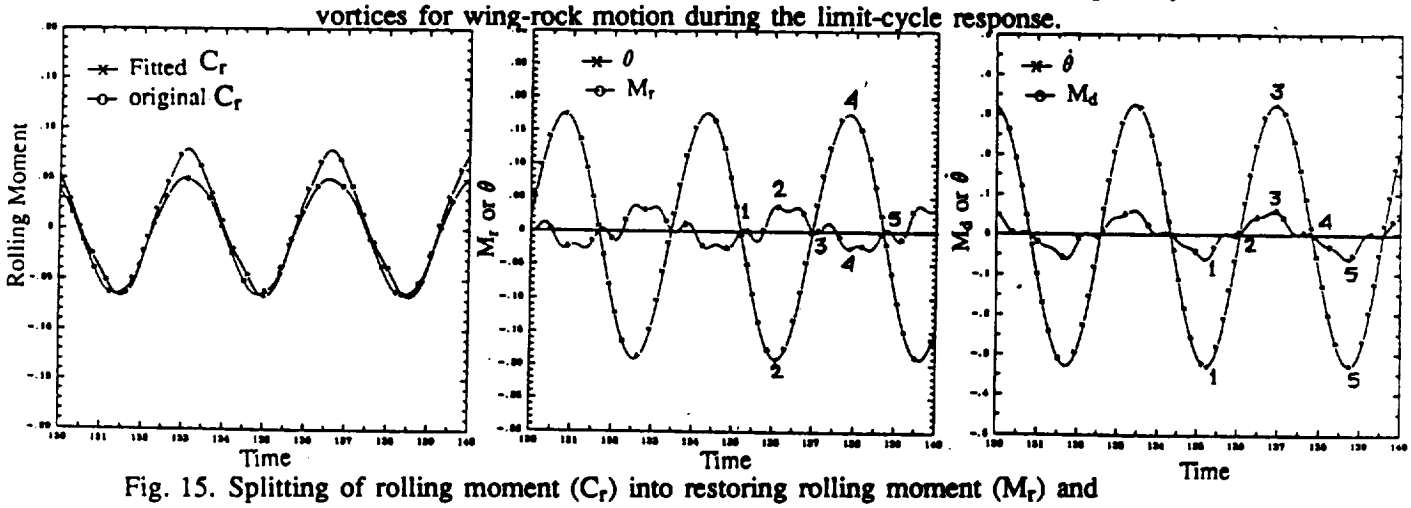

Fig. 15. Splitting of rolling moment (C_r) into restoring rolling moment (M_r) and damping rolling moment (M_d) for wing-rock motion during the limit-cycle response.